TEMPERATURE-DEPENDENT THREE-PHASE POWER FLOW FOR UNBALANCED RADIAL SYSTEMS

by

Forest Atchison

A thesis submitted to the faculty of
The University of North Carolina at Charlotte
in partial fulfillment of the requirements
for the degree of Master of Science in
Electrical Engineering

Charlotte

2022

Approved by:

_____
Dr. Valentina Cecchi

_____
Dr. Badrul Chowdhury

_____
Dr. Sukumar Kamalasadan

ABSTRACT

FOREST ATCHISON. Temperature-dependent three-phase power flow for unbalanced radial systems. (Under the direction of DR. VALENTINA CECCHI)

Traditional power flow algorithms, including Newton-Raphson (NR) based methods and backward-forward sweep (BFS) based techniques, consider conductor resistance as a fixed quantity predetermined for some assumed combination of ambient conditions (weather, soil temperature, etc.) and loading that imply a certain conductor temperature. However, during the course of an iterative power flow algorithm, the calculated current, and thus conductor temperature, and consequently conductor resistance are changing at each iteration. Therefore, dependent on the actual ambient and loading conditions of a system, there can be a non-negligible temperature related error embedded in a conventional power flow solution.

Some work has been done to address this in transmission systems with NR-based temperature-dependent power flow techniques, but the literature is almost silent on the effect that the consideration of conductor temperature may have on power flow for distribution systems. Distribution systems have unique characteristics including radial topologies, high R/X ratios, smaller quantities of delivered power, shorter line segments, and an inability to make assumptions about balanced loading that make them distinct from transmission systems and often require non-NR based solution methods to solve the power flow problem, such as BFS techniques.

In this work, a temperature-dependent three-phase power flow algorithm for radial systems is proposed. The proposed algorithm couples the electrical and thermal characteristics of overhead and underground lines for a more accurate solution to the power flow problem. This method is capable of accounting for the particularities and requirements of modeling distribution systems as distinct from transmission systems, including untransposed lines, unbalanced loading, three-phase transformer and volt-

age regulator models, and constant current, impedance, and power loads. The line phase impedance matrices are updated at each iteration of the algorithm with the calculated resistance as derived from the calculated conductor temperature. The proposed method is tested against standard IEEE test feeders using real world weather and soil temperature data sets, and the results are compared against the accepted benchmarks with respect to system nodal voltage profile, real power loss, and degree of voltage unbalance.

ACKNOWLEDGEMENTS

I would like to acknowledge the unflagging support and encouragement of my graduate advisor, Dr. Valentina Cecchi. I thank Dr. Cecchi for providing the opportunity to become involved in research as an undergraduate, and the invitation made to me at that time to join her Power Delivery Innovation Research Group at UNC Charlotte. Dr. Cecchi has been a consistent advocate of my educational goals and advancement, and I will be forever indebted to her for her guidance and mentorship.

I would also like to thank Dr. Badrul Chowdhury and Dr. Sukumar Kamalasadan for serving on my thesis committee and for the knowledge I received while under their instruction. The work in this thesis is built upon what I was taught during Dr. Cecchi's, Dr. Chowdhury's, and Dr. Kamalasadan's classes.

I would also like to convey my gratitude to the faculty and staff at large at the Energy Production and Infrastructure Center (EPIC) and the Department of Electrical and Computer Engineering for the excellent undergraduate and graduate education I and many others received, and for many office hours, emails, and candid conversations.

I would also like to gratefully acknowledge the support of the National Science Foundation in providing funding through the Graduate Research Fellowship Program during the course of this work [1].

Finally, I would like to thank my family, especially my wife Julie, who has been a cheerful and unwavering source of support during this process.

[1]This material is based upon work supported by the National Science Foundation Graduate Research Fellowship Program under Grant No. 1848727. Any opinions, findings, and conclusions or recommendations expressed in this material are those of the author(s) and do not necessarily reflect the views of the National Science Foundation

TABLE OF CONTENTS

LIST OF TABLES

LIST OF FIGURES

LIST OF SYMBOLS AND ACRONYMS

δ_i Voltage angle at bus i

δ_n Voltage angle at bus n

$|I^L_{a,b,c}|\angle\alpha_{a,b,c}$ Complex load current magnitude and angle, wye-connected load

$|I^L_{ab,bc,ca}|\angle\alpha_{ab,bc,ca}$ Complex load current magnitude and angle, delta-connected load

$|S_{a,b,c}|\angle\theta_{a,b,c}$ Nominal complex power magnitude and angle, wye-connected load

$|S_{ab,bc,ca}|\angle\theta_{ab,bc,ca}$ Nominal complex power magnitude and angle, delta-connected load

$|V_{ab,bc,ca}|\angle\delta_{ab,bc,ca}$ Nominal complex line-to-line voltage magnitude and angle, phases ab, bc, ca

$|V_{an,bn,cn}|\angle\delta_{a,b,c}$ Nominal complex line-to-neutral voltage magnitude and angle, phases a, b, c

$|Z_{a,b,c}|\angle\theta_{a,b,c}$ Constant complex wye-connected load impedance magnitude and angle, phases a, b, c

$|Z_{ab,bc,ca}|\angle\theta_{ab,bc,ca}$ Constant complex delta-connected load impedance magnitude and angle, phases ab, bc, ca

$|\hat{V}_{ab,bc,ca}|\angle\hat{\delta}_{ab,bc,ca}$ Calculated complex line-to-line voltage magnitude and angle, phases ab, bc, ca

$|\hat{V}_{an,bn,cn}|\angle\hat{\delta}_{a,b,c}$ Calculated complex line-to-neutral voltage magnitude and angle, phases a, b, c

φ_{in} Angle of impedance between bus i and bus n

G_{ii} Conductance of ii^{th} element of admittance matrix

P_i Real power flow from node i

P_r Receiving bus real power

Q_i Reactive power flow from node i

Q_r Receiving bus reactive power

R Resistance between receiving and sending bus

T_c Conductor temperature

V_i Complex voltage at node i

V_n Complex voltage at node n

V_r Receiving bus voltage

V_s Sending bus voltage

X Reactance between receiving and sending bus

Y_{in} Complex in^{th} element of admittance matrix

BFS Backward-forward sweep

CIGRE Conseil International des Grands Reseaux Electriques (International Council on Large Electric Systems)

DLR Dynamic line rating

IEC International Electrotechnical Commission

IEEE Institute of Electrical and Electronics Engineers

NEMA National Electrical Manufacturers Association

NR Newton-Raphson

PF Power flow

SSHBE Steady-state heat balance equation

TDOPF Temperature-dependent optimal power flow

TDPF Temperature-dependent power flow

ZIP Acronym for constant impedance, constant current and constant power loads

CHAPTER 1: INTRODUCTION

1.1 Overview

The focus of this thesis lies on modeling the effect that weather conditions and soil temperature have on the power flow solutions of three-phase unbalanced radial distribution systems containing both underground and overhead line sections. These effects include varying voltage profiles[1], real power loss, and voltage unbalance. Additionally, the effect of varying load in conjunction with varying weather and soil conditions on the power flow solution is addressed. A temperature-dependent three-phase radial power flow algorithm is introduced; the algorithm is capable of coupling the thermal and electrical parameters of a distribution network containing both underground and overhead line sections, with unbalanced loading and untransposed lines. The proposed method incorporates calculations of the conductor temperatures for underground cable and overhead conductors into the power flow algorithm. The calculated conductor temperatures, which are dependent on weather conditions, soil conditions, conductor characteristics, and loading, are used to modify the phase impedance matrices associated with each line section, which in turn affect the iterative calculation of the unknown bus voltages, power flows, and various system characteristics of interest.

The following topics are presented in this chapter:

- Background and motivation for this work;
- Research objectives and contributions;
- Overview of the organization of the thesis.

[1]Defined for this work as pu voltage magnitude with respect to each node of the system. For a three-phase system, there will be three voltage profiles.

1.2 Background and Motivation

The aim of this thesis is to determine the effect that considering the temperature of overhead and underground conductors has on the solution to the power flow problem for three-phase unbalanced radial distribution systems. The motivation lies in the relative scarcity of information in the existing literature to answer this question.

The effect of real-time or predicted weather conditions on line ampacity, known as dynamic line rating (DLR), is well represented in existing literature [1–6]. These studies have found that taking weather conditions into account for ampacity calculations can substantially increase the thermal rating, and thus the allowable ampacity, of overhead lines [5], [6]. The vast majority of the existing literature considers DLR in the context of overhead transmission lines, and depend largely on either IEEE Std. 738 [7] or CIGRE Technical Brochure 601 [8], which provide guidelines to integrate weather conditions into the calculation of the line current carrying capacity for bare overhead conductors.

Not only has it been shown that weather conditions affect the calculation of line thermal rating and corresponding ampacity limits, but there is also a broad representation in existing literature that discusses the effect ambient conditions such as weather can have on the system-level analysis of power systems. As variation of the weather conditions impacts the line conductor temperatures and resultant electrical parameters [9], [10], it affects the line impedance values. Conventionally used power flow methods do not account for the impact of the conductor temperatures while performing steady-state analysis of power systems [11–13]. Preset values of line electrical parameters are used in the traditional power flow analysis, i.e. the resistance is fixed and does not vary with conductor temperature, which is dependent on ambient conditions such as weather, but also iteratively varies with the calculated current during the power flow algorithm. Power flow algorithms capable of considering the variation of conductor temperatures have been proposed in several research works [14–17].

These works have shown that the calculated bus voltages and losses can vary significantly when conductor temperature is considered. These algorithms are almost exclusively Newton-Raphson (NR) based, consider only overhead lines as opposed to underground cables, and operate on per-phase models of transmission systems. A brief review of existing temperature-dependent power flow literature for transmission systems will be presented in section 2.3.1.

Power flow analysis of distribution systems is distinctly different from that of transmission systems. Distribution systems are often radial, or at best weakly meshed, and have high R/X ratios as compared to transmission networks. These characteristics cause the NR Jacobian to be prone to singularity and for the algorithm to fail [18]. For this reasons, other methods of solving the power flow problem for radial distribution systems have been proposed in the literature to overcome the shortcomings of the NR technique, including backward-forward sweep (BFS) methods [18–26]. Additionally, in per-phase power flow analysis typically conducted for transmission networks, assumptions have been made including the transposition of line conductors and balanced loading. These assumptions will typically not hold for distribution systems, and the applied power flow techniques must consider a polyphase model of the network that includes untransposed line conductors and unbalanced loading conditions [27].

The representation in the literature of temperature-dependent power flow models for distribution systems is much less extensive as compared to transmission systems, and the models are not three-phase and thus do not account for unbalanced systems [28]. The systems that are studied in [28] consist exclusively of overhead lines, which disregards the practical reality of combined overhead and underground distribution systems. Additionally, the existing work considers only constant power loads, neglecting constant impedance and constant current loads. It is common and necessary in distribution system modeling to consider all three load types [27], which can be referred to by the acronym ZIP (Z, constant impedance; I, constant current; P,

constant power).

This thesis intends to fill a void in the current literature by proposing a temperature-dependent three-phase power flow model for radial distribution systems capable of accommodating ZIP loads, untransposed lines, unbalanced loading, overhead and underground lines, and other common circuit elements such as transformers, voltage regulators, and capacitor banks.

1.3 Research Objectives

The proposed temperature-dependent three-phase power flow algorithm allows for the determination of the extent to which considering conductor temperature affects the solution to the power flow problem for three-phase unbalanced radial distribution systems. These effects include, but are not necessarily limited to, a variation from the baseline solution with respect to the following:

- Voltage profile;
- Phase, branch, and total real power losses;
- Degree of nodal voltage unbalance.

The developed method is tested on several IEEE test feeders [29] that contain underground and overhead lines, unbalanced loading, and common circuit elements such as transformers, voltage regulators, and capacitor banks. The developed algorithm must be capable of accommodating a radial topology, untransposed lines, unbalanced ZIP loading, and incorporate temperature calculations for both underground cable and overhead bare conductors.

The temperature-dependent solution is compared to the baseline solution (i.e., with fixed resistance), with respect to the itemized characteristics above.

1.4 Research Contributions

The research contributions of this work can be summarized as follows:

- Synthesis of three-phase component modeling from first principles for power flow studies;
  - Transformers of various primary and secondary connections
  - Voltage regulator
  - Capacitor banks (delta and wye connected, single- and three-phase)
  - ZIP loads (delta and wye connected, single-, two-, and three-phase)
  - Overhead and underground lines
- Development and implementation of three-phase BFS-based power flow algorithm for radial systems capable of accommodating unbalanced loading and incorporating component models listed above;
- Synthesis of electrothermal modeling indicated by IEEE Std. 738 for bare overhead conductors;
  - Development and implementation of bisection algorithm to enable fast computation of IEEE Std. 738 equations governing non-linear relationship between conductor temperature and current
- Synthesis of electrothermal modeling indicated by IEC 60287 for underground cables;
  - Development and implementation of subroutine to calculate cable conductor temperature utilizing the relationships presented in IEC 60287
- Incorporation of electrothermal modeling into derivation of phase impedance matrices for power flow algorithm;
  - Matrices developed from first principles at each iteration to account for variation in conductor temperature and corresponding resistance;

- Development and implementation of power flow algorithm mentioned above with incorporation of electrothermal modeling of overhead lines and underground cables.

1.5 Thesis Organization

The thesis is structured as follows:

- In Chapter 2, a problem statement is presented, and the literature review to address the problem statement is discussed.
- In Chapter 3, detailed descriptions of circuit component models are presented.
- In Chapter 4, the coupling of electrical and thermal parameters is discussed for both overhead lines and underground cables.
- In Chapter 5, both a baseline (fixed resistance) and the proposed temperature-dependent backward-forward sweep power flow algorithm are presented.
- In Chapter 6, case studies are conducted and the results are discussed.
- In Chapter 7, the accomplishments and contribution of this research is summarized and concluded with future work.

CHAPTER 2: PROBLEM STATEMENT AND LITERATURE REVIEW

2.1 Overview

Several topics required review when approaching the problem of a temperature-dependent power flow algorithm for distribution systems. The requisite component modeling will be discussed in Chapter 3 and the electrothermal coupling of line sections will be addressed in Chapter 4. In this chapter however, a literature review is presented with respect to the solution methods for the power flow problem for distribution systems and temperature-dependent system level analysis of both transmission and distribution systems.

The following topics are presented in this chapter:

- Problem statement that motivated the literature review;
- Review of prior work on temperature-dependent power system modeling and analysis;
- Review of different techniques for performing power flow in distribution systems;
- Review of works pertaining to temperature-dependent power flow for distribution systems.

2.2 Problem Statement

The thermal state of an electrical conductor is known to be dependent on the current which passes through the conductor and on the ambient conditions [7], [30]. It is also known that the line resistance has an approximately linear relationship with conductor temperature [31]. It is further known from Ohm's and Joule's laws that

current drawn by a load will be affected by line resistance. Thus there is a recursive relationship between current, resistance, and conductor temperature.

It has been demonstrated in the literature that taking conductor temperature into consideration will have a non-negligible effect on the solution to the power flow problem, particularly for transmission systems, where the bulk of this work has been done. Section 2.3.1 that follows gives a brief review of this work.

What is not well known, or at least not well documented in the literature, is the extent to which electrothermal coupling of resistance, current, and conductor temperature can affect the power flow solution for distribution systems, with comparatively shorter lines and smaller quantities of delivered power. This is the research question that this thesis will begin to address: will a temperature-dependent three-phase power flow algorithm show non-negligible differences in calculated system characteristics when applied to distribution networks?

In order to answer this question, several aspects of the work must be addressed individually before they can be synthesized into a final working algorithm:

- Component modeling (addressed in Chapter 3);
- electrothermal coupling (addressed in Chapter 4);
- A suitable power flow algorithm must be chosen and developed with the following characteristics:
  - Three-phase
  - Capable of handling unbalanced ZIP loads
  - Capable of iterative updates to phase impedance matrices
  - Reasonably fast for a moderately-sized system ($\approx$100 nodes)

2.3 Literature Review

The literature review in the sections that follow was conducted to determine a suitable power flow algorithm and to generally assess the direction of work done related to this thesis. Section 2.3.1 will address temperature-dependent power system modeling and analysis in general, including primarily transmission systems, where the majority of the existing work has been focused, and is composed of a synthesis of the author's previous work concerning a review of temperature dependent analysis in electric power systems [32]. Section 2.3.2 will discuss various methodologies and algorithms that have been proposed and developed to solve the power flow problem for distribution systems. Section 2.3.3 will be similar in scope to section 2.3.1, but will address specifically the work that has been done on temperature-dependent power flow for distribution systems.

2.3.1 Temperature-Dependent Power System Modeling and Analysis

Apart from line current, which offers the greatest contribution, there are many external factors that can impact the temperature of an overhead line [33–36]. The geographic location of the line, elevation from sea level, exposure to the sun, and weather conditions can all affect the temperature of the line conductor; although among these, the impact of weather conditions plays the most vital role [37], [38]. Weather conditions, such as ambient temperature, wind speed, wind direction, solar insolation, etc. directly impact the conductor temperatures of overhead lines [38]. Along with the above-mentioned factors, aging of the conductors and the environmental pollution level of different areas can also impact the conductor temperatures [39], [40]. A detailed description of the relationship between conductor parameters, weather conditions, and conductor temperature for overhead lines will be presented in section 4.2. The temperature of underground cable is dependent on the properties of the cable itself, the method of burial, and the ambient soil temperature. A detailed description

of these relationships will be presented in section 4.3.

By utilizing these relationships, coupled with the relationship between conductor temperature and the electrical characteristics of the line, researchers have sought to achieve more accurate solutions in steady-state analysis of power systems such as power flow. The works that follow in this section are concerned exclusively with transmission systems, are Newton-Raphson based, assume balanced constant power loading (and thus perform per-phase analysis), and consider only overhead lines.

Power flow (PF) is the most widely used method for steady-state analysis of power systems. Conventionally, power flow methods assume constant line electrical parameter values. Similar to a static line rating approach, a set of predefined values are used for the line electrical parameters [12,41–43]. Therefore, conventional power flow methods do not consider the impact of weather conditions and conductor temperatures on the line impedance values [44], [45]. As the assumption of line electrical parameter values may often vary from the practical values of the parameters, it is possible that conventional power flow methods would generate a certain level of temperature-related inaccuracy [46], [47]. Moreover, the traditional methods of power flow only provide information about the electrical conditions of the system. Thermal conditions of the system branches and other equipment cannot be obtained using the traditional methods [14, 15, 45]. With the increased importance of DLR and the prospect of its implementation in transmission systems by many utilities [48–50], availability of power system analysis methods capable of incorporating weather conditions have become increasingly necessary. The coupling of electrical and thermal parameters has been addressed by authors in a variety of different ways, primarily through one of two methodologies: 1) a fully coupled approach that seeks to incorporate the heat balance equations of IEEE [7] or CIGRE [8] standards into the Jacobian matrices of the power flow equations, or 2) a fully or partially decoupled approach whereby the heat balance equation is solved for each iteration of a traditional power flow, providing an updated

branch admittance at each iteration. These various coupling approaches further vary by: 1) having certain weather parameters included or excluded from the algorithm, 2) which standard is used to relate the thermal and electrical parameters (although the standards are very similar), 3) whether or not the thermal equations from the standards have been greatly simplified or linearized. Some works have omitted weather conditions entirely and instead considered the a priori line temperature and its effect on the line impedance, and thus the solution to the power flow algorithm.

The authors in [15] proposed a decoupled modification to the conventional power flow whereby the line current and weather conditions in conjunction with simplified versions of the thermal equations of [7] are used to update the line temperature and resulting resistance for each iteration. Authors in [14] showed an initial step at the coupling of conductor temperatures into the conventional Newton-Raphson power flow method. Using simplified and linearized versions of the heat gain and heat loss equations from the heat balance equation, a novel conductor temperature difference equation is introduced. This difference equation is integrated with the power flow equations, essentially making the power flow Jacobian a 3x3 matrix, instead of the conventional 2x2 Jacobian. Using the proposed approach, the authors studied the impact of ambient temperature on power flow analysis. Though the approach explicitly showed the incorporation of only ambient temperatures, it may be capable of considering other weather conditions as well.

In [51–53], the authors used the temperature-dependent power flow (TDPF) methods developed in [14] for temperature-dependent optimal power flow (TDOPF) analysis. In [51], the impact of the ambient temperatures on branch electrical parameters was integrated into the optimal power flow and the optimization problem was solved using a sine cosine algorithm (SCA). A simplified interior point method was used for optimal power flow in [52] using a coupling property of the electrical and thermal variables. The gbest-guided artificial bee colony algorithm is used, incorporating the

impact of conductor temperatures on branch parameters, for the optimal power flow solution in [53]. Again, as in [14], the only weather parameter considered is ambient temperature, although the method may be capable of integrating further conditions. The authors of [54] also used a linearized relationship between the rise in ambient temperatures and branch losses to propose a TDOPF using a primal-dual interior point method (PDIPM). All the above-mentioned approaches showed the effective minimization of the branch losses and generation cost by incorporating the ambient conditions into optimal power flow solutions.

The preceding works utilize linearized and simplified versions of the heat balance equations and associated thermal parameters when integrating into the power flow solution. To overcome the limits of this linearization, authors in [16] proposed a novel temperature-dependent power flow method using the non-linearized heat balance equation. A Newton code-based solution method for highly non-linear systems [55] was used in this approach. As the heat equations were not linearized, this method is capable of accounting for all the weather parameters described in [7]. Instead of inserting the thermal equations into the power flow equations, the heat balance and power flow equations are solved sequentially in each iteration in a decoupled method; therefore, the size of the Jacobian is not changed. The resulting Y matrix components are functions of conductor temperature (T_c), as can be seen in Eq. (2.1).

$$\begin{aligned} P_i &= |V_i|^2 G_{ii}(T_c) + \sum_{n=1;n\neq i}^{N} |V_i V_n Y_{in}(T_c)| cos(\varphi_{in}(T_c) - \delta_i + \delta_n) \\ Q_i &= |V_i|^2 G_{ii}(T_c) - \sum_{n=1;n\neq i}^{N} |V_i V_n Y_{in}(T_c)| sin(\varphi_{in}(T_c) - \delta_i + \delta_n) \end{aligned} \tag{2.1}$$

As the developed temperature-dependent power flow method can provide conductor temperatures of the transmission lines, this benefit can be utilized to accurately

determine the maximum power handling capability of a system. As an example to quantify the differences between results obtained with TDPF and traditional power flow, in [16], it is found that the power handling capacity of the IEEE 39-bus test system can be increased by 9% when TDPF is used. The same percentage increases to 15% when the spatial variation of weather conditions is also integrated into TDPF.

Another approach using the non-linearized heat balance equation was used for a so-called weather-dependent power flow (WDPF) analysis in [17]. In this method, the modified heat balance equation works as the third equation in power flow analysis which increases the size of the Jacobian, presenting a detailed full coupling of the non-linear heat balance equation and the conventional power flow equations. Using real weather data obtained from a weather station in New Zealand, this work demonstrated that the maximum real power loss error for the system was 15.5% at a certain point over the course of a year when comparing the conventional PF and WDPF.

2.3.2 Power Flow for Distribution Systems

Power flow algorithms are essential for the analysis of power systems, and inform the planning and operation of the the electric grid. The power flow problem, whether for transmission or distribution systems, involves calculating unknown bus voltage angles and magnitudes, active and reactive powers, and consequently the line loading characteristics of a power system. Newton-Raphson based methods, as those presented in the previous section, are the industry standard and work well in the case of meshed networks such as many transmission systems, but often have poor convergence characteristics for radial systems. Distribution systems are often radial, or at best weakly meshed, and have high R/X ratios as compared to transmission networks. These characteristics cause the Newton-Raphson Jacobian to be prone to singularity and for the algorithm to fail [18]. For this reason, other methods of solving the power flow problem for radial distribution systems have been proposed in the literature to overcome the shortcomings of the Newton-Raphson technique.

These methods generally fall into two categories: Kirchoff's formulation-based sweep algorithms and bi-quadratic equation-based sweep algorithms [22]. Both are backward-forward sweep (BFS) based methods that iteratively calculate backward (upstream) and forward (downstream) along the feeder and laterals of a radial system until convergence and differ only in the basic circuit relationships used in voltage calculation. Kirchoff's formulation-based sweep algorithms employ Kirchoff's well known voltage and current laws and a process of current summation to calculate node voltages during backward and forward sweeps. Bi-quadratic equation-based sweep methods relate the voltage magnitude at the receiving end of a branch to the branch power and the voltage at the sending end via the bi-quadratic equation relating voltage and power, and utilize a process of power summation. This bi-quadratic relationship can be seen in Eq. (2.2), with the maximum real root of this equation giving the line receiving end voltage magnitude.

$$V_r^4 + 2V_r^2(P_rR + Q_rX) - V_s^2V_r^2 + (P_r^2 + Q_r^2)Z^2 = 0 \tag{2.2}$$

Although many variations exist in the literature, in general, Kirchoff's formulation-based sweep methods employ a first step of current summation in the backward sweep, summing the currents at each node as the algorithm traverses the circuit from the end nodes towards the source or root node. The second step is then node voltage calculation in the forward sweep using the currents calculated in the backward sweep, moving from root node to end nodes. This process continues iteratively until some convergence criteria is met.

The authors of [23] present a power flow method for radial or weakly-meshed systems using a multi-port compensation technique and Kirchoff's laws. The method can be applied to single-phase or three-phase networks, although only the single-phase

treatment is given in detail. The convergence criteria given in this work is maximum real and reactive power mismatch of loads. In a variation of Kirchoff's-based sweep methods, a method based on ladder network theory is demonstrated in [24], [27]. The primary difference between a more conventional BFS method and the described ladder network theory method is that voltages are also computed in the backward sweep in addition to the forward sweep. In this technique, the convergence criteria is the calculated difference between the magnitude of the source voltage of successive iterations.

As distribution networks are often very large, containing thousands of nodes, researchers have also sought to increase the speed and efficiency of some of these earlier conventional methods. In [56], the authors propose the use of a load-impedance matrix (LIM) to calculate the bus voltages in a single step per iteration, unlike the two step conventional BFS. The LIM represents the contribution of the loads to the voltage drops along the branches of the system. The method is tested on both balanced and unbalanced systems and is reported as being between 2-5 times faster than conventional BFS. In another proposed method of increasing speed, the authors of [18] propose a fast and flexible radial power flow (FFRPF) utilizing a radial configuration matrix (RCM). The RCM becomes the building block matrix for several other matrices which are used in the sweep algorithm, each of which need only be computed once at the beginning of the process. This method is tested on several systems, both balanced and unbalanced, and is reported to be approximately twice as fast as a Gauss Zbus method and the radial load flow method described in [23].

In bi-quadratic sweep-based methods, power summation is employed in the backward sweep and voltages are calculated in the forward sweep utilizing Eq. (2.2). The authors of [20] develop a method for application to weakly meshed systems which converts the original system to a radial network. In the backward sweep, power losses and sending and receiving end powers are calculated and then summed moving from

the end node to the root node. Then in the forward sweep, using the known sending end power, the receiving end voltages are calculated. A similar technique is used in [25], [26].

2.3.3 Temperature-Dependent Power Flow for Distribution Systems

The available literature that refers directly to temperature-dependent power flow for radial systems is almost non-existent. The researchers that have worked towards a temperature-dependent power flow algorithm for distribution systems have employed a current summation, i.e. Kirchoff's-formulation based approach, to the BFS and have incorporated electrothermal coupling through the CIGRE [8] standard that outlines guidelines for the thermal behavior of overhead conductors. The authors of [28] propose a temperature-dependent BFS method for distribution systems considering the addition of distributed generation at one or more points in the network. However, this work only considers single-phase models of the test systems presented, assuming balanced conditions, and therefore is not a reasonably accurate representation of a distribution system. Also, only constant power loads are considered. They cite the CIGRE standard [8] as the resource used to implement the electrothermal coupling and [27] as the source of the BFS algorithm. An exhaustive-search algorithm is used to optimize the location of the distributed generation in order to minimize losses. In the course of this optimization, the effect of electrothermal coupling is considered. The authors found that by incorporating the conductor temperature to the power flow, they demonstrated differences of 8-13% in calculated total losses, depending on the system studied.

The lack of research into temperature-dependent power flow for radial distribution systems will begin to be addressed in the following chapters. The next chapter will describe the modeling of circuit components required for a distribution system power flow algorithm, namely line sections, transformers, voltage regulators, loads, and capacitor banks.

CHAPTER 3: COMPONENT MODELING FOR DISTRIBUTION SYSTEM POWER FLOW STUDIES

3.1 Overview

The sections that follow in this chapter will give explicit detailed formulations for the component modeling used in the implementation of the backward-forward sweep power flow algorithm described in Chapter 5. The component modeling in this chapter is taken from William H. Kersting's *Distribution System Modeling and Analysis*, 2nd edition [27], and in the case of the transformer and voltage regulator modeling, not every configuration possible or even described in [27] is presented, only the configurations that will be needed for the test system case studies presented in Chapter 6.

The shunt circuit elements presented are loads and capacitor banks. The load models in the subsections to follow are either lumped, that is concentrated at a single distribution node, or distributed, that is considered uniformly distributed along a branch between two or more nodes. The capacitor banks are presented for both wye and delta configurations, and both loads and capacitors are modeled with respect to their contribution to the node current at their associated nodes within the distribution system model.

The series circuit elements presented are transformers, line sections, and voltage regulators. All series circuit element derivations will be made with the aim of associating voltages at, and currents leaving, a node n with the voltage at, and current entering, a node m, as can be seen in the generalized series component diagram, Fig. 3.1.

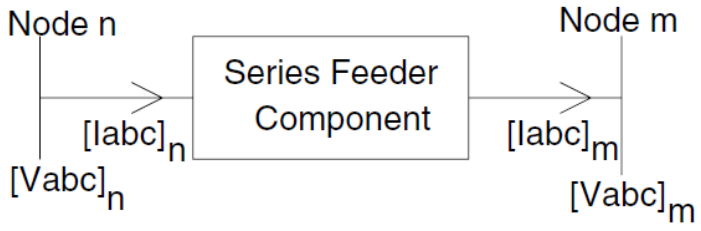

Figure 3.1: Generalized series component model [27]

These relationships can be written, for defining node n voltages and currents with respect to node m:

$$[V_{abc}]_n = [a]\,[V_{abc}]_m + [b]\,[I_{abc}]_m \tag{3.1}$$

$$[I_{abc}]_n = [c]\,[V_{abc}]_m + [d]\,[I_{abc}]_m \tag{3.2}$$

And relating node m voltages with respect to node n:

$$[V_{abc}]_m = [A]\,[V_{abc}]_n - [B]\,[I_{abc}]_m \tag{3.3}$$

In Eqs. 3.1-3.3, the voltages are line-to-neutral for a four-wire wye feeder or equivalent line-to-neutral for a three-wire delta system. For voltage regulators, the voltages are line-to-neutral for terminals that are connected to a four-wire wye, and line-to-line when connected to a three-wire delta. The purpose of the series component sections (sections 3.4, 3.5, 3.6) is to develop the a,b,c,d,A,B matrices necessary to perform the backward-forward sweep power flow developed in Chapter 5. The purpose of the shunt component sections (sections 3.2, 3.3, 3.7) is to develop the contribution to the node current due to the shunt element.

3.2 Lumped Load Models

This section presents lumped load models that are concentrated at a single distribution system node. Additionally, the three-phase lumped models are presented as either being wye- or delta-connnected, and of constant impedance, constant current, or constant power type. The modeling will be presented with respect to the load currents, as this is required of the power flow algorithm presented in Chapter 5. All models are initially defined by a nominal complex power per phase and an assumed line-to-neutral voltage for wye loads, and an assumed line-to-line voltage for delta loads. These quantities are known inputs of the power flow algorithm.

3.2.1 Wye Connection

For wye-connected loads, the notation for nominal complex powers and nominal line-to-neutral voltages is as follows:

$$\begin{aligned} &\text{Phase a} : |S_a|\angle\theta_a \text{ and } |V_{an}|\angle\delta_a \\ &\text{Phase b} : |S_b|\angle\theta_b \text{ and } |V_{bn}|\angle\delta_b \\ &\text{Phase c} : |S_c|\angle\theta_c \text{ and } |V_{cn}|\angle\delta_c \end{aligned} \tag{3.4}$$

The notation for calculated line-to-neutral voltages is as follows:

$$\begin{aligned} &\text{Phase a} : |\hat{V}_{an}|\angle\hat{\delta}_a \\ &\text{Phase b} : |\hat{V}_{bn}|\angle\hat{\delta}_b \\ &\text{Phase c} : |\hat{V}_{cn}|\angle\hat{\delta}_c \end{aligned} \tag{3.5}$$

3.2.1.1 Constant Impedance

Computing the line currents for wye-connected constant impedance loads begins by defining the constant impedance in terms of nominal complex power and nominal line-to-neutral voltage:

$$\begin{aligned} Z_a &= \frac{|V_{an}|^2}{S_a^*} = \frac{|V_{an}|^2}{|S_a|}\angle\theta_a = |Z_a|\angle\theta_a \\ Z_b &= \frac{|V_{bn}|^2}{S_b^*} = \frac{|V_{bn}|^2}{|S_b|}\angle\theta_b = |Z_b|\angle\theta_b \\ Z_c &= \frac{|V_{cn}|^2}{S_c^*} = \frac{|V_{cn}|^2}{|S_c|}\angle\theta_c = |Z_c|\angle\theta_c \end{aligned} \tag{3.6}$$

This impedance remains constant during the course of the power flow, but the load currents will change as a function of the calculated value of line-to-neutral voltage at each iteration:

$$\begin{aligned} I_a^L &= \frac{\hat{V}_{an}}{Z_a} = \frac{|\hat{V}_{an}|}{|Z_a|}(\angle\hat{\delta}_a - \angle\theta_a) = |I_a^L|\angle\alpha_a \\ I_b^L &= \frac{\hat{V}_{bn}}{Z_b} = \frac{|\hat{V}_{bn}|}{|Z_b|}(\angle\hat{\delta}_b - \angle\theta_b) = |I_b^L|\angle\alpha_b \\ I_c^L &= \frac{\hat{V}_{cn}}{Z_c} = \frac{|\hat{V}_{cn}|}{|Z_c|}(\angle\hat{\delta}_c - \angle\theta_c) = |I_c^L|\angle\alpha_c \end{aligned} \tag{3.7}$$

3.2.1.2 Constant Current

This constant current model allows the power factor of the load to remain constant by calculating a fixed magnitude for the current based on the nominal complex powers and nominal voltages. Then the angle of the current is computed during the power flow by using the calculated voltage angle at each iteration and the angle of the nominal complex power:

$$
\begin{aligned}
I_a^L &= \frac{|S_a|}{|V_{an}|}(\angle\hat{\delta}_a - \angle\theta_a) = |I_a^L|\angle\alpha_a \\
I_b^L &= \frac{|S_b|}{|V_{bn}|}(\angle\hat{\delta}_b - \angle\theta_b) = |I_b^L|\angle\alpha_b \\
I_c^L &= \frac{|S_c|}{|V_{cn}|}(\angle\hat{\delta}_c - \angle\theta_c) = |I_c^L|\angle\alpha_c
\end{aligned} \tag{3.8}
$$

3.2.1.3 Constant Power

The line currents entering the constant power loads are computed by using the nominal complex powers and calculated voltages:

$$
\begin{aligned}
I_a^L &= \left(\frac{S_a}{\hat{V}_{an}}\right)^* = \frac{|S_a|}{|\hat{V}_{an}|}(\angle\hat{\delta}_a - \angle\theta_a) = |I_a^L|\angle\alpha_a \\
I_b^L &= \left(\frac{S_b}{\hat{V}_{bn}}\right)^* = \frac{|S_b|}{|\hat{V}_{bn}|}(\angle\hat{\delta}_b - \angle\theta_b) = |I_b^L|\angle\alpha_b \\
I_c^L &= \left(\frac{S_c}{\hat{V}_{cn}}\right)^* = \frac{|S_c|}{|\hat{V}_{cn}|}(\angle\hat{\delta}_c - \angle\theta_c) = |I_c^L|\angle\alpha_c
\end{aligned} \tag{3.9}
$$

3.2.2 Delta Connection

For delta-connected loads, the notation for nominal complex powers and nominal line-to-line voltages is as follows:

$$
\begin{aligned}
&\text{Phase ab} : |S_{ab}|\angle\theta_{ab} \text{ and } |V_{ab}|\angle\delta_{ab} \\
&\text{Phase bc} : |S_{bc}|\angle\theta_{bc} \text{ and } |V_{bc}|\angle\delta_{bc} \\
&\text{Phase ca} : |S_{ca}|\angle\theta_{ca} \text{ and } |V_{ca}|\angle\delta_{ca}
\end{aligned} \tag{3.10}
$$

The notation for calculated line-to-line voltages is as follows:

$$\begin{aligned} &\text{Phase ab} : |\hat{V}_{ab}|\angle\hat{\delta}_{ab} \\ &\text{Phase bc} : |\hat{V}_{bc}|\angle\hat{\delta}_{bc} \\ &\text{Phase ca} : |\hat{V}_{ca}|\angle\hat{\delta}_{ca} \end{aligned} \tag{3.11}$$

In all delta-connected load cases, the line current, required for the power flow algorithm, is recovered from the delta load current by the application of Kirchoff's current law at the nodes of the delta:

$$\begin{bmatrix} I_a^L \\ I_b^L \\ I_c^L \end{bmatrix} = \begin{bmatrix} 1 & 0 & -1 \\ -1 & 1 & 0 \\ 0 & -1 & 1 \end{bmatrix} \begin{bmatrix} I_{ab}^L \\ I_{bc}^L \\ I_{ca}^L \end{bmatrix} \tag{3.12}$$

3.2.2.1 Constant Impedance

Computing the delta load currents for delta-connected constant impedance loads begins by defining the constant impedance in terms of nominal complex power and nominal line-to-line voltage:

$$\begin{aligned} Z_{ab} &= \frac{|V_{ab}|^2}{S_{ab}^*} = \frac{|V_{ab}|^2}{|S_{ab}|}\angle\theta_{ab} = |Z_{ab}|\angle\theta_{ab} \\ Z_{bc} &= \frac{|V_{bc}|^2}{S_{bc}^*} = \frac{|V_{bc}|^2}{|S_{bc}|}\angle\theta_{bc} = |Z_{bc}|\angle\theta_{bc} \\ Z_{ca} &= \frac{|V_{ca}|^2}{S_{ca}^*} = \frac{|V_{ca}|^2}{|S_{ca}|}\angle\theta_{ca} = |Z_{ca}|\angle\theta_{ca} \end{aligned} \tag{3.13}$$

This impedance remains constant during the course of the power flow, but the load currents will change as a function of the calculated value of line-to-line voltage at

each iteration:

$$
\begin{aligned}
I_{ab}^{L} &= \frac{\hat{V}_{ab}}{Z_{ab}} = \frac{|\hat{V}_{ab}|}{|Z_{ab}|}(\angle\hat{\delta}_{ab} - \angle\theta_{ab}) = |I_{ab}^{L}|\angle\alpha_{ab} \\
I_{bc}^{L} &= \frac{\hat{V}_{bc}}{Z_{bc}} = \frac{|\hat{V}_{bc}|}{|Z_{bc}|}(\angle\hat{\delta}_{bc} - \angle\theta_{bc}) = |I_{bc}^{L}|\angle\alpha_{bc} \\
I_{ca}^{L} &= \frac{\hat{V}_{ca}}{Z_{ca}} = \frac{|\hat{V}_{ca}|}{|Z_{ca}|}(\angle\hat{\delta}_{ca} - \angle\theta_{ca}) = |I_{ca}^{L}|\angle\alpha_{ca}
\end{aligned}
\tag{3.14}
$$

3.2.2.2 Constant Current

As in the wye-connected constant current load, this constant current model allows the power factor of the load to remain constant by calculating a fixed magnitude for the current based on the nominal complex powers and nominal voltages. Then the angle of the current is computed during the power flow by using the calculated voltage angle at each iteration and the angle of the nominal complex power:

$$
\begin{aligned}
I_{ab}^{L} &= \frac{|S_{ab}|}{|V_{ab}|}(\angle\hat{\delta}_{ab} - \angle\theta_{ab}) = |I_{ab}^{L}|\angle\alpha_{ab} \\
I_{bc}^{L} &= \frac{|S_{bc}|}{|V_{bc}|}(\angle\hat{\delta}_{bc} - \angle\theta_{bc}) = |I_{bc}^{L}|\angle\alpha_{bc} \\
I_{ca}^{L} &= \frac{|S_{ca}|}{|V_{ca}|}(\angle\hat{\delta}_{ca} - \angle\theta_{ca}) = |I_{ca}^{L}|\angle\alpha_{ca}
\end{aligned}
\tag{3.15}
$$

3.2.2.3 Constant Power

The delta load currents entering the constant power loads are computed by using the nominal complex powers and calculated voltages:

$$
\begin{aligned}
I_{ab}^{L} &= \left(\frac{S_{ab}}{\hat{V}_{ab}}\right)^{*} = \frac{|S_{ab}|}{|\hat{V}_{ab}|}(\angle\hat{\delta}_{ab} - \angle\theta_{ab}) = |I_{ab}^{L}|\angle\alpha_{ab} \\
I_{bc}^{L} &= \left(\frac{S_{bc}}{\hat{V}_{bc}}\right)^{*} = \frac{|S_{bc}|}{|\hat{V}_{bc}|}(\angle\hat{\delta}_{bc} - \angle\theta_{bc}) = |I_{bc}^{L}|\angle\alpha_{bc} \\
I_{ca}^{L} &= \left(\frac{S_{ca}}{\hat{V}_{ca}}\right)^{*} = \frac{|S_{ca}|}{|\hat{V}_{ca}|}(\angle\hat{\delta}_{ca} - \angle\theta_{ca}) = |I_{ca}^{L}|\angle\alpha_{ca}
\end{aligned}
\tag{3.16}
$$

3.3 Uniformly Distributed Load Model

Uniformly distributed load models, as opposed to lumped load models, assume that load is uniformly distributed along a line between two or more nodes. This is often a reasonable modeling choice in the case of uniform spacing of similarly sized loads along the length of a feeder lateral. In the derivation of an exact lumped load model of a uniformly distributed load [27], the load is modeled as constant current at uniform spacing of dx with the value of di.

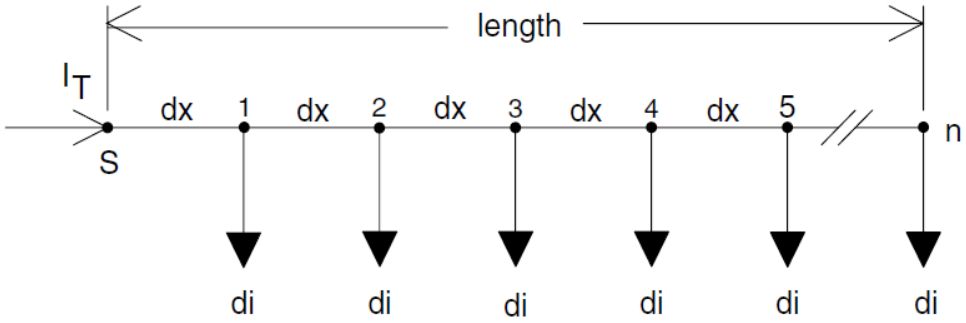

Figure 3.2: Uniformly distributed loads [27]

By reconciling the models of total voltage drop and total power loss developed in [27], the following exact lumped load model can be derived:

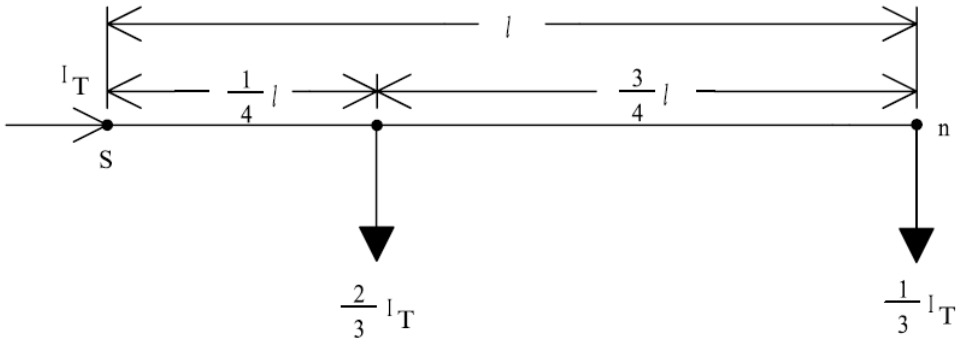

Figure 3.3: Exact lumped load model [27]

The interpretation of Fig. 3.3 is that one-third of the total distributed load is treated as a lumped load at the end of the line section containing the uniformly distributed load, and two-thirds is lumped one-fourth of the length of the line from the beginning of the line section. This load model will allow for the correct calculation of both total voltage drop and total power loss on the line section.

3.4 Line Models

In this section line models are presented for both overhead and underground lines. The models are given in terms of series impedance and shunt admittance, although in most practical cases the shunt admittance for short distribution system line lengths is negligible and can be neglected in the power flow. The modeling assumes unbalanced loading and untransposed line segments, and accommodates single-phase, two-phase, and three-phase line segments.

The series phase impedance and shunt phase admittance matrices developed in the following sections for overhead and underground lines will be used in the power flow algorithm to compute three-phase node voltages and currents for a node n and a node m that lie on either end of a line segment. Referring to Fig. 3.4, to relate the node voltages and the node currents at nodes n amd m, the relationships of Eqs. 3.1 and 3.2 can be written in the partitioned matrix form:

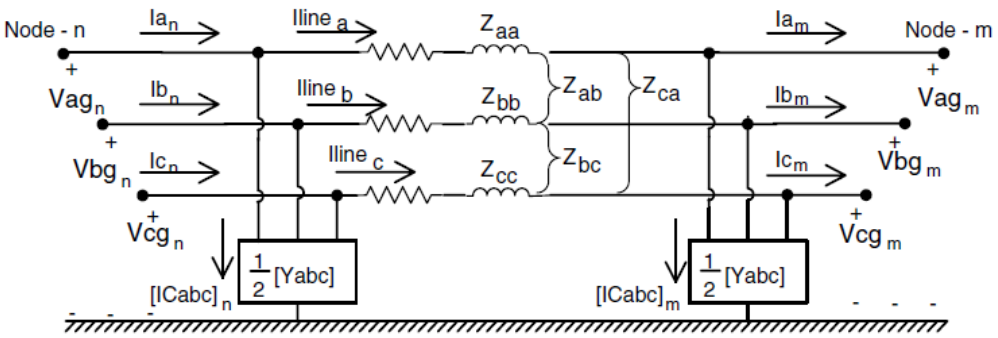

Figure 3.4: Three-phase line model [27]

$$\begin{bmatrix} [VLG_{abc}]_n \\ [I_{abc}]_n \end{bmatrix} = \begin{bmatrix} [a] & [b] \\ [c] & [d] \end{bmatrix} \begin{bmatrix} [VLG_{abc}]_m \\ [I_{abc}]_m \end{bmatrix} \tag{3.17}$$

where the generalized line matrices are,

$$[a] = [I] + \frac{1}{2}[Z_{abc}][Y_{abc}] \tag{3.18}$$

$$[b] = [Z_{abc}] \tag{3.19}$$

$$[c] = [Y_{abc}] + \frac{1}{4}[Y_{abc}][Z_{abc}][Y_{abc}] \tag{3.20}$$

$$[d] = [I] + \frac{1}{2}[Z_{abc}][Y_{abc}] \tag{3.21}$$

and,

$$[I] = \text{the 3 x 3 identity matrix} \tag{3.22}$$

$$[Z_{abc}] = [z_{abc}] \cdot \text{the length of the line} \tag{3.23}$$

$$[Y_{abc}] = [y_{abc}] \cdot \text{the length of the line} \tag{3.24}$$

The per unit length series impedance and shunt admittance matrices $[z_{abc}]$ and $[y_{abc}]$ will be developed in the following sections for overhead and underground lines. In practice, because the shunt admittance matrix is generally very small in distribution systems, the following approximations can be made:

$$[a] = [I] + \frac{1}{2}[Z_{abc}][Y_{abc}] \approx [I] \tag{3.25}$$

$$[b] = [Z_{abc}] \tag{3.26}$$

$$[c] = [Y_{abc}] + \frac{1}{4}[Y_{abc}][Z_{abc}][Y_{abc}] \approx [0] \tag{3.27}$$

$$[d] = [I] + \frac{1}{2}[Z_{abc}][Y_{abc}] \approx [I] \tag{3.28}$$

The relationship of Eq. 3.3, relating the voltages at node m to the voltages and currents at node n (note due to the approximations in Eqs. 3.25-3.28 the currents entering node m and leaving n are taken to be equal) are given by:

$$[V_{abc}]_m = [A][V_{abc}]_n - [B][I_{abc}]_m \tag{3.29}$$

where, following with the approximations in Eqs. 3.25-3.28,

$$[A] = [a]^{-1} \approx [I] \tag{3.30}$$

$$[B] = [a]^{-1}[b] \approx [b] \tag{3.31}$$

3.4.1 Overhead Lines

3.4.1.1 Series Impedance

For untransposed lines, the self and mutual components of the line inductance must be explicitly considered for each phase conductor. Both components are functions of the total magnetic fields surrounding a conductor and can be derived as:

$$\text{Self inductance} : L_{ii} = 2 \cdot 10^{-}7 \cdot \ln \frac{1}{GMR_i} \ \text{H/m} \tag{3.32}$$

$$\text{Mutual inductance} : L_{ij} = 2 \cdot 10^{-}7 \cdot \ln \frac{1}{D_{ij}} \ \text{H/m} \tag{3.33}$$

where the known quantities are,

$$D_{ij} = \text{Distance between centers of conductors } i \text{ and } j \text{ (ft.)}$$

$$GMR_i = \text{Geometric Mean Radius of conductor } i \text{ (ft.)}$$

Assuming a frequency of 60 Hz, and including a resistance term r_i in the self impedance term, which can be acquired from a resource with tabulated resistances such as [31], the self and mutual impedance values of the conductors, respectively, can be computed as:

$$z_{ii} = r_i + j0.12134 \cdot \ln \frac{1}{GMR_i} \ \Omega/\text{mile} \tag{3.34}$$

$$z_{ij} = j0.12134 \cdot \ln \frac{1}{D_{ij}} \ \Omega/\text{mile} \tag{3.35}$$

To take into account the return path of current through the ground in the self and mutual impedance terms, John Carson developed an approach utilizing an imaginary

earth conductor to represent the return path of current [57]. The derivation results in so-termed "primitive" impedance terms that are embedded with the effect of the ground return path. This approach is summarized in [27], and through the use of some minimal approximation, and with the assumption of a frequency of 60 Hz and an earth resistivity of 100 Ω-m, the following primitive impedance terms can be derived:

$$\hat{z}_{ii} = r_i + 0.09530 + 0.12134 \cdot \left(\ln \frac{1}{GMR_i} + 7.93402 \right) \quad \Omega/\text{mile} \tag{3.36}$$

$$\hat{z}_{ij} = 0.09530 + j0.12134 \cdot \left(\ln \frac{1}{D_{ij}} + 7.93402 \right) \quad \Omega/\text{mile} \tag{3.37}$$

Note the hat operator denotes these as primitive impedance terms. These terms are used to construct an n x n matrix where n is the number of conductors. For example, a four-wire grounded wye line segment will result in a 4 x 4 primitive impedance matrix, as seen below:

$$\left[\hat{z}_{primitive}\right] = \left[\begin{array}{ccc:c} \hat{z}_{aa} & \hat{z}_{ab} & \hat{z}_{ac} & \hat{z}_{an} \\ \hat{z}_{ba} & \hat{z}_{bb} & \hat{z}_{bc} & \hat{z}_{bn} \\ \hat{z}_{ca} & \hat{z}_{cb} & \hat{z}_{cc} & \hat{z}_{cn} \\ \hdashline \hat{z}_{na} & \hat{z}_{nb} & \hat{z}_{nc} & \hat{z}_{nn} \end{array}\right] \tag{3.38}$$

This matrix can be partitioned as:

$$\left[\hat{z}_{primitive}\right] = \left[\begin{array}{c:c} [\hat{z}_{ij}] & [\hat{z}_{in}] \\ \hdashline [\hat{z}_{nj}] & [\hat{z}_{nn}] \end{array}\right] \tag{3.39}$$

For application to the power flow algorithm presented in Chapter 5, this n x n primitive impedance matrix must be reduced to 3 x 3 phase impedance matrix which

consists of the equivalent self and mutual impedance terms. The method of Kron reduction will be used for the matrix reduction, as described below. For four-wire wye grounded line segments, we can consider the diagram of Fig. 3.5, and we make the assumption that the line has a multigrounded neutral, thus the neutral voltages on both ends of the segment are taken to be zero.

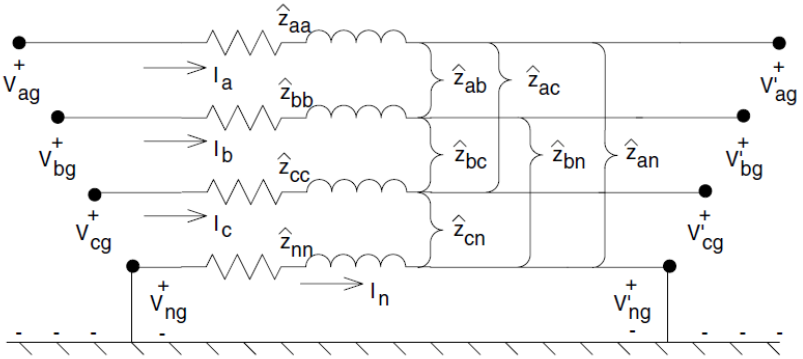

Figure 3.5: Four-wire wye grounded line segment [27]

Then using Kirchoff's voltage law, we can write:

$$\begin{bmatrix} V_{ag} \\ V_{bg} \\ V_{cg} \\ V_{ng} \end{bmatrix} = \begin{bmatrix} V'_{ag} \\ V'_{bg} \\ V'_{cg} \\ V'_{ng} \end{bmatrix} + \begin{bmatrix} \hat{z}_{aa} & \hat{z}_{ab} & \hat{z}_{ac} & \hat{z}_{an} \\ \hat{z}_{ba} & \hat{z}_{bb} & \hat{z}_{bc} & \hat{z}_{bn} \\ \hat{z}_{ca} & \hat{z}_{cb} & \hat{z}_{cc} & \hat{z}_{cn} \\ \hat{z}_{na} & \hat{z}_{nb} & \hat{z}_{nc} & \hat{z}_{nn} \end{bmatrix} \begin{bmatrix} I_a \\ I_b \\ I_c \\ I_n \end{bmatrix} \tag{3.40}$$

And in partitioned from, Eq. 3.40 can be written as:

$$\begin{bmatrix} [V_{abc}] \\ [V_{ng}] \end{bmatrix} = \begin{bmatrix} [V'_{abc}] \\ [V'_{ng}] \end{bmatrix} + \begin{bmatrix} [\hat{z}_{ij}] & [\hat{z}_{in}] \\ [\hat{z}_{nj}] & [\hat{z}_{nn}] \end{bmatrix} \begin{bmatrix} [I_{abc}] \\ [I_{ng}] \end{bmatrix} \tag{3.41}$$

Again, assuming that the line has a multigrounded neutral and the neutral voltages are equal to zero allows the following relationship to be developed [27]:

$$\left[z_{abc}\right] = \left[\hat{z}_{ij}\right] - \left[\hat{z}_{in}\right]\left[\hat{z}_{nn}\right]^{-1}\left[\hat{z}_{nj}\right] \tag{3.42}$$

The phase impedance matrix developed in Eq. 3.42 is used in the power flow algorithm of Chapter 5 and has the following form:

$$\left[z_{abc}\right] = \begin{bmatrix} z_{aa} & z_{ab} & z_{ac} \\ z_{ba} & z_{bb} & z_{bc} \\ z_{ca} & z_{cb} & z_{cc} \end{bmatrix} \quad \Omega/\text{mile} \tag{3.43}$$

For two-phase and single-phase lines, the primitive impedance matrices will be 3 x 3 and 2 x 2 respectively, which will reduce to 2 x 2 and 1 x 1 after the Kron reduction step in Eq. 3.42. These matrices can then be expanded to 3 x 3 with zero elements for the missing phases. The phase impedance matrix for a three-wire delta line does not require the Kron reduction step, and is composed of the $[\hat{z}_{ij}]$ portion of the primitive impedance matrix in Eq. 3.39.

3.4.1.2 Shunt Admittance

The shunt admittance of a line consists of both conductance and capacitive susceptance, although in practice the conductance is usually ignored as it is much smaller than the susceptance. The derivation of the self and mutual shunt admittance terms for an overhead line will employ the method of conductor images [57], [27], as can be seen graphically in Fig. 3.6, wherein each conductor is imagined as having an image conductor equidistant below ground as the overhead conductor is above ground. Using the method of conductors and their images, the self and mutual shunt admittance terms can be derived for an overhead line with the following information:

$$
\begin{aligned}
S_{ii} &= \text{distance from conductor } i \text{ to its image } i^{'} \text{ (ft)} \\
S_{ij} &= \text{distance from conductor } i \text{ to the image of conductor } j \text{ (ft)} \\
D_{ij} &= \text{distance from conductor } i \text{ to conductor } j \text{ (ft)} \\
RD_i &= \text{radius of conductor } i \text{ (ft.)}
\end{aligned}
\tag{3.44}
$$

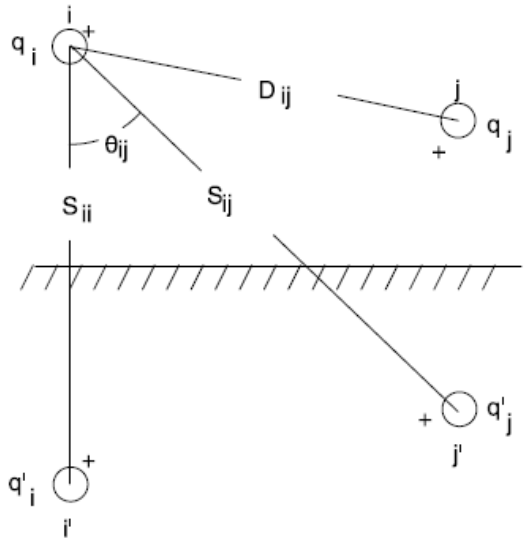

Figure 3.6: Conductors and images [27]

Then with the assumption of the relative permittivity of air as 1.0, the self and mutual primitive potential coefficient terms can be defined as:

$$\hat{P}_{ii} = 11.17689 \cdot \left(\ln \frac{S_{ii}}{RD_i} \right) \quad \text{mile}/\mu\text{F} \tag{3.45}$$

$$\hat{P}_{ij} = 11.17689 \cdot \left(\ln \frac{S_{ij}}{D_{ij}} \right) \quad \text{mile}/\mu\text{F} \tag{3.46}$$

The primitive potential coefficent matrix will be n x n where n is the number of

conductors. For a four-wire grounded wye line the matrix will be of the form:

$$\left[\hat{P}_{primitive}\right] = \left[\begin{array}{ccc:c} \hat{P}_{aa} & \hat{P}_{ab} & \hat{P}_{ac} & \hat{P}_{an} \\ \hat{P}_{ba} & \hat{P}_{bb} & \hat{P}_{bc} & \hat{P}_{bn} \\ \hat{P}_{ca} & \hat{P}_{cb} & \hat{P}_{cc} & \hat{P}_{cn} \\ \hdashline \hat{P}_{na} & \hat{P}_{nb} & \hat{P}_{nc} & \hat{P}_{nn} \end{array}\right] \tag{3.47}$$

This matrix can be partitioned as:

$$\left[\hat{P}_{primitive}\right] = \left[\begin{array}{c:c} [\hat{P}_{ij}] & [\hat{P}_{in}] \\ \hdashline [\hat{P}_{nj}] & [\hat{P}_{nn}] \end{array}\right] \tag{3.48}$$

Using the same assumption of the grounding of the neutral conductor as in section 3.4.1.1, the matrix can be reduced using Kron reduction as:

$$\left[P_{abc}\right] = \left[\hat{P}_{ij}\right] - \left[\hat{P}_{in}\right]\left[\hat{P}_{nn}\right]^{-1}\left[\hat{P}_{nj}\right] \tag{3.49}$$

The inverse of the potential coefficient matrix (Eq. 3.49) will give the capacitance matrix, such that the final expression for the phase shunt admittance matrix, neglecting conductance, is given by:

$$\left[y_{abc}\right] = j \cdot \omega \cdot \left[P_{abc}\right]^{-1} \quad \mu\text{S/mile} \tag{3.50}$$

where j denotes the unit imaginary number and $\omega = 2 \cdot \pi \cdot 60$.

3.4.2 Underground Lines

3.4.2.1 Series Impedance

In much the same manner as applied for overhead lines in section 3.4.1.1, the modified Carson's equations can be used to develop phase impedance matrices for underground cable. Two types of cable present in the test feeder cases in Chapter 6 will be addressed specifically in this thesis, concentric neutral cable and tape-shielded cable.

Concentric Neutral Cable

Fig. 3.7 shows the cross-section of a concentric neutral cable. The following data is required in order to apply Carson's equation and derive the phase impedance matrix:

d_c = phase conductor diameter (inches)

d_{od} = nominal diameter over the concentric neutrals (inches)

d_s = diameter of concentric neutral strand (inches)

GMR_c = Geometric Mean Radius of phase conductor (ft.)

GMR_s = Geometric Mean Radius of neutral conductor (ft.)

r_c = resistance of the phase conductor (Ω/mile)

r_n = resistance of the neutral conductor (Ω/mile)

k = number of individual neutral conductor strands

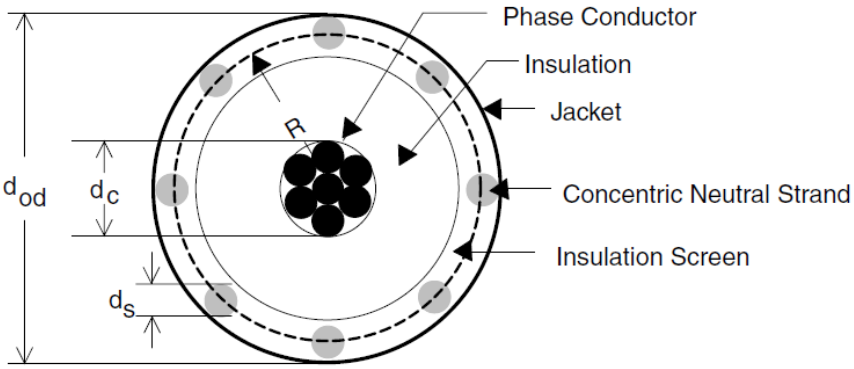

Figure 3.7: Concentric neutral cable cross-section [27]

The GMR and resistances above can be acquired by using tables such as those contained in [31]. For the concentric neutrals, equivalent GMR and resistance values must be obtained that represent the individual neutral conductors taken as a whole. The equivalent GMR of the concentric neutral taken is given as:

$$GMR_{cn} = \sqrt[k]{GMR_s \cdot k \cdot R^{k-1}} \text{ ft} \tag{3.51}$$

R is the radius of a circle passing through the center of the concentric neutral strands, as shown in Fig. 3.7, and can be calculated as:

$$R = \frac{d_{od} - d_s}{24} \text{ ft} \tag{3.52}$$

The equivalent resistance of the concentric neutral is:

$$r_{cn} = \frac{r_s}{k} \ \Omega/\text{mile} \tag{3.53}$$

The spacings (D_{ij}) between phase conductors and concentric neutrals are also

needed to compute the elements of the primitive impedance matrix. Three general spacings are required:

Concentric neutral to its own phase conductor :

$D_{ij} = R$ (Eq. 3.52) for concentric neutral or phase conductor i and j (ft) (3.54)

Concentric neutral to adjacent concentric neutral :

$D_{ij} =$ center to center distance of the phase conductors i and j (ft) (3.55)

Concentric neutral to adjacent phase conductor :

$$D_{ij} = \sqrt[k]{D_{nm}^k - R^k} \text{ (ft)} \tag{3.56}$$

For this last case, where the distance between adjacent cables is much greater than the radius R, Eq. 3.56 can be approximated as being equal to the distance between adjacent cables.

Using the development above, the self and mutual elements, respectively, of the primitive impedance matrix can be derived as:

$$\hat{z}_{ii} = r_i + 0.09530 + 0.12134 \cdot \left(\ln \frac{1}{GMR_i} + 7.93402 \right) \quad \Omega/\text{mile} \tag{3.57}$$

$$\hat{z}_{ij} = 0.09530 + j0.12134 \cdot \left(\ln \frac{1}{D_{ij}} + 7.93402 \right) \quad \Omega/\text{mile} \tag{3.58}$$

where,

D_{ij} = Distance as defined by Eqs. 3.54-3.56

GMR_i = Equivalent Geometric Mean Radius of concentric neutral (Eq. 3.51) or Geometric Mean Radius of phase conductor i (ft)

r_i = Equivalent resistance of concentric neutral i (Eq. 3.53) or resistance of phase conductor i (Ω/mile)

A grounded wye line segment consisting of three concentric neutral cables will have a 6 x 6 primitive impedance matrix, taking into account the mutual coupling between the three phase conductors and three equivalent neutral conductors ($n1$, $n2$, $n3$), as seen below:

$$\left[\hat{z}_{primitive}\right] = \left[\begin{array}{ccc:ccc} \hat{z}_{aa} & \hat{z}_{ab} & \hat{z}_{ac} & \hat{z}_{an1} & \hat{z}_{an2} & \hat{z}_{an3} \\ \hat{z}_{ba} & \hat{z}_{bb} & \hat{z}_{bc} & \hat{z}_{bn1} & \hat{z}_{bn2} & \hat{z}_{bn3} \\ \hat{z}_{ca} & \hat{z}_{cb} & \hat{z}_{cc} & \hat{z}_{cn1} & \hat{z}_{cn2} & \hat{z}_{cn3} \\ \hdashline \hat{z}_{n1a} & \hat{z}_{n1b} & \hat{z}_{n1c} & \hat{z}_{n1n1} & \hat{z}_{n1n2} & \hat{z}_{n1n3} \\ \hat{z}_{n2a} & \hat{z}_{n2b} & \hat{z}_{n2c} & \hat{z}_{n2n1} & \hat{z}_{n2n2} & \hat{z}_{n2n3} \\ \hat{z}_{n3a} & \hat{z}_{n3b} & \hat{z}_{n3c} & \hat{z}_{n3n1} & \hat{z}_{n3n2} & \hat{z}_{n3n3} \end{array}\right] \tag{3.59}$$

This matrix can be partitioned as:

$$\left[\hat{z}_{primitive}\right] = \left[\begin{array}{c:c} [\hat{z}_{ij}] & [\hat{z}_{in}] \\ \hdashline [\hat{z}_{nj}] & [\hat{z}_{nn}] \end{array}\right] \tag{3.60}$$

And using Kron reduction as in section 3.4.1.1, the phase impedance matrix can be derived by:

$$\left[z_{abc}\right] = \left[\hat{z}_{ij}\right] - \left[\hat{z}_{in}\right]\left[\hat{z}_{nn}\right]^{-1}\left[\hat{z}_{nj}\right] = \begin{bmatrix} z_{aa} & z_{ab} & z_{ac} \\ z_{ba} & z_{bb} & z_{bc} \\ z_{ca} & z_{cb} & z_{cc} \end{bmatrix} \quad \Omega/\text{mile} \tag{3.61}$$

Tape-Shielded Cable

Fig. 3.8 shows the cross-section of a tape-shielded cable. The following data is required in order to apply Carson's equation and derive the phase impedance matrix:

$$\begin{aligned} d_c &= \text{phase conductor diameter (inches)} \\ d_s &= \text{outside diameter of tape shield (inches)} \\ d_{od} &= \text{outside diameter over jacket (inches)} \\ T &= \text{thickness of copper tape in mils} \end{aligned} \tag{3.62}$$

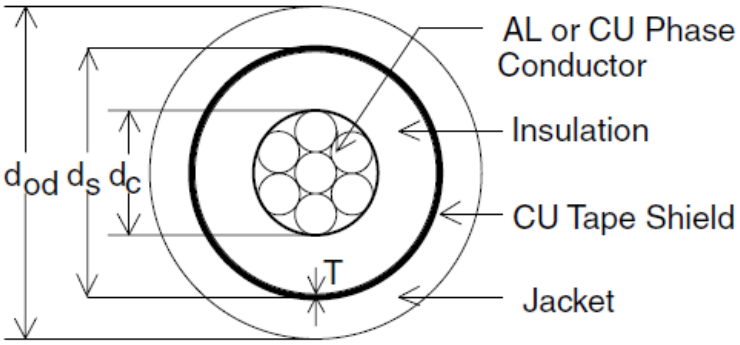

Figure 3.8: Tape-shielded cable cross-section [27]

As in the previous cases of bare overhead line conductors (section 3.4.1.1) and concentric neutral cable (section 3.4.2.1), the modified Carson's equations will be

applied to derive the phase impedance matrix for the line section. The GMR and resistances of the phase and neutral conductors required in the formulations that follow can be acquired by using tables such as those contained in [31]. The resistance of the tape shield is given by the following, where ρ is the resistivity of the shield and must be expressed in Ω-meters at $50°C$:

$$r_{shield} = 7.9385 \cdot 10^8 \cdot \frac{\rho}{d_s \cdot T} \quad \Omega/\text{mile} \tag{3.63}$$

The GMR of the tape shield is the radius of a circle passing through the middle of the shield and can be calculated as:

$$GMR_{shield} = \frac{d_s - \frac{T}{1000}}{24} \quad \text{ft} \tag{3.64}$$

And as in the case of the concentric neutral cable, various spacings need to be defined to calculate the mutual impedance terms:

Tape shield to its own phase conductor :

$D_{ij} = GMR_{shield}$ (Eq. 3.64) for tape shield or phase conductor i and j (ft) (3.65)

Tape shield to adjacent tape shield :

D_{ij} = center to center distance of the phase conductors i and j (ft) (3.66)

Tape shield to adjacent phase or neutral conductor :

D_{ij} = center to center distance of the phase conductors i and j (ft) (3.67)

The self and mutual impedance terms of the primitive impedance matrix can subsequently be derived as:

$$\hat{z}_{ii} = r_i + 0.09530 + 0.12134 \cdot \left(\ln \frac{1}{GMR_i} + 7.93402 \right) \quad \Omega/\text{mile} \tag{3.68}$$

$$\hat{z}_{ij} = 0.09530 + j0.12134 \cdot \left(\ln \frac{1}{D_{ij}} + 7.93402 \right) \quad \Omega/\text{mile} \tag{3.69}$$

where,

D_{ij} = Distance as defined by Eqs. 3.65-3.67

GMR_i = Geometric Mean Radius of tape shield (Eq. 3.64), phase, or neutral conductor i (ft)

r_i = Resistance of tape shield (Eq. 3.63), phase, or neutral conductor i (Ω/mile)

For a single-phase tape-shielded cable with a neutral conductor, the primitive impedance matrix will have the following form, with numbering such that the phase conductor is 1, the tape shield is 2, and the ground or neutral is 3:

$$\left[\hat{z}_{primitive}\right] = \left[\begin{array}{c|cc} \hat{z}_{11} & \hat{z}_{12} & \hat{z}_{13} \\ \hline \hat{z}_{21} & \hat{z}_{22} & \hat{z}_{23} \\ \hat{z}_{31} & \hat{z}_{32} & \hat{z}_{33} \end{array}\right] \tag{3.70}$$

This matrix can be partitioned as:

$$\left[\hat{z}_{primitive}\right] = \left[\begin{array}{c|c} [\hat{z}_{ij}] & [\hat{z}_{in}] \\ \hline [\hat{z}_{nj}] & [\hat{z}_{nn}] \end{array}\right] \tag{3.71}$$

And using Kron reduction as in section 3.4.1.1 and section 3.4.2.1, the phase impedance matrix can be derived as follows, in this case reducing to a single impedance term to represent the equivalent single-phase impedance of the tape-shielded cable and the neutral conductor:

$$\left[z_{abc}\right] = \left[\hat{z}_{ij}\right] - \left[\hat{z}_{in}\right]\left[\hat{z}_{nn}\right]^{-1}\left[\hat{z}_{nj}\right] = \left[\ z_{1p}\ \right] \quad \Omega/\text{mile} \tag{3.72}$$

Assuming the conductor is associated with phase A, the 3 x 3 impedance matrix needed for the power flow algorithm can be represented as:

$$\left[z_{abc}\right] = \begin{bmatrix} z_{1p} & 0 & 0 \\ 0 & 0 & 0 \\ 0 & 0 & 0 \end{bmatrix} \quad \Omega/\text{mile} \tag{3.73}$$

3.4.2.2 Shunt Admittance

Concentric Neutral Cable

To calculate the phase shunt admittance matrix for a concentric neutral cable, and referencing Fig. 3.9, the following information is required:

R_b = radius of a circle passing through the centers of the neutral strands

d_c = phase conductor diameter

d_s = diameter of concentric neutral strand

k = number of individual neutral conductor strands

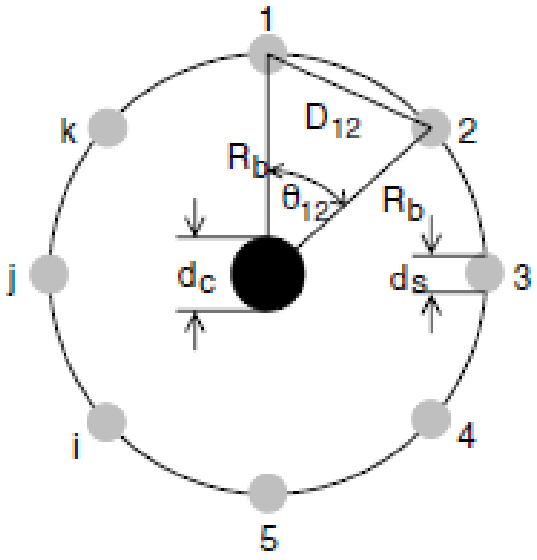

Figure 3.9: Concentric neutral cable cross-section [27]

And defining:

$$RD_c = \frac{d_c}{2} \tag{3.74}$$

$$RD_s = \frac{d_s}{2} \tag{3.75}$$

Since the concentric neutral strands are assumed grounded and therefore at the same potential, it is only necessary to find the capacitance and subsequent shunt susceptance for one phase cable. For a multiphase section, the shunt susceptance values for each cable will be the same. Additionally, it is assumed that due to the stranding of the concentric neutrals, the electric field that generates the capacitance and subsequent susceptance is confined to the boundary of the concentric neutral strands, and no mutual coupling between phase conductor capacitance occurs. Using the derivation presented in [27], and using a relative permittivity value of 2.3 (conservatively chosen as the minimum value of XLPE cable) the shunt admittance term for a concentric neutral cable is given by the following, where j is the unit imaginary

number:

$$y_{ag} = y_{bg} = y_{cg} = j \cdot \frac{77.3619}{\ln\left(\frac{R_b}{RD_c}\right) - \frac{1}{k}\ln\left(\frac{k \cdot RD_s}{R_b}\right)} \tag{3.76}$$

Note that the dimensions of the radii and diameters are not crucial as long as they are consistent, as their final use will be as a ratio used in the argument of the natural log function. Since the shunt admittance term given by Eq. 3.76 will be the same for each phase cable, and no mutual coupling is assumed, the 3 x 3 phase shunt admittance matrix for a three-phase section, neglecting susceptance, is given as:

$$\left[y_{abc}\right] = \begin{bmatrix} y_{ag} & 0 & 0 \\ 0 & y_{bg} & 0 \\ 0 & 0 & y_{cg} \end{bmatrix} \ \mu\text{S/mile} \tag{3.77}$$

Tape-Shielded Cable

To derive the phase shunt admittance matrix for tape-shielded cable, we refer to Eq. 3.76 in the previous section. The tape-shielded cable can be considered as a concentric neutral cable where the number of strands k has become infinite. With this notion, the second term in the denominator of Eq. 3.76 becomes zero, and the equation for the shunt admittance term of a tape-shielded conductor becomes:

$$y_{ag} = y_{bg} = y_{cg} = j \cdot \frac{77.3619}{\ln\left(\frac{R_b}{RD_c}\right)} \tag{3.78}$$

And making use again of the tape-shielded cable parameters:

$$
\begin{aligned}
d_c &= \text{phase conductor diameter (inches)} \\
d_s &= \text{outside diameter of tape shield (inches)} \\
d_{od} &= \text{outside diameter over jacket (inches)} \\
T &= \text{thickness of copper tape in mils}
\end{aligned}
\tag{3.79}
$$

And defining:

$$R_b = \frac{d_s - T}{2} \tag{3.80}$$

$$RD_c = \frac{d_c}{2} \tag{3.81}$$

Considering, for example, a single-phase line segment associated with phase A, the corresponding 3 x 3 phase shunt admittance matrix would be given as:

$$\left[y_{abc}\right] = \begin{bmatrix} y_{ag} & 0 & 0 \\ 0 & 0 & 0 \\ 0 & 0 & 0 \end{bmatrix} \quad \mu\text{S/mile} \tag{3.82}$$

3.5 Three-Phase Transformer Models

In this section three-phase transformer models will be derived for use in the power flow algorithm presented in Chapter 5. The models will be presented with respect to the generalized series component matrices as was done for line models (section 3.4), and is described in general in the overview of this chapter (section 3.1). The

relationships developed, for a node n (source side, capital letters A,B,C,N) and a node m (load side, lowercase letters, a,b,c,d), as visualized in Fig. 3.10, are given by:

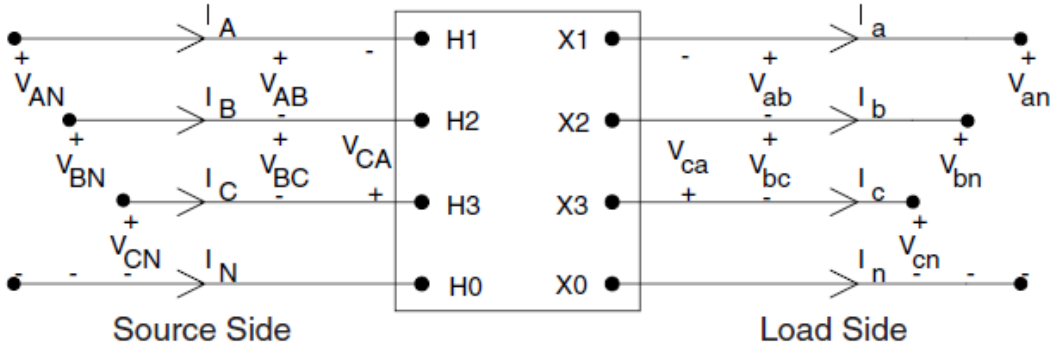

Figure 3.10: Generalized three-phase transformer model [27]

$$[VLN_{ABC}] = [a_t]\,[VLN_{abc}] + [b_t]\,[I_{abc}] \tag{3.83}$$

$$[I_{ABC}] = [c_t]\,[VLN_{abc}] + [d_t]\,[I_{abc}] \tag{3.84}$$

And relating node m (load side) voltages with respect to node n (source side):

$$[VLN_{abc}] = [A_t]\,[VLN_{ABC}] - [B_t]\,[I_{abc}] \tag{3.85}$$

The purpose of the following sections will be to develop these generalized matrices a_t, b_t, c_t, d_t, A_t, and B_t for use in the power flow algorithm. Three step-down connection types will be detailed, as required by the case studies in Chapter 6: grounded wye-grounded wye, delta-grounded wye, and delta-delta.

It should be noted that transformer impedances are often given as a percent impedance on the transformer base. For the power flow algorithm presented in Chapter 5 these impedances must be converted to Ohms. Referred to the low voltage side of the transformer, the impedances Z_t in Ohms can be obtained from the percentage

impedance by:

$$Z_t = \frac{VLL_{low}^2}{S} \cdot (R\% + jX\%) \quad (\Omega) \tag{3.86}$$

where,

VLL_{low} = transformer nominal line-to-line voltage on the low side in volts

S = transformer nominal three-phase apparent power in VA

$R\%$ = given percentage resistance for transformer

$X\%$ = given percentage reactance for transformer

j = unit imaginary number

3.5.1 Grounded Wye-Grounded Wye Step-Down Connection

The grounded wye-grounded wye connection can be visualized in Fig. 3.11.

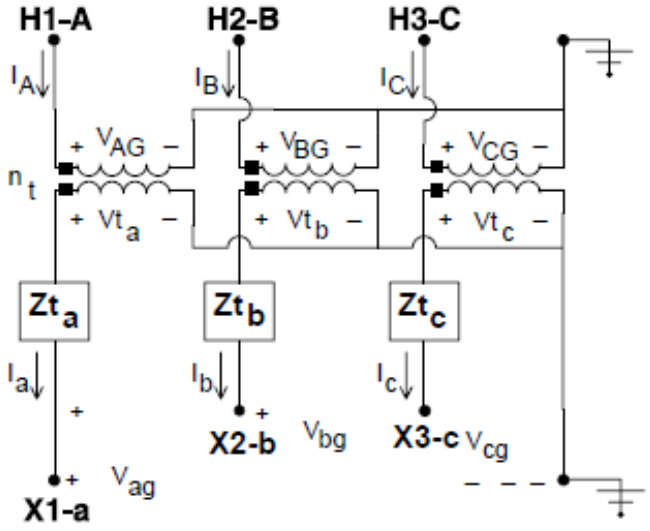

Figure 3.11: Grounded wye-grounded wye transformer connection [27]

The line-to-ground voltages on the primary side are related to the ideal transformer voltages by:

$$\begin{bmatrix} V_{AG} \\ V_{BG} \\ V_{CG} \end{bmatrix} = \begin{bmatrix} n_t & 0 & 0 \\ 0 & n_t & 0 \\ 0 & 0 & n_t \end{bmatrix} \begin{bmatrix} V_{ta} \\ V_{tb} \\ V_{tc} \end{bmatrix} \tag{3.87}$$

where the turns ratio, n_t, is defined for the step-down connection as:

$$n_t = \frac{VLN_{RatedHighSide}}{VLN_{RatedLowSide}} \tag{3.88}$$

The ideal transformer voltages can be defined, with reference to Fig. 3.11, as:

$$\begin{bmatrix} V_{ta} \\ V_{tb} \\ V_{tc} \end{bmatrix} = \begin{bmatrix} V_{ag} \\ V_{bg} \\ V_{cg} \end{bmatrix} + \begin{bmatrix} Z_{ta} & 0 & 0 \\ 0 & Z_{tb} & 0 \\ 0 & 0 & Z_{tc} \end{bmatrix} \begin{bmatrix} I_a \\ I_b \\ I_c \end{bmatrix} \tag{3.89}$$

Substituting Eq. 3.89 into Eq. 3.87 yields the following expression that is of the form of Eq. 3.83:

$$\begin{bmatrix} V_{AG} \\ V_{BG} \\ V_{CG} \end{bmatrix} = \begin{bmatrix} n_t & 0 & 0 \\ 0 & n_t & 0 \\ 0 & 0 & n_t \end{bmatrix} \begin{bmatrix} V_{ag} \\ V_{bg} \\ V_{cg} \end{bmatrix} + \begin{bmatrix} n_t & 0 & 0 \\ 0 & n_t & 0 \\ 0 & 0 & n_t \end{bmatrix} \begin{bmatrix} Z_{ta} & 0 & 0 \\ 0 & Z_{tb} & 0 \\ 0 & 0 & Z_{tc} \end{bmatrix} \begin{bmatrix} I_a \\ I_b \\ I_c \end{bmatrix} \tag{3.90}$$

Therefore, for the generalized transformer matrices of Eq. 3.83:

$$[a_t] = \begin{bmatrix} n_t & 0 & 0 \\ 0 & n_t & 0 \\ 0 & 0 & n_t \end{bmatrix} \tag{3.91}$$

$$[b_t] = \begin{bmatrix} Z_{ta} \cdot n_t & 0 & 0 \\ 0 & Z_{tb} \cdot n_t & 0 \\ 0 & 0 & Z_{tc} \cdot n_t \end{bmatrix} \tag{3.92}$$

The primary line currents as a function of the secondary line currents are given by:

$$\begin{bmatrix} I_A \\ I_B \\ I_C \end{bmatrix} = \begin{bmatrix} \frac{1}{n_t} & 0 & 0 \\ 0 & \frac{1}{n_t} & 0 \\ 0 & 0 & \frac{1}{n_t} \end{bmatrix} \begin{bmatrix} I_a \\ I_b \\ I_c \end{bmatrix} \tag{3.93}$$

Therefore, for the generalized transformer matrices of Eq. 3.84:

$$[c_t] = \begin{bmatrix} 0 & 0 & 0 \\ 0 & 0 & 0 \\ 0 & 0 & 0 \end{bmatrix} \tag{3.94}$$

$$[d_t] = \begin{bmatrix} \frac{1}{n_t} & 0 & 0 \\ 0 & \frac{1}{n_t} & 0 \\ 0 & 0 & \frac{1}{n_t} \end{bmatrix} \tag{3.95}$$

Solving Eq. 3.90 for the secondary line-to-ground voltages gives the following, which is of the form of Eq. 3.85:

$$\begin{bmatrix} V_{ag} \\ V_{bg} \\ V_{cg} \end{bmatrix} = \begin{bmatrix} n_t & 0 & 0 \\ 0 & n_t & 0 \\ 0 & 0 & n_t \end{bmatrix}^{-1} \begin{bmatrix} V_{AG} \\ V_{BG} \\ V_{CG} \end{bmatrix} - \begin{bmatrix} Z_{ta} & 0 & 0 \\ 0 & Z_{tb} & 0 \\ 0 & 0 & Z_{tc} \end{bmatrix} \begin{bmatrix} I_a \\ I_b \\ I_c \end{bmatrix} \tag{3.96}$$

Therefore, for the generalized transformer matrices of Eq. 3.85:

$$[A_t] = \begin{bmatrix} n_t & 0 & 0 \\ 0 & n_t & 0 \\ 0 & 0 & n_t \end{bmatrix}^{-1} = \begin{bmatrix} \frac{1}{n_t} & 0 & 0 \\ 0 & \frac{1}{n_t} & 0 \\ 0 & 0 & \frac{1}{n_t} \end{bmatrix} \tag{3.97}$$

$$[B_t] = \begin{bmatrix} Z_{ta} & 0 & 0 \\ 0 & Z_{tb} & 0 \\ 0 & 0 & Z_{tc} \end{bmatrix} \tag{3.98}$$

3.5.2 Delta-Grounded Wye Step-Down Connection

The delta-grounded wye connection can be visualized in Fig. 3.12. The model developed for this connection type will utilize a standard American thirty-degree step-down connection whereby the source side line-to-line voltages lead the load side line-to-line voltages by 30 degrees, and the source side line current leads the load side line current by 30 degrees.

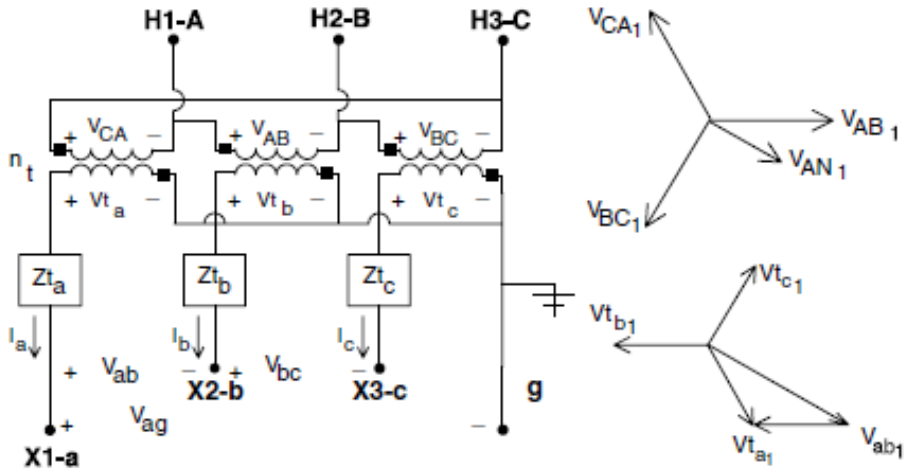

Figure 3.12: Delta-grounded wye transformer connection and positive sequence phasor diagrams [27]

The line-to-line voltages on the primary side are related to the ideal transformer voltages by:

$$\begin{bmatrix} V_{AB} \\ V_{BC} \\ V_{CA} \end{bmatrix} = \begin{bmatrix} 0 & -n_t & 0 \\ 0 & 0 & -n_t \\ -n_t & 0 & 0 \end{bmatrix} \begin{bmatrix} V_{ta} \\ V_{tb} \\ V_{tc} \end{bmatrix} \tag{3.99}$$

where the turns ratio, n_t, is defined for the step-down connection as:

$$n_t = \frac{VLL_{RatedHighSide}}{VLN_{RatedLowSide}} \tag{3.100}$$

The relationship between the ideal transformer voltages and the line-to-ground voltages and line currents on the secondary side is given by:

$$\begin{bmatrix} V_{ta} \\ V_{tb} \\ V_{tc} \end{bmatrix} = \begin{bmatrix} V_{ag} \\ V_{bg} \\ V_{cg} \end{bmatrix} + \begin{bmatrix} Z_{ta} & 0 & 0 \\ 0 & Z_{tb} & 0 \\ 0 & 0 & Z_{tc} \end{bmatrix} \begin{bmatrix} I_a \\ I_b \\ I_c \end{bmatrix} \tag{3.101}$$

To derive a relationship between the ideal transformer voltages and the equivalent line-to-neutral voltages on the primary side, the theory of symmetrical components is applied. After derivation detailed in [27], this relationship can be written as:

$$\begin{bmatrix} V_{AN} \\ V_{BN} \\ V_{CN} \end{bmatrix} = \frac{-n_t}{3} \begin{bmatrix} 0 & 2 & 1 \\ 1 & 0 & 2 \\ 2 & 1 & 0 \end{bmatrix} \begin{bmatrix} V_{ta} \\ V_{tb} \\ V_{tc} \end{bmatrix} \tag{3.102}$$

Substituting Eq. 3.101 into Eq. 3.102 yields the following expression that is of the form of Eq. 3.83:

$$\begin{bmatrix} V_{AN} \\ V_{BN} \\ V_{CN} \end{bmatrix} = \frac{-n_t}{3} \begin{bmatrix} 0 & 2 & 1 \\ 1 & 0 & 2 \\ 2 & 1 & 0 \end{bmatrix} \begin{bmatrix} V_{ag} \\ V_{bg} \\ V_{cg} \end{bmatrix} + \frac{-n_t}{3} \begin{bmatrix} 0 & 2 & 1 \\ 1 & 0 & 2 \\ 2 & 1 & 0 \end{bmatrix} \begin{bmatrix} Z_{ta} & 0 & 0 \\ 0 & Z_{tb} & 0 \\ 0 & 0 & Z_{tc} \end{bmatrix} \begin{bmatrix} I_a \\ I_b \\ I_c \end{bmatrix} \tag{3.103}$$

Therefore, for the generalized transformer matrices of Eq. 3.83:

$$[a_t] = \frac{-n_t}{3}\begin{bmatrix} 0 & 2 & 1 \\ 1 & 0 & 2 \\ 2 & 1 & 0 \end{bmatrix} \tag{3.104}$$

$$[b_t] = \frac{-n_t}{3}\begin{bmatrix} 0 & 2Z_{tb} & Z_{tc} \\ Z_{ta} & 0 & 2Z_{tc} \\ 2Z_{ta} & Z_{tb} & 0 \end{bmatrix} \tag{3.105}$$

Applying Kirchoff's current law, the line currents as a function of the delta currents are given by:

$$\begin{bmatrix} I_A \\ I_B \\ I_C \end{bmatrix} = \begin{bmatrix} 1 & -1 & 0 \\ 0 & 1 & -1 \\ -1 & 0 & 1 \end{bmatrix} \begin{bmatrix} I_{AC} \\ I_{BA} \\ I_{CB} \end{bmatrix} \tag{3.106}$$

And the equation relating the delta primary currents to the secondary line currents is given by:

$$\begin{bmatrix} I_{AC} \\ I_{BA} \\ I_{CB} \end{bmatrix} = \begin{bmatrix} \frac{1}{n_t} & 0 & 0 \\ 0 & \frac{1}{n_t} & 0 \\ 0 & 0 & \frac{1}{n_t} \end{bmatrix} \begin{bmatrix} I_a \\ I_b \\ I_c \end{bmatrix} \tag{3.107}$$

Substituting Eq. 3.107 into Eq. 3.106 yields the following expression that is of the form of Eq. 3.84:

$$\begin{bmatrix} I_A \\ I_B \\ I_C \end{bmatrix} = \begin{bmatrix} 1 & -1 & 0 \\ 0 & 1 & -1 \\ -1 & 0 & 1 \end{bmatrix} \begin{bmatrix} \frac{1}{n_t} & 0 & 0 \\ 0 & \frac{1}{n_t} & 0 \\ 0 & 0 & \frac{1}{n_t} \end{bmatrix} \begin{bmatrix} I_a \\ I_b \\ I_c \end{bmatrix} \tag{3.108}$$

Therefore, for the generalized transformer matrices of Eq. 3.84:

$$[c_t] = \begin{bmatrix} 0 & 0 & 0 \\ 0 & 0 & 0 \\ 0 & 0 & 0 \end{bmatrix} \tag{3.109}$$

$$[d_t] = \frac{1}{n_t} \begin{bmatrix} 1 & -1 & 0 \\ 0 & 1 & -1 \\ -1 & 0 & 1 \end{bmatrix} \tag{3.110}$$

Solving Eq. 3.99 for the ideal secondary voltages gives the following:

$$\begin{bmatrix} V_{ta} \\ V_{tb} \\ V_{tc} \end{bmatrix} = \begin{bmatrix} 0 & -n_t & 0 \\ 0 & 0 & -n_t \\ -n_t & 0 & 0 \end{bmatrix}^{-1} \begin{bmatrix} V_{AB} \\ V_{BC} \\ V_{CA} \end{bmatrix} \tag{3.111}$$

And the line-to-line voltages as a function of the equivalent line-to-neutral voltages are:

$$\begin{bmatrix} V_{AB} \\ V_{BC} \\ V_{CA} \end{bmatrix} = \begin{bmatrix} 1 & -1 & 0 \\ 0 & 1 & -1 \\ -1 & 0 & 1 \end{bmatrix} \begin{bmatrix} V_{AN} \\ V_{BN} \\ V_{CN} \end{bmatrix} \tag{3.112}$$

Substituting Eq. 3.112 into Eq. 3.111 yields the following expression:

$$\begin{bmatrix} V_{ta} \\ V_{tb} \\ V_{tc} \end{bmatrix} = \begin{bmatrix} 0 & -n_t & 0 \\ 0 & 0 & -n_t \\ -n_t & 0 & 0 \end{bmatrix}^{-1} \begin{bmatrix} 1 & -1 & 0 \\ 0 & 1 & -1 \\ -1 & 0 & 1 \end{bmatrix} \begin{bmatrix} V_{AN} \\ V_{BN} \\ V_{CN} \end{bmatrix} \tag{3.113}$$

And substituting Eq. 3.101 into Eq. 3.113 and rearranging yields the following, which is of the form of Eq. 3.85:

$$\begin{bmatrix} V_{ag} \\ V_{bg} \\ V_{cg} \end{bmatrix} = \frac{1}{n_t} \begin{bmatrix} 1 & 0 & -1 \\ -1 & 1 & 0 \\ 0 & -1 & 1 \end{bmatrix} \begin{bmatrix} V_{AN} \\ V_{BN} \\ V_{CN} \end{bmatrix} - \begin{bmatrix} Z_{ta} & 0 & 0 \\ 0 & Z_{tb} & 0 \\ 0 & 0 & Z_{tc} \end{bmatrix} \begin{bmatrix} I_a \\ I_b \\ I_c \end{bmatrix} \tag{3.114}$$

Therefore, for the generalized transformer matrices of Eq. 3.85:

$$[A_t] = \frac{1}{n_t} \begin{bmatrix} 1 & 0 & -1 \\ -1 & 1 & 0 \\ 0 & -1 & 1 \end{bmatrix} \tag{3.115}$$

$$[B_t] = \begin{bmatrix} Z_{ta} & 0 & 0 \\ 0 & Z_{tb} & 0 \\ 0 & 0 & Z_{tc} \end{bmatrix} \tag{3.116}$$

3.5.3 Delta-Delta Step-Down Connection

The delta-delta connection can be visualized in Fig. 3.13.

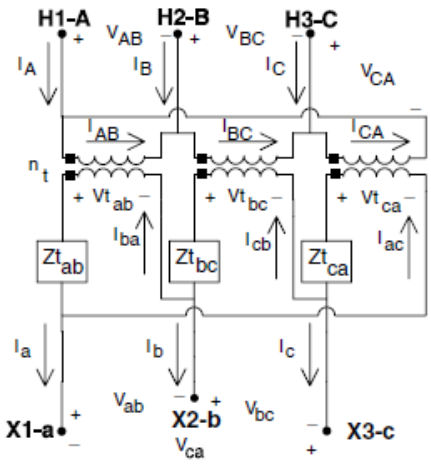

Figure 3.13: Delta-delta transformer connection diagram [27]

Referring to Fig. 3.13, the line-to-line voltages on the primary side are related to the ideal transformer voltages by:

$$\begin{bmatrix} V_{AB} \\ V_{BC} \\ V_{CA} \end{bmatrix} = \begin{bmatrix} n_t & 0 & 0 \\ 0 & n_t & 0 \\ 0 & 0 & n_t \end{bmatrix} \begin{bmatrix} V_{tab} \\ V_{tbc} \\ V_{tca} \end{bmatrix} \tag{3.117}$$

where the turns ratio, n_t, is defined for the step-down connection as:

$$n_t = \frac{VLL_{RatedHighSide}}{VLL_{RatedLowSide}} \tag{3.118}$$

The relationship between the ideal delta voltages on the load side and the line-to-line voltages and delta currents is given by:

$$\begin{bmatrix} V_{tab} \\ V_{tbc} \\ V_{tca} \end{bmatrix} = \begin{bmatrix} V_{ab} \\ V_{bc} \\ V_{ca} \end{bmatrix} + \begin{bmatrix} Z_{tab} & 0 & 0 \\ 0 & Z_{tbc} & 0 \\ 0 & 0 & Z_{tca} \end{bmatrix} \begin{bmatrix} I_{ba} \\ I_{cb} \\ I_{ac} \end{bmatrix} \tag{3.119}$$

Substituting Eq. 3.119 into Eq. 3.117 and solving for the load side line-to-line voltages yields the following expression:

$$\begin{bmatrix} V_{ab} \\ V_{bc} \\ V_{ca} \end{bmatrix} = \begin{bmatrix} n_t & 0 & 0 \\ 0 & n_t & 0 \\ 0 & 0 & n_t \end{bmatrix}^{-1} \begin{bmatrix} V_{AB} \\ V_{BC} \\ V_{CA} \end{bmatrix} - \begin{bmatrix} Z_{tab} & 0 & 0 \\ 0 & Z_{tbc} & 0 \\ 0 & 0 & Z_{tca} \end{bmatrix} \begin{bmatrix} I_{ba} \\ I_{cb} \\ I_{ac} \end{bmatrix} \tag{3.120}$$

Using Kirchoff's voltage and current laws and the fact that the turns ratios of each phase are equal, the following expression can be derived for the load side line currents:

$$\begin{bmatrix} I_a \\ I_b \\ 0 \end{bmatrix} = \begin{bmatrix} 1 & 0 & -1 \\ -1 & 1 & 0 \\ Z_{tab} & Z_{tbc} & Z_{tca} \end{bmatrix} \begin{bmatrix} I_{ba} \\ I_{cb} \\ I_{ca} \end{bmatrix} \tag{3.121}$$

Solving Eq. 3.121 for the load side delta currents:

$$\begin{bmatrix} I_{ba} \\ I_{cb} \\ I_{ac} \end{bmatrix} = \frac{1}{Z_{tab} + Z_{tbc} + Z_{tca}} \begin{bmatrix} Z_{tca} & -Z_{tbc} & 1 \\ Z_{tca} & Z_{tab} + Z_{tca} & 1 \\ -Z_{tab} - Z_{tbc} & -Z_{tbc} & 1 \end{bmatrix} \begin{bmatrix} I_a \\ I_b \\ 0 \end{bmatrix} \tag{3.122}$$

To include the phase c line current in Eq. 3.122, we set the last column of the 3 x 3 matrix in Eq. 3.122 to zeros:

$$\begin{bmatrix} I_{ba} \\ I_{cb} \\ I_{ac} \end{bmatrix} = \frac{1}{Z_{tab} + Z_{tbc} + Z_{tca}} \begin{bmatrix} Z_{tca} & -Z_{tbc} & 0 \\ Z_{tca} & Z_{tab} + Z_{tca} & 0 \\ -Z_{tab} - Z_{tbc} & -Z_{tbc} & 0 \end{bmatrix} \begin{bmatrix} I_a \\ I_b \\ I_c \end{bmatrix} \tag{3.123}$$

Substituting Eq. 3.123 into Eq. 3.120 and solving for the source side line-to-line voltages yields the following expression:

$$\begin{bmatrix} V_{AB} \\ V_{BC} \\ V_{CA} \end{bmatrix} = \begin{bmatrix} n_t & 0 & 0 \\ 0 & n_t & 0 \\ 0 & 0 & n_t \end{bmatrix} \begin{bmatrix} V_{ab} \\ V_{bc} \\ V_{ca} \end{bmatrix} + \begin{bmatrix} n_t & 0 & 0 \\ 0 & n_t & 0 \\ 0 & 0 & n_t \end{bmatrix} \begin{bmatrix} Z_{tab} & 0 & 0 \\ 0 & Z_{tbc} & 0 \\ 0 & 0 & Z_{tca} \end{bmatrix} \begin{bmatrix} G \end{bmatrix} \begin{bmatrix} I_a \\ I_b \\ I_c \end{bmatrix} \tag{3.124}$$

where,

$$\begin{bmatrix} G \end{bmatrix} = \frac{1}{Z_{tab} + Z_{tbc} + Z_{tca}} \begin{bmatrix} Z_{tca} & -Z_{tbc} & 0 \\ Z_{tca} & Z_{tab} + Z_{tca} & 0 \\ -Z_{tab} - Z_{tbc} & -Z_{tbc} & 0 \end{bmatrix} \tag{3.125}$$

Because the power flow algorithm is written in terms of line-to-neutral or equivalent line-to-neutral voltages, an expression in terms of equivalent line-to-neutral voltages is required. Employing the theory of symmetrical components the relation between the source side equivalent line-to-neutral voltages and source side line-to-line voltages can be written:

$$\begin{bmatrix} V_{AN} \\ V_{BN} \\ V_{CN} \end{bmatrix} = \begin{bmatrix} W \end{bmatrix} \begin{bmatrix} V_{ab} \\ V_{bc} \\ V_{ca} \end{bmatrix} \tag{3.126}$$

where,

$$\left[W\right] = \frac{1}{3}\begin{bmatrix} 2 & 1 & 0 \\ 0 & 2 & 1 \\ 1 & 0 & 2 \end{bmatrix} \tag{3.127}$$

Substituting Eq. 3.126 into Eq. 3.124, using Kirchoff's voltage law to define the matrix $[D]$, and solving for the source side equivalent line-to-neutral voltages yields the following expression:

$$\begin{bmatrix} V_{AN} \\ V_{BN} \\ V_{CN} \end{bmatrix} = \left[W\right]\left[N_t\right]\left[D\right]\begin{bmatrix} V_{an} \\ V_{bn} \\ V_{cn} \end{bmatrix} + \left[W\right]\left[N_t\right]\left[Z_{tabc}\right]\left[G\right]\begin{bmatrix} I_a \\ I_b \\ I_c \end{bmatrix} \tag{3.128}$$

where,

$$\left[D\right] = \begin{bmatrix} 1 & -1 & 0 \\ 0 & 1 & -1 \\ -1 & 0 & 1 \end{bmatrix} \tag{3.129}$$

$$\left[Z_{tabc}\right] = \begin{bmatrix} Z_{tab} & 0 & 0 \\ 0 & Z_{tbc} & 0 \\ 0 & 0 & Z_{tca} \end{bmatrix} \tag{3.130}$$

$$\left[N_t\right] = \begin{bmatrix} n_t & 0 & 0 \\ 0 & n_t & 0 \\ 0 & 0 & n_t \end{bmatrix} \tag{3.131}$$

Eq. 3.128 is of the form of Eq. 3.83. Therefore, the generalized transformer matrices of Eq. 3.83 can be expressed as:

$$[a_t] = \left[W\right]\left[N_t\right]\left[D\right] = \frac{n_t}{3}\begin{bmatrix} 2 & -1 & -1 \\ -1 & 2 & -1 \\ -1 & -1 & 2 \end{bmatrix} \tag{3.132}$$

$$[b_t] = \left[W\right]\left[N_t\right]\left[Z_{tabc}\right]\left[G\right] \tag{3.133}$$

Noting the transformer polarity, the delta currents on the primary and secondary sides of the transformer are related by:

$$\begin{bmatrix} I_{ba} \\ I_{cb} \\ I_{ca} \end{bmatrix} = \begin{bmatrix} n_t & 0 & 0 \\ 0 & n_t & 0 \\ 0 & 0 & n_t \end{bmatrix}\begin{bmatrix} I_{AB} \\ I_{BC} \\ I_{CA} \end{bmatrix} \tag{3.134}$$

Solving Eq. 3.134 for the source side delta currents:

$$\begin{bmatrix} I_{AB} \\ I_{BC} \\ I_{CA} \end{bmatrix} = \begin{bmatrix} n_t & 0 & 0 \\ 0 & n_t & 0 \\ 0 & 0 & n_t \end{bmatrix}^{-1}\begin{bmatrix} I_{ba} \\ I_{cb} \\ I_{ca} \end{bmatrix} \tag{3.135}$$

And solving for the source side line currents as a function of the source side delta currents using Kirchoff's current law:

$$\begin{bmatrix} I_A \\ I_B \\ I_C \end{bmatrix} = \begin{bmatrix} 1 & 0 & -1 \\ -1 & 1 & 0 \\ 0 & -1 & 1 \end{bmatrix}\begin{bmatrix} I_{AB} \\ I_{BC} \\ I_{CA} \end{bmatrix} \tag{3.136}$$

Substituting Eq. 3.135 into Eq. 3.136:

$$\begin{bmatrix} I_A \\ I_B \\ I_C \end{bmatrix} = \begin{bmatrix} 1 & 0 & -1 \\ -1 & 1 & 0 \\ 0 & -1 & 1 \end{bmatrix} \begin{bmatrix} n_t & 0 & 0 \\ 0 & n_t & 0 \\ 0 & 0 & n_t \end{bmatrix}^{-1} \begin{bmatrix} I_{ba} \\ I_{cb} \\ I_{ca} \end{bmatrix} \tag{3.137}$$

The load side line currents can also be written as functions of the load side delta currents:

$$\begin{bmatrix} I_a \\ I_b \\ I_c \end{bmatrix} = \begin{bmatrix} 1 & 0 & -1 \\ -1 & 1 & 0 \\ 0 & -1 & 1 \end{bmatrix} \begin{bmatrix} I_{ba} \\ I_{cb} \\ I_{ca} \end{bmatrix} \tag{3.138}$$

Substituting Eq. 3.138 into Eq. 3.137 and noting that the matrix of n_t terms in Eq. 3.137 is a diagonal matrix, the source side line currents can be written:

$$\begin{bmatrix} I_A \\ I_B \\ I_c \end{bmatrix} = \begin{bmatrix} n_t & 0 & 0 \\ 0 & n_t & 0 \\ 0 & 0 & n_t \end{bmatrix}^{-1} \begin{bmatrix} I_a \\ I_b \\ I_c \end{bmatrix} \tag{3.139}$$

Eq. 3.139 is of the form of Eq. 3.84, therefore, for the generalized transformer matrices of Eq. 3.84, we can write:

$$[c_t] = \begin{bmatrix} 0 & 0 & 0 \\ 0 & 0 & 0 \\ 0 & 0 & 0 \end{bmatrix} \tag{3.140}$$

$$[d_t] = \begin{bmatrix} \frac{1}{n_t} & 0 & 0 \\ 0 & \frac{1}{n_t} & 0 \\ 0 & 0 & \frac{1}{n_t} \end{bmatrix} \tag{3.141}$$

Modifying Eq. 3.120 with the same logic that was applied to Eq. 3.128 yields the following expression which is of the form of Eq. 3.85:

$$\begin{bmatrix} V_{an} \\ V_{bn} \\ V_{cn} \end{bmatrix} = \Big[W\Big] \Big[N_t\Big]^{-1} \Big[D\Big] \begin{bmatrix} V_{AN} \\ V_{BN} \\ V_{CN} \end{bmatrix} - \Big[W\Big] \Big[Z_{tabc}\Big] \Big[G\Big] \begin{bmatrix} I_a \\ I_b \\ I_c \end{bmatrix} \tag{3.142}$$

Therefore, for the generalized matrices of Eq. 3.85, we can write:

$$[A_t] = \Big[W\Big] \Big[N_t\Big]^{-1} \Big[D\Big] = \frac{1}{3 \cdot n_t} \begin{bmatrix} 2 & -1 & -1 \\ -1 & 2 & -1 \\ -1 & 2 & -1 \end{bmatrix} \tag{3.143}$$

$$[B_t] = \Big[W\Big] \Big[Z_{tabc}\Big] \Big[G\Big] \tag{3.144}$$

3.6 Type B Step-Voltage Regulator Model

A single-phase step-voltage regulator consists of an autotransformer and a load tap changing mechanism [27]. The voltage regulation occurs as the device changes taps of the series winding of the autotransformer to achieve the desired regulation. A control

circuit known as a line drop compensator enables the automation of this process. The more common type B step regulator connection will be discussed in this section. Three single-phase type B regulators are connected in wye to form a wye-connected three-phase unit.

The following voltage and current equations can be written relating the line and load sides of the three-phase type B regulator, which are of the form of generalized series component Eqs. 3.1-3.2:

$$\begin{bmatrix} V_{AN} \\ V_{BN} \\ V_{CN} \end{bmatrix} = \begin{bmatrix} a_{Ra} & 0 & 0 \\ 0 & a_{Rb} & 0 \\ 0 & 0 & a_{Rc} \end{bmatrix} \begin{bmatrix} V_{an} \\ V_{bn} \\ V_{cn} \end{bmatrix} \tag{3.145}$$

$$\begin{bmatrix} I_A \\ I_B \\ I_C \end{bmatrix} = \begin{bmatrix} \frac{1}{a_{Ra}} & 0 & 0 \\ 0 & \frac{1}{a_{Rb}} & 0 \\ 0 & 0 & \frac{1}{a_{Rc}} \end{bmatrix} \begin{bmatrix} I_a \\ I_b \\ I_c \end{bmatrix} \tag{3.146}$$

Therefore, the general series component matrices of Eqs. 3.1-3.2 can be written as:

$$[a] = \begin{bmatrix} a_{Ra} & 0 & 0 \\ 0 & a_{Rb} & 0 \\ 0 & 0 & a_{Rc} \end{bmatrix} \quad [c] = \begin{bmatrix} 0 & 0 & 0 \\ 0 & 0 & 0 \\ 0 & 0 & 0 \end{bmatrix}$$

$$[b] = \begin{bmatrix} 0 & 0 & 0 \\ 0 & 0 & 0 \\ 0 & 0 & 0 \end{bmatrix} \quad [d] = \begin{bmatrix} \frac{1}{a_{Ra}} & 0 & 0 \\ 0 & \frac{1}{a_{Rb}} & 0 \\ 0 & 0 & \frac{1}{a_{Rc}} \end{bmatrix} \tag{3.147}$$

The effective regulator ratio, a_R, is given by:

$$a_R = 1 \pm 0.00625 \cdot Tap \tag{3.148}$$

where *Tap* denotes the tap setting. For a three-phase regulator, each phase can be monitored independently and the tap setting can be different for each phase. It is also possible in a "ganged" arrangement for a single phase to be monitored, and all tap settings will then be equivalent. The minus sign in Eq. 3.148 applies for the raise position, and the plus sign for the lower position. It should be noted that this model is lossless and modifies only the magnitudes of voltage and current.

The general series component matrices of Eq. 3.3 can then be written:

$$[A] = \left[a\right]^{-1} \tag{3.149}$$

$$[B] = \left[b\right]^{-1} \tag{3.150}$$

The tap setting is derived from the compensator settings, CT (current transformer) and PT (potential transformer) ratings, and regulator set points. The compensator settings are calibrated in volts and represent the equivalent impedance from the regulator to the load center. The load center may exist some distance downstream from the regulator, and the compensator circuit becomes a simulated model of the system that is used to determine the appropriate tap settings to properly regulate the voltage within the required tolerance.

In integrating the regulator model into the power flow algorithm, the power flow is first performed considering the regulator(s) as a lossless line section, essentially taking the value of *Tap* to be zero. The converged power flow solution is then used to determine the input voltage and current to the compensator circuit. A visual

representation of the compensator circuit can be viewed in Fig. 3.14.

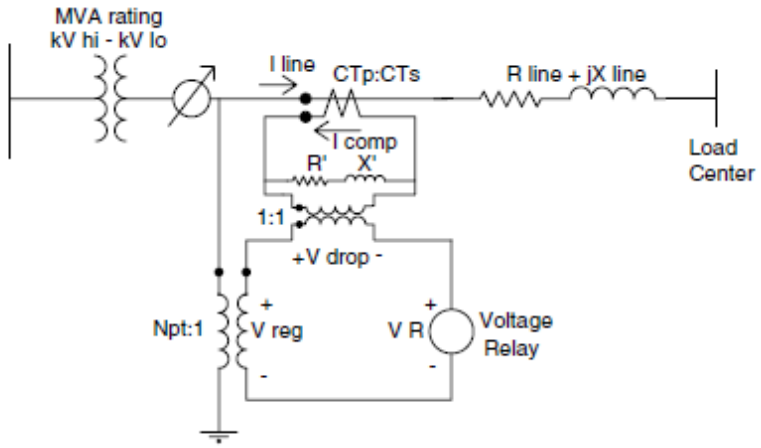

Figure 3.14: Regulator compensator circuit [27]

The parameters needed for the calculation of the tap settings are as follows:

R' = compensator R setting (volts)

X' = compensator X setting (volts)

CT_p = CT primary rating (amps); typically rated current of feeder

CT_s = CT secondary rating (amps)

N_{pt} = PT ratio (nominal LN voltage divided by 120 V)

V_{level} = voltage set point scaled to 120 V base

BW = bandwidth; the allowed variance of the load center voltage from V_{level}

V_{input} = input voltage to the PT; LN voltage present at the regulator after initial power flow solution (volts)

I_{input} = input current to the CT; line current through the regulator after intitial power flow solution (amps)

I_{input} and V_{input} are the complex phase currents and voltages, where for single- or

two-phase circuits, some values may be zero. The compensator settings R' and X' are provided in volts and must be converted to Ohms as:

$$R + jX = \frac{R' + jX'}{CT_s}\ \Omega \tag{3.151}$$

where j is the unit imaginary number.

The compensator current is derived from I_{input} as:

$$I_{comp} = \frac{I_{input} \cdot CT_s}{CT_p}\ A \tag{3.152}$$

The input voltage to the compensator circuit is:

$$V_{reg} = \frac{V_{input}}{N_{pt}}\ V \tag{3.153}$$

The voltage drop in the compensator circuit is equal to the compensator current times the compensator settings in Ohms, Eq. 3.151:

$$V_{drop} = (R + jX) \cdot I_{comp} \tag{3.154}$$

The voltage across the voltage relay represents the voltage at the load center that is to be regulated. This voltage, with reference to Fig. 3.14 is given by:

$$V_{relay} = V_{reg} - V_{drop} \tag{3.155}$$

And the tap settings are subsequently determined from V_{relay}, the voltage level set point, and the bandwidth as:

$$Tap = round\left(\frac{(V_{level} - 0.5 \cdot BW) - |V_{relay}|}{0.75}\right) \tag{3.156}$$

The notation *round* indicates the result is to be rounded to the nearest integer, as the tap settings are only defined for integer values. Standard step regulators contain a reversing switch enabling a $\pm$ 10% regulator range in 32 steps. This amounts to a 0.75 V change with each step on a 120 V base, hence the denominator of Eq. 3.156. The result of Eq. 3.156 will be three tap settings, where values may not apply for single- or two-phase circuits, and depending on how the power flow program is written. The final generalized matrices for integrating the regulator into the power flow algorithm will be determined from substituting Eq. 3.156 into Eq. 3.148, and subsequently Eqs. 3.147 and 3.149.

3.7 Capacitor Banks

Shunt capacitor banks are modeled as constant susceptances and can be connected in delta or wye. The input to the power flow is known nominal kvar and voltage, either line-to-neutral for wye connected banks, or line-to-line for delta connected banks. In the equations in this section, the units of capacitor reactive power rating are vars and voltage is in volts. In application of the power flow algorithm, the contributions to the line current from a capacitor bank are treated as additional load current, and must be added to any other load currents present at a node due to a lumped or distributed load.

3.7.1 Wye Connection

For wye-connected banks, the notation for nominal reactive power rating of each phase unit and nominal line-to-neutral voltages is as follows:

$$\begin{aligned} &\text{Phase a} : Q_a^{rated} \text{ and } V_{an} \\ &\text{Phase b} : Q_b^{rated} \text{ and } V_{bn} \\ &\text{Phase c} : Q_c^{rated} \text{ and } V_{cn} \end{aligned} \tag{3.157}$$

The notation for calculated line-to-neutral voltages is as follows:

$$\begin{aligned} &\text{Phase a} : |\hat{V}_{an}|\angle\hat{\delta}_a \\ &\text{Phase b} : |\hat{V}_{bn}|\angle\hat{\delta}_b \\ &\text{Phase c} : |\hat{V}_{cn}|\angle\hat{\delta}_c \end{aligned} \tag{3.158}$$

The constant susceptance for each phase, in Siemens, is calculated as:

$$\begin{aligned} B_a &= \frac{Q_a^{rated}}{|V_{an}|^2} \\ B_b &= \frac{Q_b^{rated}}{|V_{bn}|^2} \\ B_c &= \frac{Q_c^{rated}}{|V_{cn}|^2} \end{aligned} \tag{3.159}$$

This susceptance will stay constant during the power flow, while the reactive power contribution of the capacitor bank will vary with the calculated voltage. The contribution to the line current from the capacitor bank will also change iteratively during the power flow based on the calculated voltage as:

$$
\begin{aligned}
I_a^L &= jB_a\hat{V}_{an} \\
I_b^L &= jB_b\hat{V}_{bn} \\
I_c^L &= jB_c\hat{V}_{cn}
\end{aligned}
\tag{3.160}
$$

3.7.2 Delta Connection

For delta-connected banks, the notation for nominal reactive power rating of each phase unit and nominal line-to-line voltages is as follows:

$$
\begin{aligned}
&\text{Phase ab} : Q_{ab}^{rated} \text{ and } V_{ab} \\
&\text{Phase bc} : Q_{bc}^{rated} \text{ and } V_{bc} \\
&\text{Phase ca} : Q_{ca}^{rated} \text{ and } V_{ca}
\end{aligned}
\tag{3.161}
$$

The notation for calculated line-to-line voltages is as follows:

$$
\begin{aligned}
&\text{Phase ab} : |\hat{V}_{ab}|\angle\hat{\delta}_{ab} \\
&\text{Phase bc} : |\hat{V}_{bc}|\angle\hat{\delta}_{bc} \\
&\text{Phase ca} : |\hat{V}_{ca}|\angle\hat{\delta}_{ca}
\end{aligned}
\tag{3.162}
$$

The constant susceptance for each phase, in Siemens, is calculated as:

$$
\begin{aligned}
B_{ab} &= \frac{Q_{ab}^{rated}}{|V_{ab}|^2} \\
B_{bc} &= \frac{Q_{bc}^{rated}}{|V_{bc}|^2} \\
B_{ca} &= \frac{Q_{ca}^{rated}}{|V_{ca}|^2}
\end{aligned}
\tag{3.163}
$$

This susceptance will stay constant during the power flow, while the reactive power contribution of the capacitor bank will vary with the calculated voltage. The contribution to the delta load current in each phase of the capacitor bank will also change iteratively during the power flow based on the calculated voltage as:

$$
\begin{aligned}
I_{ab}^{L} &= jB_{ab}\hat{V}_{ab} \\
I_{bc}^{L} &= jB_{bc}\hat{V}_{bc} \\
I_{ca}^{L} &= jB_{ca}\hat{V}_{ca}
\end{aligned}
\tag{3.164}
$$

As in the delta-connected lumped load models, the recovery of the contribution to the line currents from the delta load currents is accomplished by application of Kirchoff's current law at the nodes of the delta, as:

$$
\begin{bmatrix} I_a^L \\ I_b^L \\ I_c^L \end{bmatrix} = \begin{bmatrix} 1 & 0 & -1 \\ -1 & 1 & 0 \\ 0 & -1 & 1 \end{bmatrix} \begin{bmatrix} I_{ab}^L \\ I_{bc}^L \\ I_{ca}^L \end{bmatrix}
\tag{3.165}
$$

CHAPTER 4: ELECTROTHERMAL COUPLING IN DISTRIBUTION SYSTEM LINE SECTIONS

4.1 Overview

This chapter will provide the means of relating the line conductor temperature (thermal) with the line current and line impedance (electrical), presenting an electrothermal coupling between these parameters that will be implemented into the power flow algorithm of Chapter 5. The resistance of an electrical conductor is known to be approximately linearly related to temperature, i.e., as the conductor temperature increases, so to does the conductor resistance. It is also well known that the conductor impedance, of which the resistance is a component, will affect conductor current, which in turn affects the conductor temperature. This recursive relationship is presented for bare overhead conductors by the IEEE Std. 738 [7] and by the IEC Std. 60287 [30] for electric cables, which can be underground or exposed to air.

The relationships presented in [7] and summarized in section 4.2.1 can be used to solve for the line current of a bare overhead conductor, given conductor temperature, certain ambient parameters such as weather conditions, and the conductor characteristics. For the purposes of this work, however, the formulations will be used to solve for conductor temperature given line current, ambient conditions, and conductor characteristics. This relationship is non-linear and is solved iteratively with an efficient bisection algorithm [58] presented in section 4.2.2.

For underground cable electrothermal coupling, the formulations of [30] will be used to relate the line current of the cable, the ambient conditions (burial method and medium, soil temperature), and the cable characteristics with the conductor temperature and the conductor impedance. The formulations allow for the calculation

of the temperature rise above ambient, and can be solved iteratively for a variety of cable configurations and types. For this work, the electrothermal coupling is presented only for the types of cable and configurations required to solve the case studies in Chapter 6, concentric neutral cable (section 4.3.1) and tape-shielded cable (section 4.3.2).

4.2 Bare Overhead Conductors

4.2.1 Steady-State Heat Balance Equation and IEEE Std. 738

The steady-state heat balance equation (SSHBE) of [7] assumes that the weather conditions, current, and conductor temperature are in steady state, or are constant for all time, denoting that the heat loss and the heat gain are equivalent. In this section an effort has been made to keep the variable and parameter symbology consistent with IEEE Std. 738. The SSHBE has the following form:

$$Q_C(T_C) + Q_R(T_C) = Q_S + I^2 R(T_C) \tag{4.1}$$

where,

T_C = conductor temperature ($^\circ C$)

Q_C = convective heat loss rate per unit length (W/m); a function of T_C

Q_R = radiated heat loss rate per unit length (W/m); a function of T_C

Q_S = solar heat gain rate per unit length (W/m)

R = AC resistance per unit length (Ω/m); a function of T_C

I = conductor current (A)

Terms Q_C, Q_R, and R in Eq. 4.1 are functions of conductor temperature, while

Q_S is not, and is dependent itself on the time of day, the location of the line, and other factors that will be detailed in this section. Eq. 4.1 can be rewritten to solve for current as:

$$I = \sqrt{\frac{Q_C(T_C) + Q_R(T_C) - Q_S}{R(T_C)}} \tag{4.2}$$

It is this form of the SSHBE that will be used in the algorithm discussed in section 4.2.2, along with the Q term formulations and the calculation of $R(T_C)$. The convective heat loss term for forced convection at low wind speeds is:

$$q_{c1} = K_{angle} \cdot [1.01 + 1.35 \cdot N_{Re}^{0.52}] \cdot k_f \cdot (T_C - T_a) \text{ (W/m)} \tag{4.3}$$

And at high winds speeds is:

$$q_{c2} = K_{angle} \cdot 0.754 \cdot N_{Re}^{0.6} \cdot k_f \cdot (T_C - T_a) \text{ (W/m)} \tag{4.4}$$

where,

K_{angle} = wind direction factor

N_{Re} = Reynolds number

k_f = thermal conductivity of air at temperature T_{film} (W/(m-$^\circ C$))

T_a = ambient temperature ($^\circ C$)

The formulations for K_{angle}, N_{Re}, and k_f can be found in [7]. The natural convec-

tion, in the case of zero wind speed, is found by:

$$q_{cn} = 3.645 \cdot \rho_f \cdot D_0^{0.75} \cdot (T_C - T_a)^{1.25} \text{ (W/m)} \tag{4.5}$$

where,

$D_0 =$ outside diameter of conductor (m)

$\rho_f =$ density of air (kg/m^3)

The formulation for ρ_f can be found in [7]. As suggested by [7], the convective heat loss term Q_C is conservatively taken as the maximum of these three heat loss formulations:

$$Q_C = \max\{q_{c1}, q_{c2}, q_{cn}\} \text{ (W/m)} \tag{4.6}$$

The radiated heat loss term, Q_R, can be written as:

$$Q_R = 17.8 \cdot D_0 \cdot \varepsilon \cdot \left[\left(\frac{T_C + 273}{100} \right)^4 - \left(\frac{T_a + 273}{100} \right)^4 \right] \text{ (W/m)} \tag{4.7}$$

where,

$\varepsilon =$ conductor emissivity (0.23 to 0.91 dependent on age and other factors)

The solar heat gain term, Q_S, can be written as:

$$Q_S = \alpha \cdot Q_{se} \cdot sin(\theta) \cdot A^{'} \text{ (W/m)} \tag{4.8}$$

where,

$\alpha =$ solar absorptivity (0.23 to 0.91 dependent on age and other factors)

$Q_{se} =$ total solar and sky radiated heat intensity corrected for elevation (W/m^2)

$\theta =$ angle that is a function of the altitude and azimuth of the sun,
and the azimuth of the line

$A^{'} =$ projected area of the conductor (m^2/linear m)

The formulations for Q_{se} and θ can be found in [7]. The solar heating is naturally dependent on the time of day and year during which the calculation is considered.

The resistance per unit length of a bare overhead stranded conductor is approximated as being linear, or piece-wise linear, and utilizes tabulated values of resistance at various temperatures as presented in resources such as [31], which are assumed to account for skin effect. The resistance can therefore be derived by linear interpolation as:

$$R(T_C) = \left[\frac{R(T_{high}) - R(T_{low})}{T_{high} - T_{low}}\right] \cdot (T_C - T_{low}) + R(T_{low}) \tag{4.9}$$

where,

$$T_{high} = 75°C \text{ if } T_C > 50°C,\ 50°C \text{ otherwise}$$

$$T_{low} = 50°C \text{ if } T_C > 50°C,\ 25°C \text{ otherwise}$$

$$R(T_{high}) = \text{tabulated resistance at } T_{high}$$

$$R(T_{low}) = \text{tabulated resistance at } T_{low}$$

The relationship dictated by 4.1 is non-linear and does not have a closed form solution. A bisection algorithm, a method of solving non-linear equations, is presented in the following section, utilizing the equations presented in this section and referenced in [7].

4.2.2 Solution to Steady-State Heat Balance Equation with Bisection Algorithm

The calculations necessary to arrive at the conductor temperature and corresponding resistance, presented in the previous section, will need to be computationally fast, as the subroutine will be called many times during simulation for even a small system. Therefore, a bisection algorithm will be used to efficiently calculate the non-linear relationship between conductor temperature and current indicated by IEEE Std. 738 for bare overhead conductors.

A bisection algorithm, also known as a binary search method or interval halving method, divides a search area interval that contains the solution to a non-linear equation into two halves. The solution to the equation is found using the midpoint value of this range, the solution is tested for convergence criteria, and if unsatisfactory, is adjusted based on the magnitude of the solution with respect to a reference value.

In the case of the SSHBE, the reference value is the line current input from the power flow algorithm. If the calculated current from Eq. 4.2 is less than the reference current, the positive correlation between current and conductor temperature indicates that the conductor temperature must be higher than that initially assumed. Con-

versely, if the calculated current is greater than the reference current, the conductor temperature must be lower. Using this knowledge, the search area interval is redefined and once again bisected. This process continues until convergence is reached. A summary of this technique as applied to the SSHBE can be viewed in Fig. 4.1.

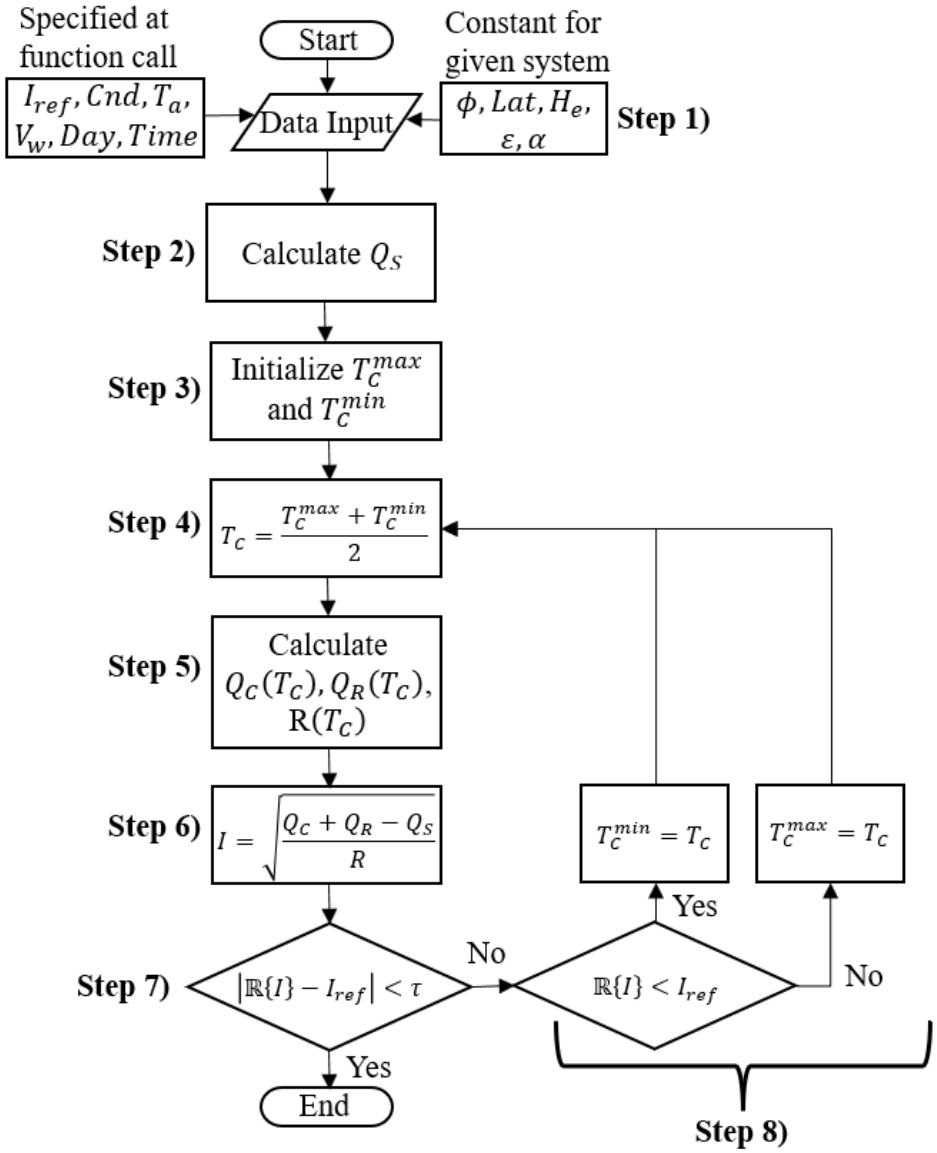

Figure 4.1: Bisection algorithm for reformulated SSHBE (Eq. 4.2)

With reference to Fig. 4.1, the bisection algorithm is as follows:

Step 1) Input data, where:

I_{ref} = reference current (A)

Cnd = MATLAB struct that contains conductor data such as diameter and resistance at $25°C$, $50°C$, and $75°C$

T_a = ambient temperature ($°C$)

Day = day of the year

$Time$ = time of day (military)

ϕ = wind angle; angle between wind direction and conductor axis

Lat = latitude of system

H_e = elevation of system

ε = emissivity

α = solar absorptivity

Step 2) Calculate solar heat gain parameter Q_S using Eq. 4.8.

Step 3) Initialize upper (T_C^{max}) and lower (T_C^{min}) limits of conductor temperature for the first search range.

Step 4) Initialize conductor temperature as the midpoint of initial search range.

Step 5) Calculate heat loss parameters Q_C and Q_R, and resistance at conductor temperature using Eqs. 4.6, 4.7, and 4.9.

Step 6) Solve for the current that corresponds to conductor temperature and input data using Eq. 4.2.

Step 7) If the difference between the current in Step 6 and I_{ref} is within convergence tolerance τ, end the algorithm and output the conductor temperature.

Step 8) Otherwise, if the current in Step 6 is less than I_{ref}, the conductor temperature must be higher, so modify search range to be the upper half of the previous search range. Similarly, if the Step 6 current is greater than I_{ref}, the conductor temperature must be lower, so modify search range to be the lower half of the previous search range. Continue with Step 4.

4.3 Underground Cable

The IEC Std. 60287 [30] is composed of two parts, the first being current rating equations and calculation of losses for electric cables, which can be buried or exposed to air, and the second concerning the calculation of thermal resistance. Thermal resistance is a concept analogous to electrical resistance whereby materials have an inherent property that inhibits the transfer of heat. Using the formulations for thermal resistance presented in Part 2-1 of the standard, and the general equations relating temperature rise above ambient to current, ambient conditions, and cable characteristics in Part 1-1, this section will provide the necessary electrothermal coupling for underground cable to implement the temperature-dependent power flow (Chapter 5) used in the specific case studies in Chapter 6. The following formulations are specific to the cable configurations and spacing present in the underground sections of the case study systems, and also assume the cables to be direct buried in earth in locations where drying out of the soil does not occur, which is not specified in the test system data. This assumption could be easily changed to reflect different conditions by referencing [30]. In the sections that follow, every effort has been made to keep the variable and parameter symbology consistent with [30].

4.3.1 Concentric Neutral Cable Thermal Modeling with IEC 60287

The equation for the temperature rise above ambient for buried AC cables where drying out of the soil does not occur is given as:

$$\Delta\theta = (I^2R + 0.5 \cdot W_d) \cdot T_1 + [I^2R(1 + \lambda_1) + W_d] \cdot n \cdot T_2 + \quad (4.10)$$
$$[I^2R(1 + \lambda_1 + \lambda_2) + W_d] \cdot (T_3 + T_4) \quad [^\circ K] \text{ or } [^\circ C]$$

where,

θ = ambient temperature of surrounding medium

I = current in the conductor (A)

R = AC resistance per unit length at the conductor temperature

W_d = dielectric loss per unit length for the insulation around the conductor (W/m)

T_1 = thermal resistance per unit length between the conductor and sheath (K-m/W)

T_2 = thermal resistance per unit length of bedding between sheath and armour (K-m/W)

T_3 = thermal resistance per unit length of external serving of cable (K-m/W)

T_4 = thermal resistance per unit length between the cable surface and surrounding medium (K-m/W)

λ_1 = ratio of losses in the metal sheath to total losses in all conductors in the cable

λ_2 = ratio of losses in the armouring to total losses in all conductors in the cable

n = number of load-carrying conductors in the cable (of equal size and load)

The underground concentric neutral cable sections of the IEEE 13-node test feeder (section 6.4) and the 123-node test feeder (section 6.5) both have specific cable spacing that can be viewed in Fig. 4.2 [29]. The cable spacing will be used in the calculation

of some parameters in Eq. 4.10.

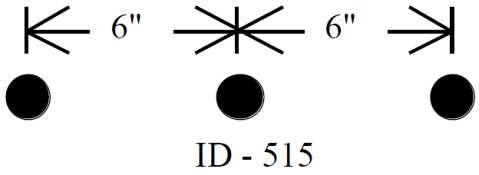

Figure 4.2: Concentric neutral cable spacing [29]

The line current I is an input from the power flow algorithm, and the resistance R is calculated as in Eq. 4.9. The dielectric loss, W_d, is considered to be negligible and equal to zero for the voltages considered for the test case systems [30].

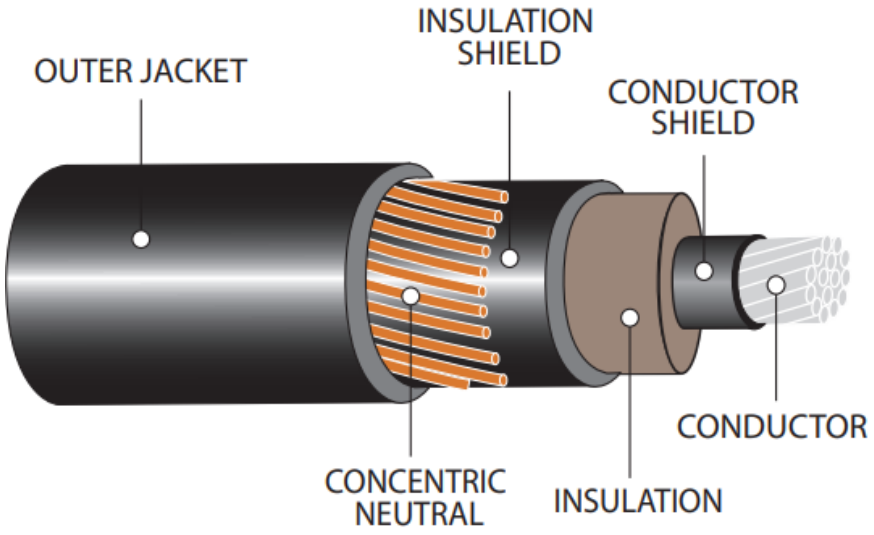

Figure 4.3: Concentric neutral cable layers [59]

With reference to Fig. 4.3, the thermal resistance between a single conductor and sheath (insulation shield) for a single core cable is given by:

$$T_1 = \frac{\rho_T}{2\pi} \ln\left[1 + \frac{2t_1}{d_c}\right] \tag{4.11}$$

where,

ρ_T = thermal resistivity of insulation (K-m/W)

d_c = diameter of conductor (mm)

t_1 = thickness of insulation between conductor and sheath

According to the standard, for unarmoured cables with extruded installation where each core has an individual screen of spaced wires, such as with the concentric neutral cables [30]:

$$T_2 = 0 \tag{4.12}$$

The thermal resistance of the outer covering (serving or jacket), T_3, for the general case is:

$$T_3 = \frac{\rho_T}{2\pi} \ln \left[1 + \frac{2t_3}{D_a^{'}} \right] \tag{4.13}$$

where,

ρ_T = thermal resistivity of jacket (K-m/W)

$D_a^{'}$ = external diameter of armour (mm)

t_3 = thickness of jacket (mm)

For unarmoured cables such as the concentric neutral cables that will be considered for the case studies [59], $D_a^{'}$ is taken as the external diameter of the sheath screen,

screen, or bedding beneath the jacket. A three phase cable configuration for a distribution system made up of three distinct cables, such as that shown in Fig. 4.2, may have unequal losses corresponding to unbalanced current across the three phase conductors. For this work, an approximation will be made in terms of the thermal modeling that the three cables have approximately equal losses. The result is a more conservative temperature rise above ambient conditions, perhaps an overestimation of the temperature rise, for the two cables that may have smaller current magnitudes. With this approximation, the thermal resistance between the surface of the cable and the surrounding medium, T_4, for three cables having approximately equal losses, laid in a horizontal plan and equally spaced apart, as in Fig. 4.2, is given by:

$$T_4 = \frac{\rho_T}{2\pi}\left\{\ln\left(u+\sqrt{u^2-1}\right)+\ln\left[1+\left(\frac{2L}{s_1}\right)^2\right]\right\} \tag{4.14}$$

where,

ρ_T = thermal resistivity of the soil (K-m/W)

$u = \dfrac{2L}{D_e}$

L = the distance from the surface of the ground to the cable axis (mm)

D_e = external diameter of one cable (mm)

s_1 = axial separation between two adjacent cables (mm)

The ratio of losses in the metal sheath (concentric neutral strands themselves) to total losses in all conductors in a single cable, λ_1, is given by:

$$\lambda_1 = \lambda_1^{'} + \lambda_1^{''} \tag{4.15}$$

where eddy-current loss, $\lambda_1^{''}$, is ignored for cables of this type (non-segmental, small conductors) [30].

Therefore, we can calculate λ_1 independently for each conductor in the formation of Fig. 4.2, without transposition of conductors, and assuming sheaths bonded at both ends of the electrical section, as:

$$\lambda_{11} = \lambda_{11}^{'} = \frac{R_s}{R}\left[\frac{0.75P^2}{R_s^2+P^2} + \frac{0.25Q^2}{R_s^2+Q^2} + \frac{2R_sPQX_m}{\sqrt{3}(R_s^2+P^2)(R_s^2+Q^2)}\right] \tag{4.16}$$

$$\lambda_{12} = \lambda_{11}^{'} = \frac{R_s}{R}\left[\frac{0.75P^2}{R_s^2+P^2} + \frac{0.25Q^2}{R_s^2+Q^2} - \frac{2R_sPQX_m}{\sqrt{3}(R_s^2+P^2)(R_s^2+Q^2)}\right] \tag{4.17}$$

$$\lambda_{1m} = \lambda_{1m}^{'} = \frac{R_s}{R}\frac{Q^2}{R_s^2+Q^2} \tag{4.18}$$

where,

$$P = X + X_m$$

$$Q = X - \frac{X_m}{3}$$

$X =$ the reactance of sheath or screen per unit length for two adjacent single-core cables

$= 2\omega \cdot 10^{-}7 \ln\left(\frac{2s}{d}\right)$ (Ω/m)

$X_m =$ the mutual reactance per unit length between sheath of outer cable and the other two conductors, in a flat formation

$= 2\omega \cdot 10^{-}7 \ln(2)$ (Ω/m)

And,

λ_{11} = losses caused by circulating currents in the outer conductor with highest loss

λ_{12} = losses caused by circulating currents in the other outer conductor

λ_{1m} = losses caused by circulating currents in the middle conductor

R = resistance of conductor per unit length

R_s = resistance of sheath or screen per unit length

s = distance between conductor axes (mm)

d = mean diameter of the sheath (mm)

$\omega = 2\pi \cdot f$

The ratio of losses in the armour to that of all conductors in the cable, λ_2, is taken to be zero for the unarmoured cable considered for the test cases [60]. The number of load-carrying conductors in a single cable, n, is equal to 1. Therefore, for the concentric neutral cable modeled in the case studies in Chapter 6:

$$\lambda_2 = 0; \quad n = 1 \tag{4.19}$$

Similarly to the solution to the SSHBE in section 4.2.2, Eq. 4.10 must be calculated iteratively due to the non-linear relationship between current, conductor temperature, and resistance. The equation has much faster convergence than the SSHBE, so a bisection algorithm was unnecessary in this case. A simple algorithm to iteratively solve for the rise above ambient temperature is described in section 4.3.3.

Once $\Delta\theta$ is known, the cable temperature is then:

$$\theta = T_a + \Delta\theta \ [^\circ C] \tag{4.20}$$

T_a = ambient temperature of soil (cable assumed direct buried) ($^\circ C$)

θ = conductor temperature ($^\circ C$)

4.3.2 Tape-Shielded Cable Thermal Modeling with IEC 60287

The tape-shielded cable section of the IEEE The 13-node test feeder (section 6.4) has specific cable spacing that can be viewed in Fig. 4.4 [29]. Equation 4.10 in the previous section still applies under the assumption that the cable is direct buried and partial drying out of the soil does not occur. The cable spacing will be used in the calculation of some parameters in Eq. 4.10. The line section in question is a single-phase line consisting of a phase conductor and a neutral conductor.

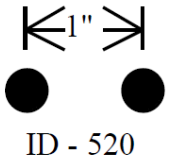

Figure 4.4: Tape-shielded cable spacing [29]

As in the concentric neutral cable case, the line current I is an input from the power flow algorithm, and the resistance R is calculated as in Eq. 4.9. The dielectric loss, W_d, is considered to be negligible and equal to zero for the voltages considered for the test case systems [30].

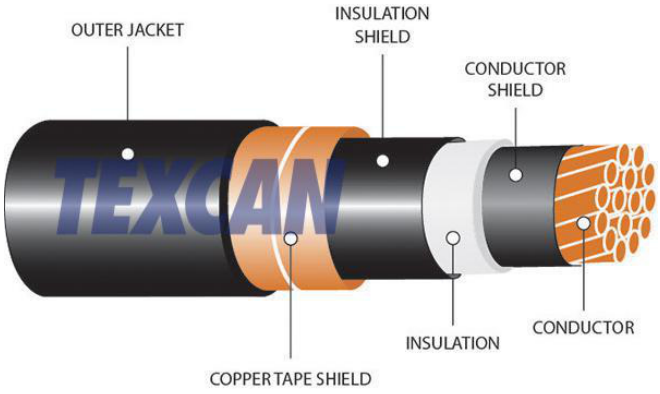

Figure 4.5: Tape-shielded cable layers [59]

With reference to Fig. 4.5, the thermal resistance between a single conductor and sheath (insulation shield) for a single core cable is given by:

$$T_1 = \frac{\rho_T}{2\pi} \ln\left[1 + \frac{2t_1}{d_c}\right] \tag{4.21}$$

where,

ρ_T = thermal resistivity of insulation (K-m/W)

d_c = diameter of conductor (mm)

t_1 = thickness of insulation between conductor and sheath

According to the standard, for unarmoured cables with extruded installation and a common metallic screen, such as with tape-shielded cables [30]:

$$T_2 = 0 \tag{4.22}$$

The thermal resistance of the outer covering (serving or jacket), T_3, for the general

case is:

$$T_3 = \frac{\rho_T}{2\pi} \ln \left[1 + \frac{2t_3}{D'_a} \right] \tag{4.23}$$

where,

ρ_T = thermal resistivity of jacket (K-m/W)

D'_a = external diameter of armour (mm)

t_3 = thickness of jacket (mm)

The thermal resistance between the surface of the cable and the surrounding medium, T_4, for two cables having approximately equal losses, laid in a horizontal plane and not touching, as in Fig. 4.4, is given by:

$$T_4 = \frac{\rho_T}{2\pi} \left\{ \ln \left(u + \sqrt{u^2 - 1} \right) + \frac{1}{2} \ln \left[1 + \left(\frac{2L}{s_1} \right)^2 \right] \right\} \tag{4.24}$$

where,

ρ_T = thermal resistivity of the soil (K-m/W)

$u = \dfrac{2L}{D_e}$

L = the distance from the surface of the ground to the cable axis (mm)

D_e = external diameter of one cable (mm)

s_1 = axial separation between two adjacent cables (mm)

The ratio of losses in the metal sheath (tape shield) to total losses in all conductors in a single cable, λ_1, is given by:

$$\lambda_1 = \lambda_1^{'} + \lambda_1^{''} \tag{4.25}$$

where eddy-current loss, $\lambda_1^{''}$, is ignored for cables of this type (non-segmental, small conductors) [30].

The calculation for λ_1 for two single-core cables as in Fig. 4.4, and assuming sheaths bonded at both ends of the electrical section, is:

$$\lambda_1 = \lambda_1^{'} = \frac{R_s}{R} \frac{1}{1 + \left(\frac{R_s}{X}\right)^2} \tag{4.26}$$

where,

X = the reactance of sheath or screen per unit length for two adjacent single-core cables

$= 2\omega \cdot 10^{-7} \ln\left(\frac{2s}{d}\right)$ (Ω/m)

λ_1 = losses caused by circulating currents in the conductor

R = resistance of conductor per unit length

R_s = resistance of sheath or screen per unit length

s = distance between conductor axes (mm)

d = mean diameter of the sheath (mm)

$\omega = 2\pi \cdot f$

The ratio of losses in the armour to that of all conductors in the cable, λ_2, is taken to be zero for the unarmoured cable considered for the test cases [61]. The number of load-carrying conductors in a single cable, n, is equal to 1. Therefore, for the tape-shielded cable modeled in the case studies in Chapter 6:

$$\lambda_2 = 0; \quad n = 1 \tag{4.27}$$

The following section will describe the iterative algorithm used to solve the equations in sections 4.3.1 and 4.3.2.

4.3.3 Iterative Algorithm to Solve IEC 60287 Equations

Similarly to the solution to the SSHBE in section 4.2.2, Eq. 4.10 must be calculated iteratively due to the non-linear relationship between current, conductor temperature, and resistance. The equation has much faster convergence than the SSHBE, so a bisection algorithm was unnecessary in this case. A simple algorithm to iteratively solve for the rise above ambient temperature is described in this section.

With reference to Fig. 4.6, the algorithm is as follows:

Step 1) Input data.

Step 2) Calculate conductor resistances for all cables at ambient temperature using Eq. 4.9.

Step 3) Calculate thermal parameters using equations in sections 4.3.1 or 4.3.2 as appropriate.

Step 4) Calculate temperature rise above ambient with Eq. 4.10.

Step 5) Calculate conductor temperatures.

Step 6) Find resistance values at this new temperature.

Step 7) If the difference between the last resistance values and current resistance values is within convergence tolerance τ, end the algorithm and output the conductor temperatures.

Step 8) Otherwise, use the currently calculated resistance value as input to Step 3. Continue with Step 3.

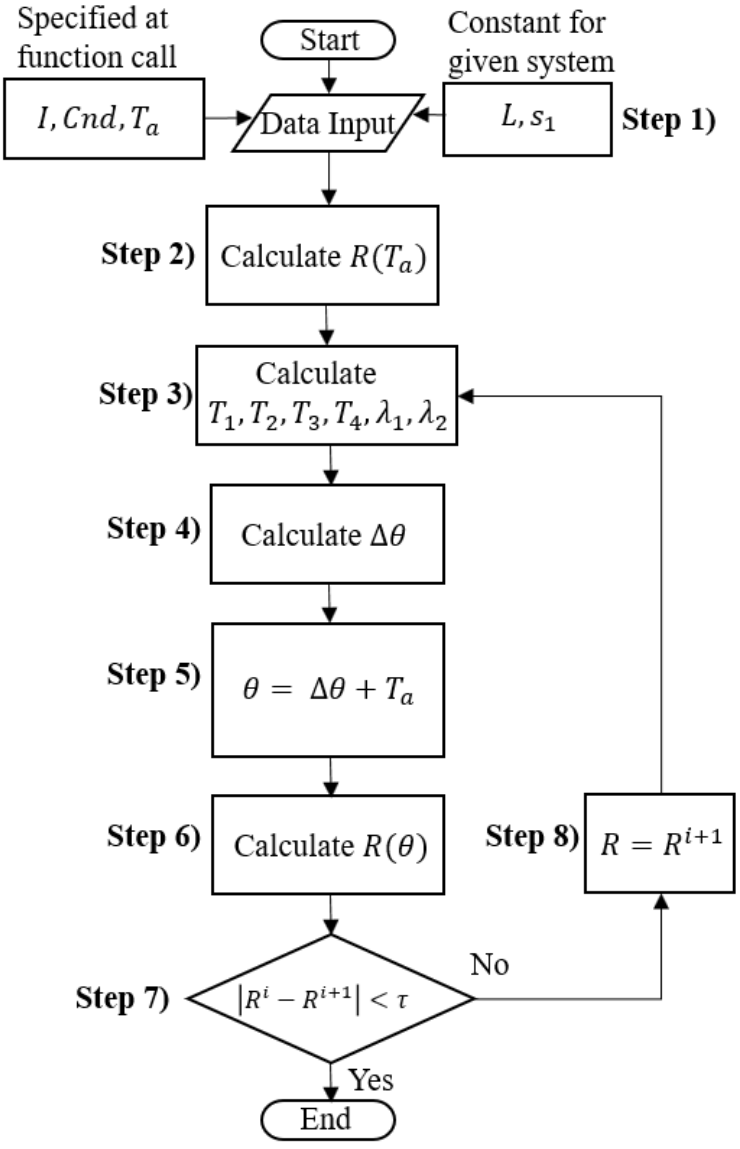

Figure 4.6: Iterative algorithm for calculation of underground cable conductor temperature (Eq. 4.10)

I = conductor line current (A)

Cnd = MATLAB struct that contains conductor data such as cable parameters and resistance at $25°C$, $50°C$, and $75°C$

T_a = soil ambient temperature ($°C$)

L = the distance from the surface of the ground to the cable axis (mm)

s_1 = axial separation between two adjacent cables (mm)

R = conductor resistance

θ = conductor temperature

In the next chapter, the component modeling of Chapter 3 will be integrated into a non-temperature-dependent (fixed conductor resistance) three-phase backward-forward sweep power flow algorithm for radial systems. The proposed *temperature-dependent* power flow algorithm will then be developed by modifying the non-temperature-dependent algorithm to include the electrothermal coupling of line sections presented in this chapter.

CHAPTER 5: BACKWARD-FORWARD SWEEP RADIAL POWER FLOW ALGORITHM

5.1 Overview

Backward-forward sweep power flow algorithms are generally based on either Kirchoff's circuit laws or a bi-quadratic expression relating node voltage and power, as detailed in section 2.3.2. This family of techniques employ a method of iteratively traversing a radial or weakly-meshed system from root (source) to end nodes to calculate the unknown node voltages and thereby determine the steady-state condition of the network. In this chapter, a backward-forward sweep algorithm based on the ladder iterative technique of [27] and the node/branch ordering scheme of [20] is presented, both as a conventional power flow algorithm (non-temperature-dependent) and as the proposed temperature-dependent power flow technique where the conductor temperatures are integrated into the power flow solution.

Section 5.2 will present the conventional algorithm, and subsections will describe the node/branch ordering scheme, the input data matrices, and the algorithm itself. Section 5.3 will then present the modifications to the conventional algorithm that introduce temperature-dependency to the power flow solution.

5.2 Conventional Backward-Forward Sweep Power Flow Algorithm

The conventional backward-forward sweep power flow algorithm described in this section is based on the ladder iterative technique detailed in [27] and employs the familiar current and voltage laws of Kirchoff, and utilizes the three-phase modeling of transformers, line sections, voltage regulators, loads, and capacitor banks as described in Chapter 3. This algorithm is designed for use with purely radial distribution

systems and cannot, in its current form, accommodate meshed systems containing loops.

By conventional power flow algorithm it is meant that the line conductor resistance is considered fixed at the value as given in the system data, or as assumed from knowledge of the conductor and as given in a resource such as [31]. By extension, the assumption is also that the conductor temperature remains fixed, regardless of considered weather conditions and conductor current, which is known to not be the case (see Chapter 4 and literature review in Chapter 2).

This differs from the temperature-dependent modification to the algorithm presented in section 5.3 where the conductor temperature is explicitly considered, as derived in Chapter 4 as a function of ambient conditions, conductor characteristics, and current. The conductor temperature is then used to inform the line conductor resistance, which in turn informs a power flow solution that will be shown to differ from the conventional algorithm in the case studies presented in Chapter 6.

Section 5.2.1 will present a description of the numbering and ordering scheme used for nodes and branches in the radial system. Section 5.2.2 will then describe the form of the matrices of system data that serve as input to the algorithm. Finally, section 5.2.3 will cover the implementation of the conventional algorithm itself.

5.2.1 Node/Branch Ordering

The numbering and ordering of nodes and branches in a radial system is a crucial component of any backward-forward sweep algorithm. The algorithm presented in this chapter operates on systems that have been organized based on the method of oriented ordering described in [20]. Node references in system data, as in that provided by the IEEE test feeder cases [62], may reference nodes by non-sequential numbering schemes that make application of any algorithm difficult. To overcome this issue, nodes may need to be renumbered and branch data logically linked to node data by appropriate numbering. Referring to Fig. 5.1, regardless of initial

node numbering, the slack or source node is given the index 1, and subsequent nodes are numbered from 2 to n_b, where n_b is the number of nodes or buses. The only requirement in the numbering of nodes is that the sending bus number should be smaller than the receiving bus number. Branch indices are then equal to the index of the receiving node, meaning that branch $i - k$ has index k. A fictitious branch with zero impedance is then introduced upstream of the source node so that the number of nodes and branches is equal. This strategy allows the coordination of nodes and associated branches necessary for the algorithm presented in section 5.2.3.

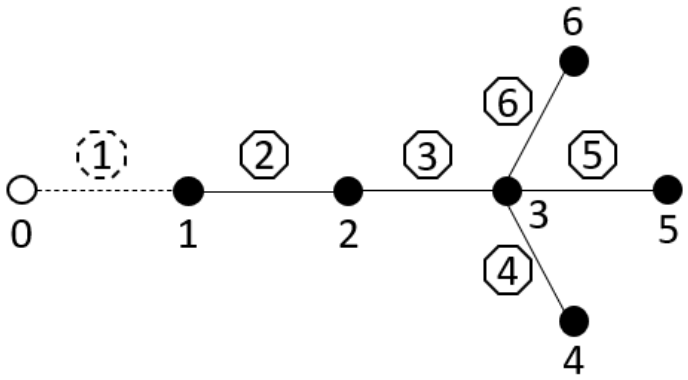

Figure 5.1: Node/branch numbering and ordering

5.2.2 Input System Data Matrices

Two numerical data matrices serve as input to the algorithm described in section 5.2.3, a node matrix containing shunt element data (i.e., load, capacitor, and nominal voltage data), and a branch matrix containing series element data (line, transformer, voltage regulator, switch). The matrices are organized to be compatible with the node/branch numbering and ordering scheme described in the previous section. The node matrix is organized sequentially by node number, with row index i containing the data for node i. The branch matrix is then organized sequentially by receiving branch number, such that the data for branch $i - k$ is in row $k - 1$.

Table 5.1: Node data matrix

Column	Description
1	Node number
2	Phase A wye-connected nominal real power load (kW)
3	Phase A wye-connected nominal reactive power load (kVar)
4	Phase B wye-connected nominal real power load (kW)
5	Phase B wye-connected nominal reactive power load (kVar)
6	Phase C wye-connected nominal real power load (kW)
7	Phase C wye-connected nominal reactive power load (kVar)
8	Phase A delta-connected nominal real power load (kW)
9	Phase A delta-connected nominal reactive power load (kVar)
10	Phase B delta-connected nominal real power load (kW)
11	Phase B delta-connected nominal reactive power load (kVar)
12	Phase C delta-connected nominal real power load (kW)
13	Phase C delta-connected nominal reactive power load (kVar)
14	Nominal node line-to-line voltage (kV)
15	Wye load code (1-constant impedance, 2-constant current, 3-constant power)
16	Delta load code (1-constant impedance, 2-constant current, 3-constant power)
17	Phase A nominal capacitor rating (kVar)
18	Phase B nominal capacitor rating (kVar)
19	Phase C nominal capacitor rating (kVar)
20	Connection type code for capacitor bank (1-wye, 2-delta)

Tables 5.1 and 5.2 detail the data contained in each column of the node and branch matrices respectively. Only a single series component exists between any two sequential nodes in a system. Therefore, in the case of a branch containing a series element of one type, such as a transformer, the data corresponding to a line section, voltage

regulator, or switch is set to zero and never accessed by the algorithm. A component code column in the branch matrix instructs the algorithm what series component to model for a particular branch.

Table 5.2: Branch data matrix

Column	Description
1	Sending node number
2	Receiving node number
3	Series component code (1-line, 2-transformer, 3-regulator)
4	Line length (ft)
5	Voltage transformer ratio (regulators)
6	Current transformer ratio (regulators)
7	Current transformer secondary current (A)
8	Voltage transformer ratio (not used)
9	Voltage level set point (regulators) (V, 120 V base)
10	Bandwidth (regulators) (V)
11	Line phase conductor resistance (Ω/mile)
12	Line neutral conductor resistance (Ω/mile)
13	Number of wires (4-wire, 3-wire, etc.) (lines)
14	Configuration code from [62] (lines)
15	Transformer resistance (pu)
16	Transformer reactance (pu)
17	Transformer nominal secondary line-to-line voltage (kV)
18	Transformer nominal primary line-to-line voltage (kV)
19	Transformer connection code (1: D-GY, 2: GY-GY, 3: D-D)

The node data matrix is constructed such that capacitor banks and wye- and delta-connected loads can exist simultaneously at a node. If only one load connection type

is present, then the second connection type load values and load code are set to zero. Similarly, if a capacitor is not present, the nominal kVar values and connection type code are set to zero.

5.2.3 Algorithm Description

In this section the implementation of the conventional, non-temperature-dependent three-phase power flow algorithm will be described in detail. The following section, 5.3, will augment this development by describing the modifications that introduce temperature-dependency to the power flow solution. The described algorithm is intended to operate on a purely radial system that has been organized and numbered as described in section 5.2.1 and takes as input the data matrices described in section 5.2.2. For the purposes of the descriptions in this section, *downstream* from a node will denote any and all paths that can be traced from a given node towards any and all end nodes that exist in a purely radial system. *Upstream* then denotes the singular path that can be traversed from a given node back towards the source node. The term *node current* will denote the algebraic sum of all currents *leaving* a node (i.e., to receiving nodes and into the load), *load current* denotes that portion of the node current that serves the load associated with a node, and *branch current* denotes the current that is delivered across a branch in the radial network, which is equal to the node current at the receiving node. *Backward* denotes the direction from end nodes to source node, and *forward* denotes the direction from source node to end nodes.

In a single power flow solution, the algorithm will converge up to three times, depending on the presence of voltage regulators at the substation (source node) and at other locations in the system. In the first convergence, all regulator tap settings are considered to be zero, and the regulators are treated essentially as a lossless line segment. Using the first converged solution, any regulator present at the substation or source node will be set, and the power flow again performed to convergence. Following the second convergence, the solution is then used to set any additional regulators that

may be present in the system. The power flow is again performed to yield the final solution.

The algorithm begins with the calculation of node load currents at each node based on the development of section 3.2. The backward sweep then begins with the end node with the highest index and crawls upstream towards the source node sequentially. Due to the requirement described in section 5.2.1 that the nodes be numbered such that all sending node numbers are smaller than their corresponding receiving nodes, the node current for a given sending node is gathered as a cumulative sum of all downstream load currents plus the load current present at the sending node itself. Voltage is also calculated in the backward sweep using the generalized series component equations 3.1 and 3.2 and the derivations given in sections 3.4, 3.5, and 3.6.

Once the backward sweep is completed, the forward sweep begins by resetting the source node voltage to its nominal value and traversing the system in the downstream direction towards the end nodes, using the currents calculated in the backward sweep, the sending end node voltages, and the generalized series component matrices to recalculate downstream node voltages. A single convergence is reached when the absolute difference between all voltages of successive iterations have reached a specified tolerance.

With reference to Fig. 5.2, the algorithm is as follows:

Step 1) Input data consisting of the data matrices described in section 5.2.2.

Step 2) Initialize all system node voltages as nominal line-to-neutral or equivalent line-to-neutral voltages for each phase present at a given node.

Step 3) Calculate load currents at each node based on the load modeling presented in section 3.2. In the first iteration the load currents are calculated using the initialized nominal voltages and nominal real and reactive powers as given in the input data matrices. Subsequent iterations will use calculated voltages.

Step 4) Beginning the backward sweep, set k equal to the number of branches, which is also equal to the number of nodes based on the development of section 5.2.1.

Step 5) Locate the sending node i of receiving node k. Note that in a purely radial system, a given node may have multiple downstream (receiving) nodes, but only a single upstream node.

Step 6) Determine the series component associated with branch k (line section, transformer, regulator, or switch).

Step 7) Calculate the generalized series component matrices a, b, c, and d that relate sending node voltages and currents to receiving node voltages and currents in the backward direction, as in Eqs. 3.1 and 3.2 and derived in detail for each series component in sections 3.4, 3.5, and 3.6. Note that a closed switch is treated as a line section with zero impedance.

Step 8) Calculate the sending node current I_i using the node load currents calculated in Step 3 and the generalized matrices of Step 7. Written in terms of the load current at node i, the node current and voltage at node k, and the generalized series component matrices:

$$[I_{abc}]_i = [I_{abc}]_i^L + [c]\,[V_{abc}]_k + [d]\,[I_{abc}]_k \tag{5.1}$$

For example, for an end node k that is the receiving node of sending node i, for branch $i-k$ that is a line segment with shunt admittance neglected, the node current at node i calculated in the backward sweep is:

$$[I_{abc}]_i = [I_{abc}]_i^L + [I_{abc}]_k^L \tag{5.2}$$

and the branch current is simply I_k^L.

Step 9) Calculate sending node voltage V_i as a function of the generalized series component matrices of Step 7, the receiving node voltage V_k, and the branch current $[I_{abc}]_k$ as:

$$[V_{abc}]_i = [a]\,[V_{abc}]_k + [b]\,[I_{abc}]_k \tag{5.3}$$

Step 10) Decrement k by 1 and proceed to receiving node index $k-1$.

Step 11) If $k = 1$, the source node has been reached and proceed to the forward sweep beginning with Step 12. Otherwise, return to Step 5 and continue backward sweep with next receiving node k.

Step 12) Reset the source node voltages to the nominal line-to-neutral or equivalent line-to-neutral values.

Step 13) Set receiving node index $k = 2$.

Step 14) Locate the sending node i of receiving node k.

Step 15) Determine the series component associated with branch k (line section, transformer, regulator, or switch).

Step 16) Calculate the generalized series component matrices A and B that relate receiving node voltage to sending node voltage and receiving node current

(branch current for branch $i-k$) in the forward direction, as in Eq. 3.3 and derived in detail for each series component in sections 3.4, 3.5, and 3.6.

Step 17) Calculate receiving node voltage V_k as a function of the generalized series component matrices of Step 16, the sending node voltage V_i, and the branch current $[I_{abc}]_k$ (node current at node k) calculated in Step 8 of the backward sweep. In terms of the generalized series component matrices:

$$[V_{abc}]_k = [A]\,[V_{abc}]_i - [B]\,[I_{abc}]_k \tag{5.4}$$

Step 18) Increment k by 1 and proceed to next receiving node index.

Step 19) If $k = nl + 1$, where nl is the number of branches, then the final end node has been reached and proceed to check for convergence in Step 20. Otherwise, return to Step 14 and continue forward sweep.

Step 20) If all absolute values of the difference between the previous iteration voltages and the current iteration voltages are within a specified tolerance, the first convergence is satisfied and proceed to set the substation (source) voltage regulator, if present, in Step 21. Otherwise, return to Step 3 to begin another iteration with the backward sweep. The first iteration of the backward-forward sweep is complete.

Step 21) If the regulator at the source node does not exist, or does exist and has been set, proceed to check if other regulators exist and have been set in Step 23. Otherwise, proceed to Step 22 to determine the substation regulator tap settings from the first converged solution.

Step 22) Determine tap settings and generalized regulator matrices from the devel-

opment in section 3.6 and the first converged power flow solution. Reinitialize all node voltages to nominal line-to-neutral or equivalent line-to-neutral values in preparation for another performance of the power flow. Proceed to Step 3 and begin second power flow to convergence.

Step 23) If no other regulators exist besides the regulator at the source node, or they exist but have previously been set, the converged power flow solution is final and the algorithm ends. Otherwise, proceed to Step 24 to determine the other regulator tap settings from the second converged solution.

Step 24) Determine tap settings and generalized regulator matrices from the development in section 3.6 and the second converged power flow solution. Reinitialize all node voltages to nominal line-to-neutral or equivalent line-to-neutral values in preparation for another performance of the power flow. Proceed to Step 3 and begin third power flow to convergence.

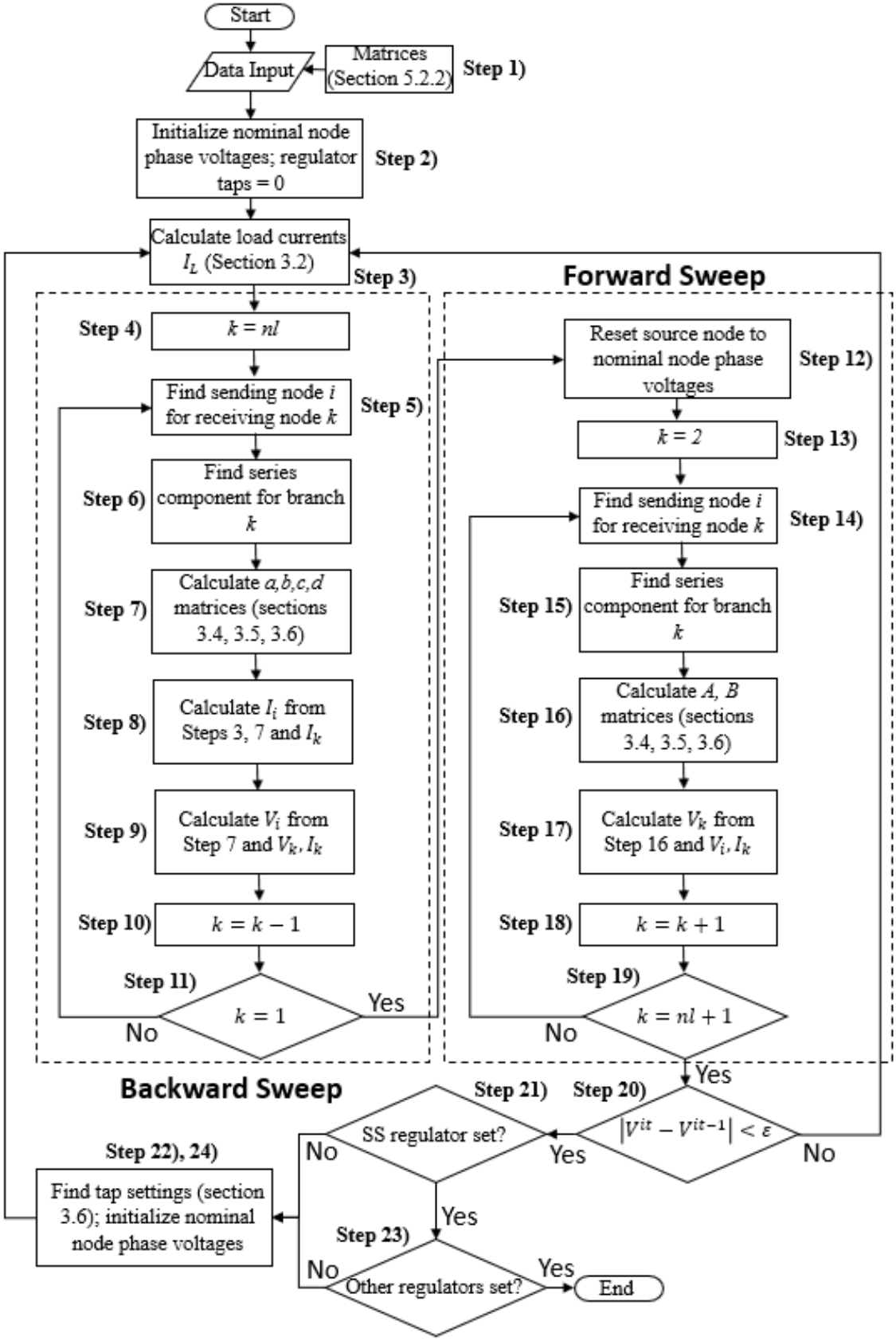

Figure 5.2: Conventional backward-forward sweep power flow algorithm

5.3 Temperature-Dependent Backward-Forward Sweep Power Flow Algorithm

This section will describe the modifications made to the algorithm presented in the previous section that will couple the electrical and the thermal characteristics of overhead and underground line sections to achieve a *temperature-dependent three-phase power flow algorithm for radial distribution systems.* In the algorithm presented in section 5.2, the line conductor temperature and subsequent resistance is considered fixed regardless of line current and ambient conditions. In contrast, the modifications presented in this section will use the development of Chapter 4 to explicitly calculate the conductor temperature and corresponding resistance as a function of the conductor temperature, and then use the calculated resistances to inform the generalized series component matrices for the line sections (section 3.4).

In the proposed temperature-dependent power flow algorithm presented in this section, the conductor temperature and corresponding resistance for each conductor of each individual line segment is calculated twice during every iteration of the backward-forward sweep algorithm, once during the backward sweep and once during the forward sweep. Referencing Fig. 5.2, this temperature and resistance calculation occurs between Steps 6 and 7 in the backward sweep, and Steps 15 and 16 in the forward sweep. The modifications to the algorithm, with reference to Fig. 5.3, can be described as follows:

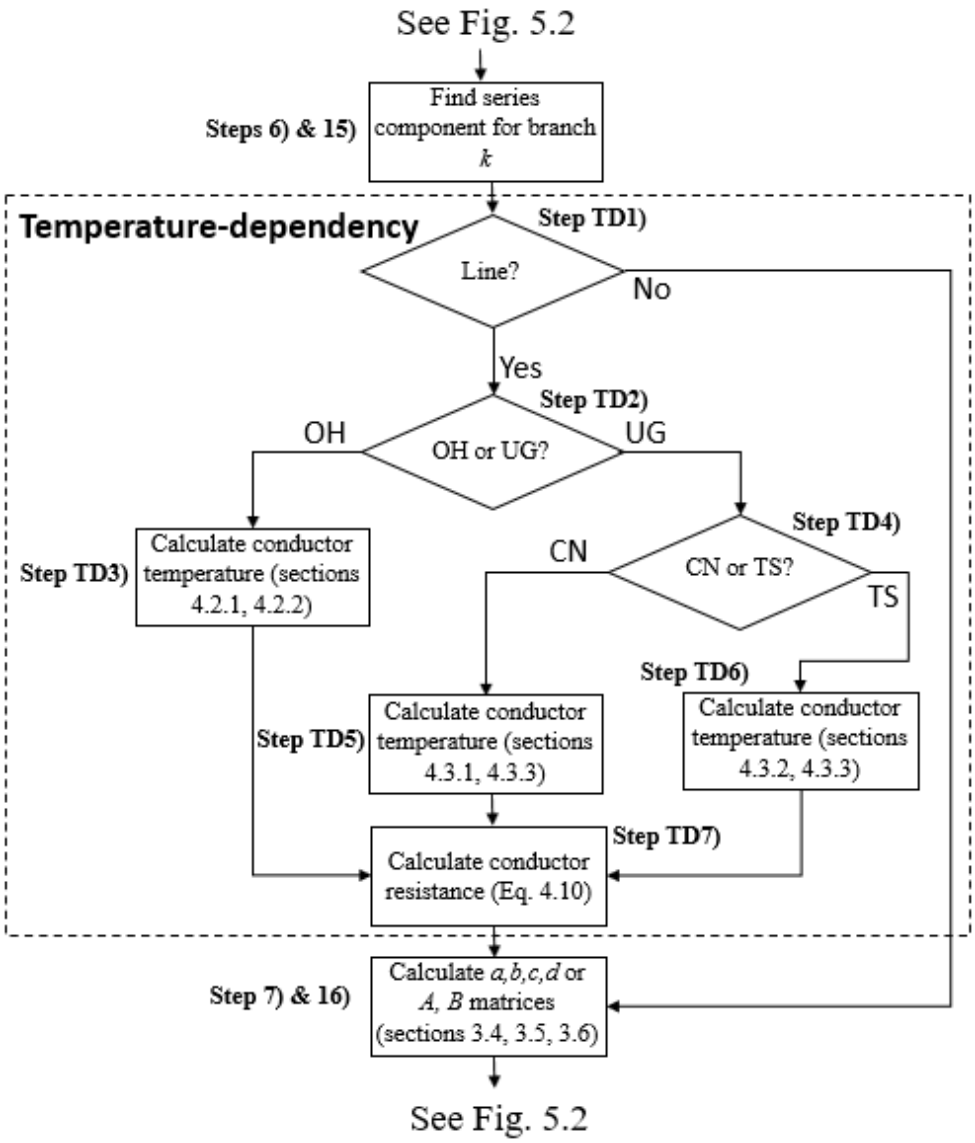

Figure 5.3: Temperature-dependency introduced to the backward-forward sweep power flow algorithm of section 5.2

Step TD1) If series component for branch k is a line section, proceed to Step TD2. Otherwise, proceed to Step 7 (backward sweep) or Step 16 (forward sweep).

Step TD2) If the line section is an overhead line of bare conductors, proceed to Step TD3. Otherwise, if the line section is an underground cable section, proceed to Step TD4.

Step TD3) Calculate conductor temperature based on the development of section

4.2 using the bisection algorithm as presented in Fig. 4.1.

Step TD4) If the underground section is composed of concentric neutral cable, proceed to Step TD5. Otherwise, if the underground section is composed of tape-shielded cable, proceed to Step TD6.

Step TD5) Calculate conductor temperature based on the development of section 4.3.1 using the algorithm as presented in Fig. 4.6.

Step TD6) Calculate conductor temperature based on the development of section 4.3.2 using the algorithm as presented in Fig. 4.6.

Step TD7) Interpolate conductor resistance using Eq. 4.9 and the conductor temperature as calculated in Steps TD3, TD5, or TD6. This resistance as a function of temperature will then be used to calculate the generalized series component matrices for the line section in Step 7 (backward sweep) or Step 16 (forward sweep) as appropriate.

As a visual representation of the differences between the conventional power flow algorithm (section 5.2) and the temperature-dependent power flow algorithm (current section), Fig. 5.4 shows the conductor temperature, resistance, and current characteristics for one phase conductor over one complete power flow iterative cycle to convergence, including the setting of the regulators, as described in the current section and in section 5.2. It can be noted that in the conventional algorithm, the conductor temperature and corresponding resistance are assumed constant. In the temperature-dependent algorithm, the conductor temperature is calculated at each iteration using the development of Chapter 4 and then is used to determine the corresponding conductor resistance per Eq. 4.9. This is done for each phase conductor of a given system, and the cumulative effect of the changing resistances has an additional effect on the iterative calculation of the current through the phase conductor. The

current calculated by the conventional algorithm still changes iteratively due to the normal processes of the algorithm's convergence, but it can be noted that the final values of current calculated by the two algorithms are different, in this case varying by approximately 0.25%.

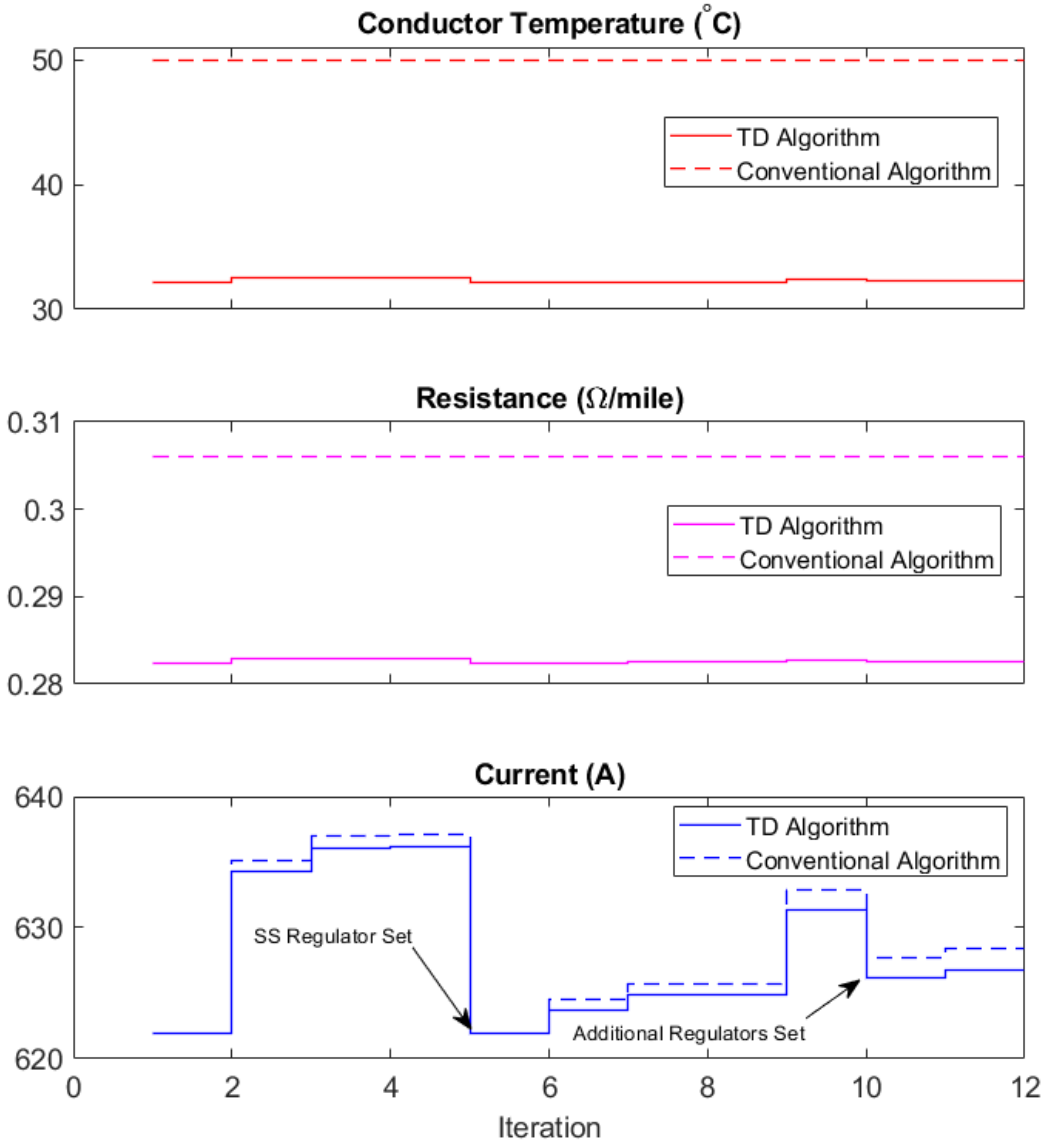

Figure 5.4: Representation of differences in the conventional and temperature-dependent power flow algorithms

This chapter described the proposed temperature-dependent three-phase power

flow algorithm for radial distribution systems with both overhead and underground line sections. The next chapter will present results obtained using this novel algorithm for specific test cases as compared to the results obtained by the conventional algorithm which does not take into account conductor temperature dependency on ambient conditions and line current, as described in Chapter 4.

CHAPTER 6: CASE STUDIES

6.1 Overview

In this chapter both the conventional (section 5.2) and the temperature-dependent (section 5.3) radial power flow algorithms will be presented as applied to the 13- and 123-node test feeders provided by the IEEE PES AMPS DSAS Test Feeder Working Group [62]. The conventional algorithm is presented as verification of the accuracy of the calculations as compared to the benchmark results given in [62]. The results of the temperature-dependent algorithm will then be shown to differ from the benchmark results with respect to voltage profile, real power losses, and degree of voltage unbalance.

The following sections 6.2 and 6.3 describe the assumptions necessary to perform the temperature-dependent power flow analysis of the test feeder systems and describe the data sets used. Cable and line parameters not given in the original test feeder data, installation specifics (burial depth, etc.) for underground cables, and assumptions about certain weather and overhead line parameters are detailed. Numeric values for each of these parameters, where applicable, are given, as well as the source for this information.

The first section in each of the case studies (sections 6.4.1 and 6.5.1) presented in this chapter will present the results of the conventional algorithm with respect to the benchmark solution. The second section in each case study (sections 6.4.2 and 6.5.2) presents the results of the proposed temperature-dependent power flow, and each of these sections is further subdivided into two test cases. First, two extreme scenarios will be presented, both for highly favorable (low conductor temperature and resistance) and highly unfavorable (high conductor temperature and resistance)

conditions. Next, a steady-state time-series power flow study is conducted over the course of a year using weather and soil temperature data obtained for 2020 [63], [64].

6.2 Temperature-Dependent Algorithm Assumptions

The temperature-dependent power flow algorithm of section 5.3 makes certain assumptions concerning the parameters serving as input to the line conductor temperature calculation methods given in Chapter 4, which are described below. Additionally, the algorithm assumes that the line geometry is fixed for all conductor temperatures, i.e., the spacing between conductors, distance from conductor to ground (for overhead lines), geometric mean radii, and conductor diameters do not change with temperature. In this model, only the elements of the line primitive impedance matrices (see section 3.4) containing a resistance term vary with conductor temperature.

The variable inputs for the calculation of conductor temperature and corresponding resistance for overhead line sections in the bisection algorithm of section 4.2 are line current, wind speed, ambient temperature, time of day, day of the year, and the size and type of conductor. Other parameters are considered fixed for all line sections for a given system and are given as shown in Table 6.1.

Table 6.1: Fixed parameters for calculation of overhead conductor temperature

Parameter	Description	Value
ϕ	Wind angle	45°
Lat	Latitude	35.227°
H_e	Elevation	272 m
ϵ	Emissivity	0.8
α	Solar absorptivity	0.8
-	Line orientation	E-W
-	Atmosphere condition	Clear

The wind angle of 45 degrees represents the angle between the wind direction and

the conductor axis and was chosen as the middle ground between the most favorable (90 degrees) and least favorable (0 degrees) angle for cooling of the line. The latitude and elevation are representative of the Charlotte, NC area, and the emissivity and solar absorptivity values are characteristic of overhead conductors that have been in the field for a number of years [7]. The line orientation and atmospheric condition selected are arbitrary, and could be adjusted as necessary.

The variable inputs for the calculation of conductor temperature and corresponding resistance for underground cable are line current, soil temperature, and size and type of conductor. The configurations (number of cables, axial separation) also play a role in the temperature calculation, and these factors are as given in the configuration data for each test case. Both types of cable considered, concentric neutral and tape-shielded, are assumed direct buried in earth at a distance of 40 inches (1.016 m) below ground level in damp soil that is 75% clay and 25% sand, which is typical of the Charlotte, NC area [65]. Other parameters needed for the calculations of section 4.3 can be found in Tables 6.2, 6.3, and 6.4 for the two sizes of concentric neutral cable and the one size of tape-shielded cable considered.

The materials used in the construction of the cables (insulation, jacket, etc.) and cable layer dimensions are taken from [60] for the concentric neutral cables and the construction from [61] and dimensions from [62] for the tape-shielded cable. The thermal resistivity of soil is taken from [66], and thermal resistivities for the insulation and jacket materials from [30]. The resistance of the sheath or screen (the concentric neutral wires themselves for the concentric neutral cable) and tape-shield are calculated as in [27].

Table 6.2: Fixed parameters for 250 MCM AA concentric neutral cable, 1/3 neutral, 15 kV (13-node case, configuration 606)

Parameter	Description	Value
ρ_{t1}	Thermal resistivity of insulation	5.0 K·m/W (EPR)
ρ_{t3}	Thermal resistivity of jacket	3.5 K·m/W (PE)
ρ_{t4}	Thermal resistivity of soil	0.75 K·m/W
t_1	Thickness of insulation between conductor and sheath	5.185 mm
t_3	Thickness of jacket	2.71 mm
D_a	External diameter of bedding beneath jacket	25.53 mm
R_s	Resistance of sheath or screen	0.000711 Ω/m

Table 6.3: Fixed parameters for 1/0 AA concentric neutral cable, 1/3 neutral, 15 kV (123-node case, configuration 12)

Parameter	Description	Value
ρ_{t1}	Thermal resistivity of insulation	5.0 K·m/W (EPR)
ρ_{t3}	Thermal resistivity of jacket	3.5 K·m/W (PE)
ρ_{t4}	Thermal resistivity of soil	0.75 K·m/W
t_1	Thickness of insulation between conductor and sheath	5.05 mm
t_3	Thickness of jacket	3.055 mm
D_a	External diameter of bedding beneath jacket	20.57 mm
R_s	Resistance of sheath or screen	0.00154 Ω/m

Table 6.4: Fixed parameters for 1/0 AA tape-shielded cable (13-node case, configuration 607)

Parameter	Description	Value
ρ_{t1}	Thermal resistivity of insulation	5.0 K·m/W (EPR)
ρ_{t3}	Thermal resistivity of jacket	3.5 K·m/W (PE)
ρ_{t4}	Thermal resistivity of soil	0.75 K·m/W
t_1	Thickness of insulation between conductor and sheath	5.74 mm
t_3	Thickness of jacket	2.032 mm
D_a	External diameter of bedding beneath jacket	22.352 mm
R_s	Resistance of sheath or screen	0.0027 Ω/m

The resistances calculated by linear interpolation through the use of Eq. 4.9 utilize a piece-wise linear model of conductor resistance whereby the resistance at $50°C$ is that as given in the original test feeder data for all conductors. For ACSR and AA conductors, the values of resistance at $25°C$ and $75°C$ are taken from [31] and for copper conductors are taken from [67]. The next section will describe the weather and soil temperature data sets used in the case studies.

6.3 Weather and Soil Data

This section will describe the wind speed and ambient air and soil temperature data used in the temperature-dependent power flow algorithm. The data sets will be used directly in the steady-state time-series cases for both the 13- and 123-node test feeders, and the minimum and maximum values will be extracted and used for the examples of extreme conditions that are also presented.

The soil ambient temperature data for the year 2020 is taken from the United States Department of Agriculture (USDA) Natural Resources Conservation Service, National Water and Climate Center at a depth of 40 inches in Washington County, NC [64] as a daily average measurement. This granularity is acceptable as the soil

temperature changes slowly as compared to the air temperature. The soil temperature is assumed comparable to that found in the Charlotte, NC area, approximately 300 miles away.

The air ambient temperature and wind speed data for the year 2020 is taken from the National Oceanic and Atmospheric Administration (NOAA) National Centers for Environmental Health at the Charlotte Douglas airport weather station in Charlotte, NC [63]. The measurements from the station are reported at irregular intervals (approximately every ten minutes), and for both wind speed and ambient air temperature the measurements closest to every hour have been extracted for use in the steady-state time-series power flow. Table 6.5 summarizes the characteristics of the data sets.

It can be noted that the ambient air temperature has a high variance as compared to the soil temperature, which remains more constant throughout the year, although the average soil and air temperatures are comparable. The mean of the wind speed is skewed towards the lower end of its range with a small standard deviation. These characteristics can be further visualized in the histograms of Figs. 6.1-6.3. Each set of data is composed of 8,784 hourly measurements (2020 was a leap year). The time-series data for ambient air and soil temperature can be viewed in Fig. 6.4 and for wind speed in Fig. 6.5.

Table 6.5: Weather and soil data characteristics

Variable	Max	Min	Mean	Std. Dev.
Wind speed	15.19 m/s	0 m/s	2.84 m/s	1.86 m/s
Ambient air temp	35.56 $^{\circ}C$	-7.22 $^{\circ}C$	17.19 $^{\circ}C$	8.37 $^{\circ}C$
Ambient soil temp	25.56 $^{\circ}C$	11.67 $^{\circ}C$	18.38 $^{\circ}C$	4.32 $^{\circ}C$

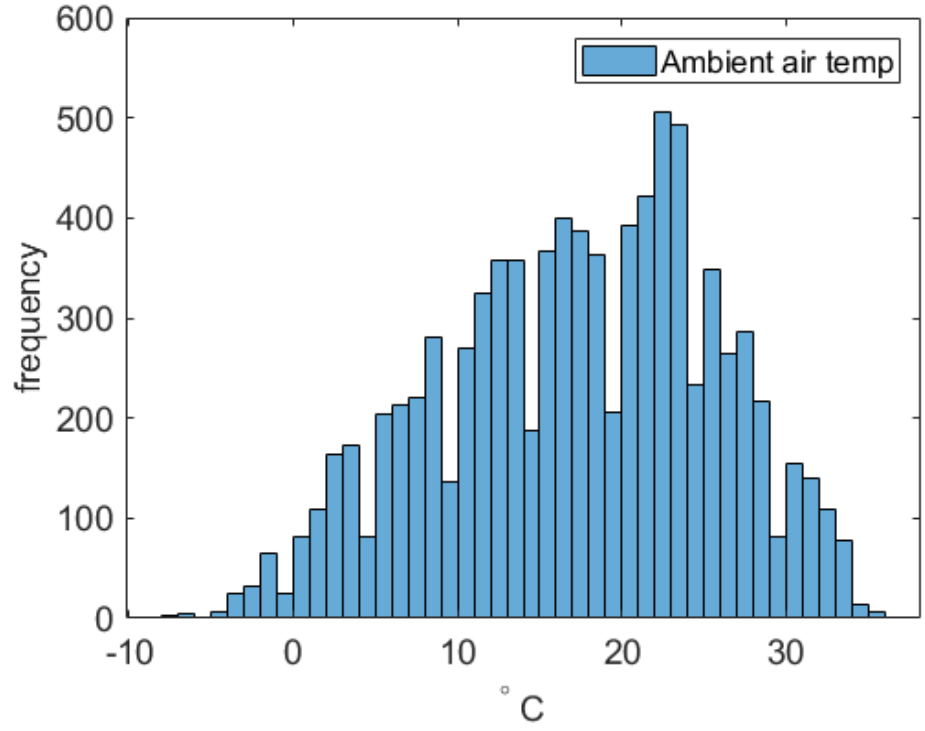

Figure 6.1: Ambient air temperature histogram, 2020

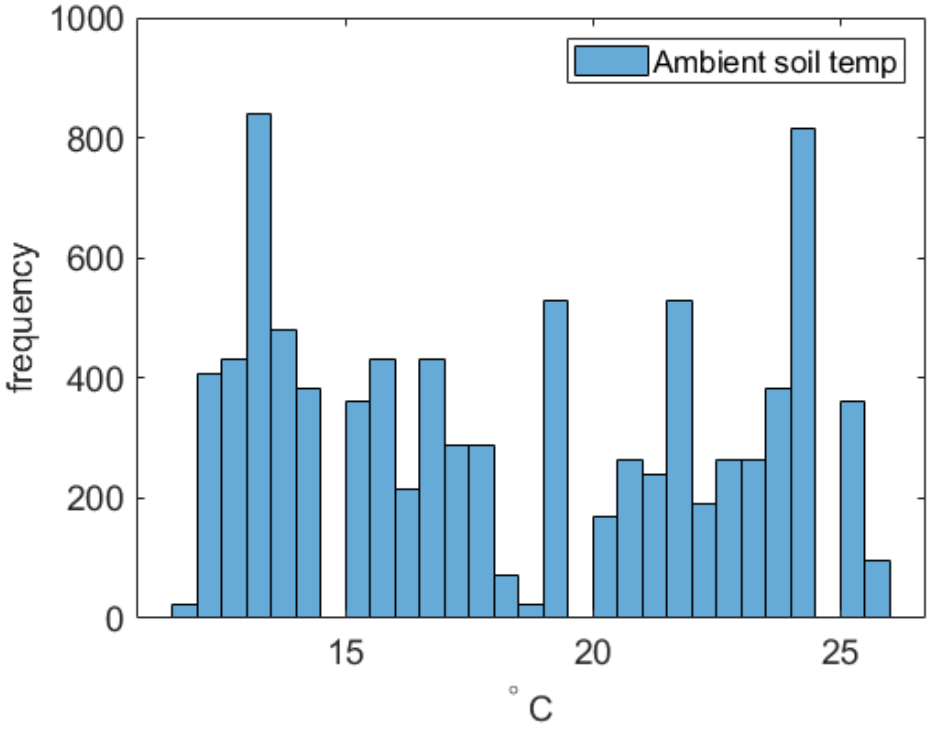

Figure 6.2: Ambient soil temperature histogram, 2020

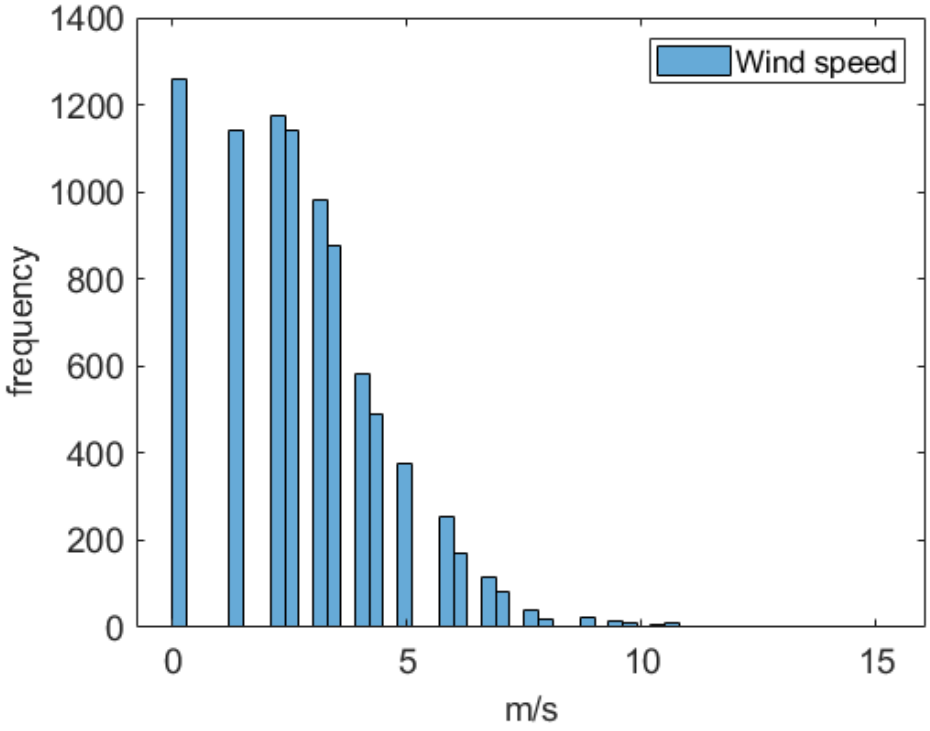

Figure 6.3: Wind speed histogram, 2020

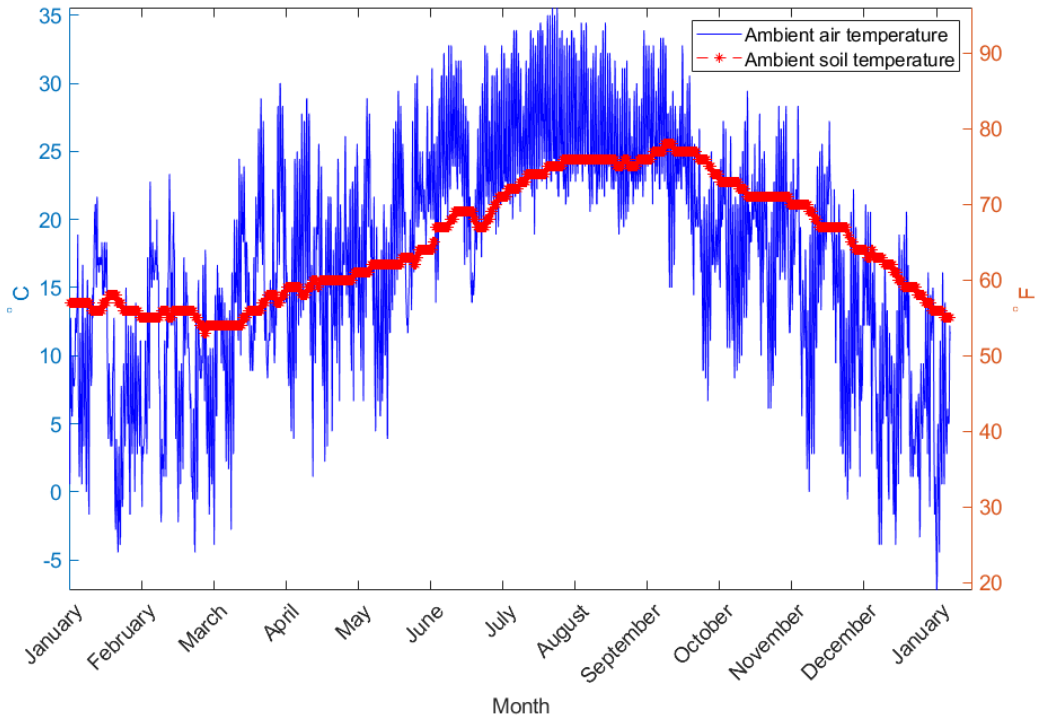

Figure 6.4: Ambient soil and air temperature, 2020

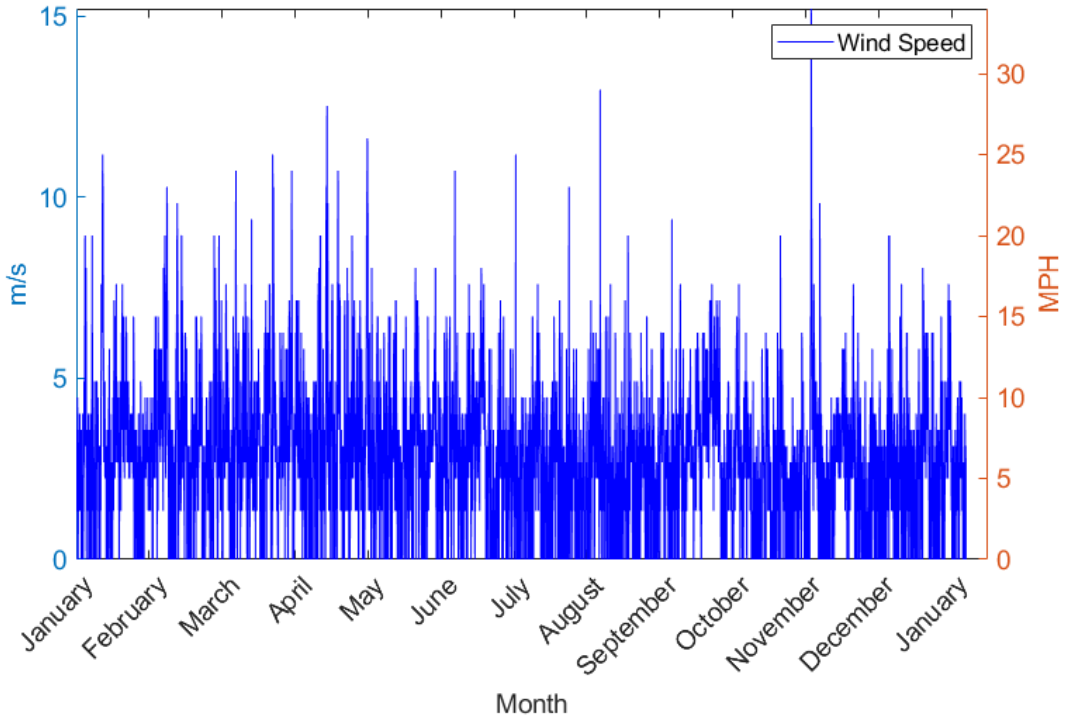

Figure 6.5: Wind speed, 2020

6.4 13-Node Test Feeder

The IEEE 13-node test feeder can be viewed in Fig. 6.6. The test feeder contains a combination of one-, two-, and three-phase line sections, one-, two-, and three-phase constant current, impedance, and power loads configured in both delta and wye, two capacitor banks, one voltage regulator and one transformer located at the substation (source) node, and a second transformer located between nodes 633 and 634. All lines are composed of overhead ACSR conductors except for line 692-675 (underground concentric neutral cable) and line 684-652 (underground tape-shielded cable). All data required for the conventional power flow analysis can be found at the IEEE PES AMPS DSAS Working Group website [62].

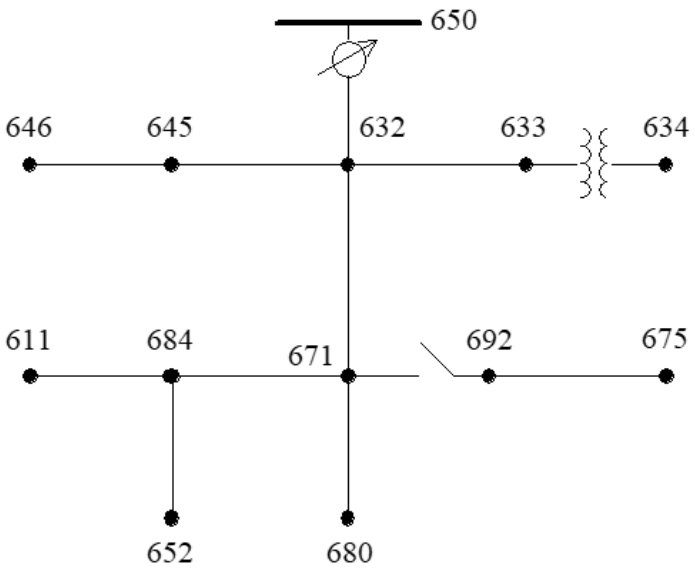

Figure 6.6: IEEE 13-node test feeder

The section that follows will compare the results of the algorithm presented in section 5.2 to the benchmark results as given in [62].

6.4.1 Conventional Algorithm Comparison to Benchmark

This section will present the results of the application of the conventional (non-temperature-dependent) three-phase backward-forward sweep algorithm (section 5.2) to the IEEE PES 13-node test feeder [62]. These results assume, as in the original test feeder data, that all conductor resistances correspond to a uniform conductor temperature of $50°C$ across the entirety of the feeder. The results of the section 5.2 algorithm are compared to the benchmark solution as given by [62] to confirm the accuracy of the algorithm before modifications are made to introduce temperature-dependency, as discussed in section 5.3.

Fig. 6.7 shows the benchmark voltage profile as given in [62] in comparison to the results of the conventional power flow algorithm of section 5.2, and Table 6.6 gives the average absolute error for each phase in the calculation of the voltage as well as the maximum absolute voltage error with respect to the comparison between the benchmark results and the section 5.2 algorithm. The voltages as calculated by

the section 5.2 algorithm are noted to be in very close agreement to those of the benchmark.

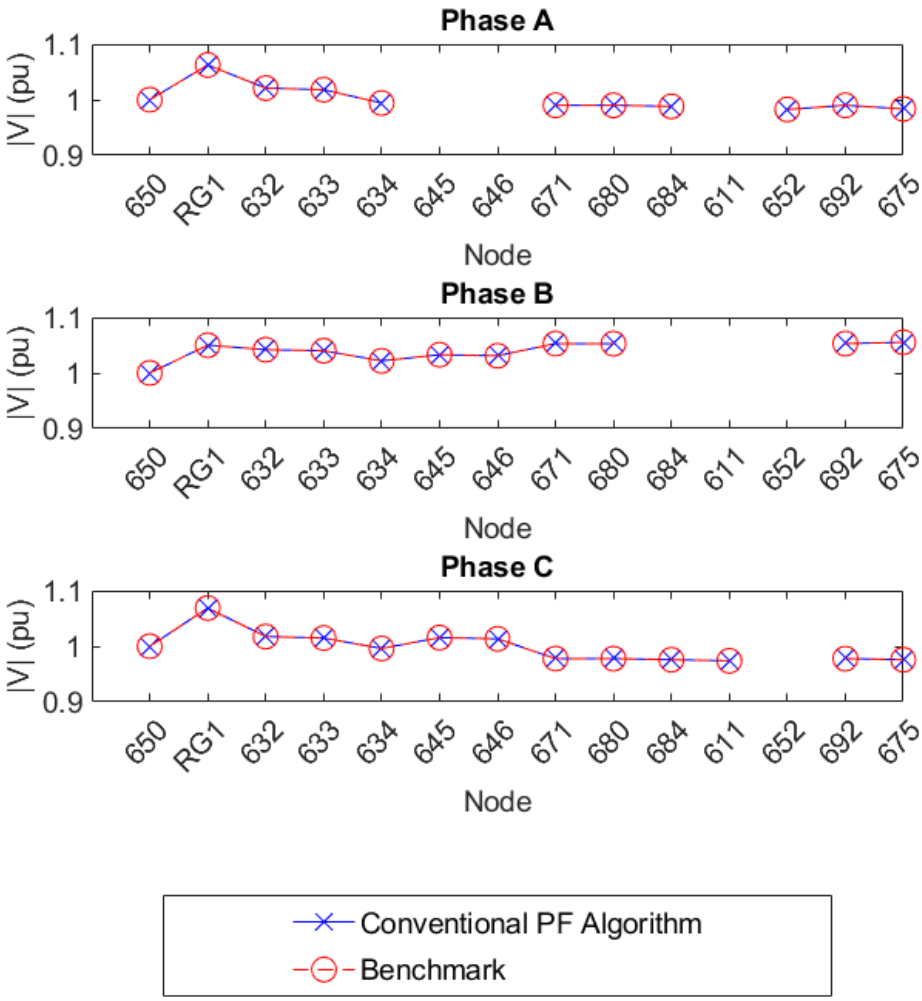

Figure 6.7: IEEE 13-node test feeder voltage profile

Table 6.6: Comparison to benchmark results: voltage error, 13-node feeder

Average Absolute Error			
Phase A (pu)	Phase B (pu)	Phase C (pu)	Maximum Error (pu)
$1.86 \cdot 10^{-5}$	$1.74 \cdot 10^{-5}$	$7.95 \cdot 10^{-5}$	$1.76 \cdot 10^{-4}$

Table 6.7 gives the comparison of the real power loss calculated by the section 5.2 algorithm to the benchmark results. The error in calculated total real power loss between the section 5.2 algorithm and the benchmark is approximately 85 watts, or 0.08%.

Table 6.7: Comparison to benchmark results: real power loss, 13-node feeder

	Phase A (kW)	Phase B (kW)	Phase C (kW)	Total (kW)
Benchmark	39.107	-4.697	76.653	111.063
Conventional PF	39.130	-4.728	76.576	110.978
Error	-0.023	0.031	0.077	0.085

The degree of voltage unbalance at each node is calculated using the National Electrical Manufacturers Association (NEMA) definition [27] as:

$$V_{unbalance} = \frac{|\text{Maximum deviation from average}|}{|V_{average}|} * 100\% \tag{6.1}$$

Using this definition, the maximum voltage unbalance can be calculated from the benchmark test results and from the results of the section 5.2 algorithm. The maximum voltage unbalance occurs at the end node 675, and is calculated for the section 5.2 algorithm and the benchmark as 5.01% and 5.02% respectively.

6.4.2 Temperature-Dependent Algorithm Results

The following sections will demonstrate the application of the proposed temperature-dependent three-phase power flow algorithm presented in section 5.3 to the 13-node test feeder. The first application in section 6.4.2.1 will assume two 'extreme' scenarios, a best- and worst-case for cooling of the lines. The second application in section 6.4.2.2 will use the complete data sets of section 6.3 in a steady-state time-series analysis.

6.4.2.1 Extreme Scenarios

In this section, two 'extreme' scenarios are tested, using the most and least advantageous combinations of ambient conditions in terms of cooling of the line sections. The most advantageous combination is expected to generate lower losses due to comparatively cooler line sections, and the least advantageous is anticipated to produce the opposite effect.

The combination of conditions to produce the most advantageous conditions for cooling of the line sections in terms of the variable inputs to the electrothermal coupling algorithms for overhead and underground lines (Chapter 4) are minimum solar heating and ambient air and soil temperature, and maximum wind speed. The least advantageous conditions for cooling of the line sections are the opposite, maximum solar heating and ambient temperatures and minimum wind speed.

Two things can be acknowledged here. Firstly, these conditions do not necessarily occur simultaneously in the data sets of section 6.3. The intent of the extreme scenario case is to represent the breadth of results due to ambient conditions. Secondly, the most advantageous conditions for cooling occur at night (no solar heating). The load used for all cases remains constant and is as given in the test feeder data. It is acknowledged that the load at night, due to cyclical variations in load patterns, is not directly comparable to the load during the day. It is the belief of the author that

the result still contains valuable information with the load remaining constant over the duration of the study.

The highest solar heating occurs at 12 noon on June 20th, 2020, which corresponds to the summer solstice. The maximum air ambient temperature occurs in mid July, and the minimum wind speed (no wind) occurs variously around this time and indeed throughout the year, so it is reasonable to assume these factors could occur at the same time. The soil temperature variation lags the variation in air temperature, and the maximum value occurs in early September.

The lowest solar heating occurs overnight throughout the year. The minimum air ambient temperature occurs in late December and the maximum wind speed occurs in October, although some comparably high wind speeds occur in early January. The minimum soil temperature occurs in late February. Again, it is considered reasonable to consider that these factors could occur simultaneously as will be considered for this portion of the study. The combinations used for the most and least advantageous cooling scenarios, heretofore referred to as 'cooler' and 'warmer' respectively, can be viewed in Table 6.8. The numeric value of solar heating varies by conductor during daytime hours, and is given as the date and/or time of occurrence.

Table 6.8: Extreme condition parameters

	Air temp ($°C$)	Soil temp ($°C$)	Wind speed (m/s)	Solar heating
Cooler	-7.22	11.67	15.19	Overnight (0)
Warmer	35.56	25.56	0	6/20, 12pm (various)

The heatmap of Fig. 6.8 shows the calculated temperatures (see Chapter 4) for all overhead and underground line sections in the 13-node test feeder for both the cooler and warmer cases described above. The vertical axes are annotated by phase, and the horizontal axes by the branch receiving node. Only branches corresponding to overhead and underground line sections are shown (transformer, switch, and regulator

branches omitted). Additionally, the temperatures of phases not present for a given line section are shown as NaN (not a number).

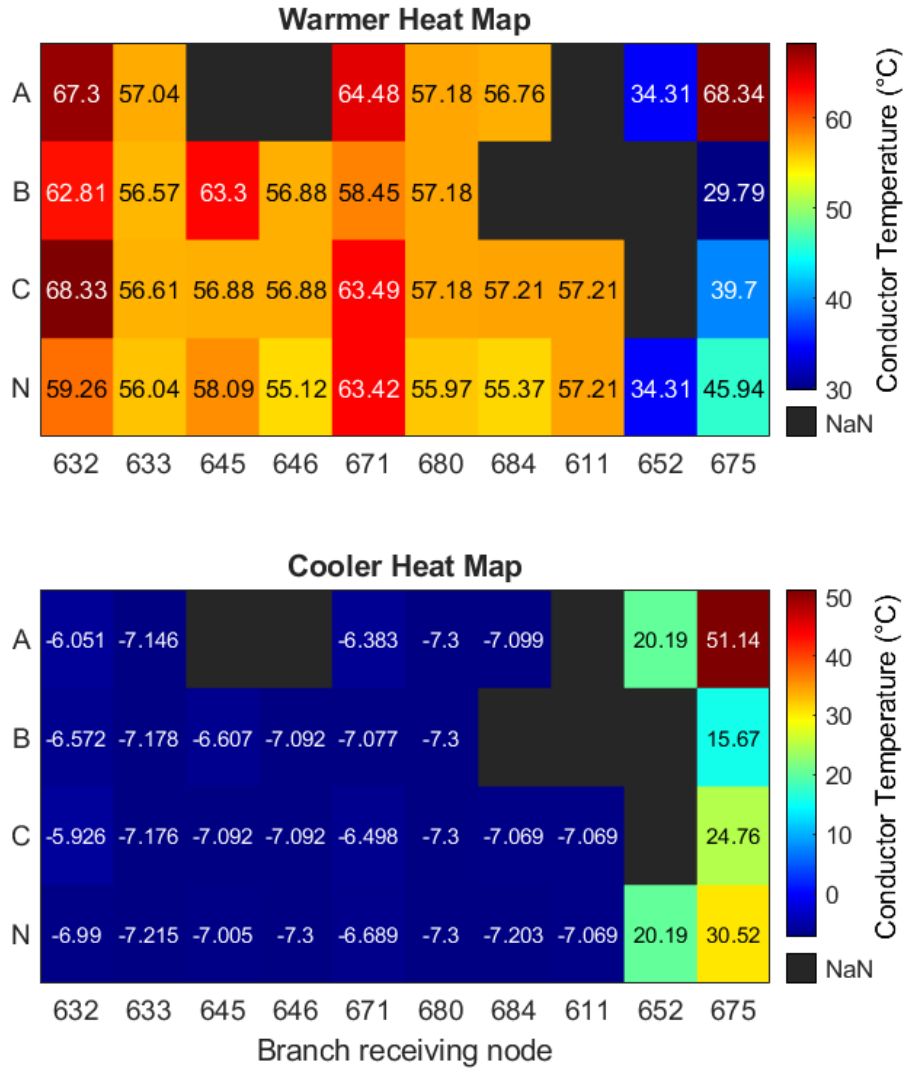

Figure 6.8: 13-node feeder: branch heatmap, cooler and warmer extreme conditions

The top portion of Fig. 6.8 shows the heatmap corresponding to the warmer scenario, and the lower portion the cooler scenario. The final two columns of the heatmaps correspond to underground line sections, with all other columns representing overhead line sections. It can be noted that the deviation in temperature for the overhead line sections is much greater than that for the underground sections when

comparing the warmer and cooler scenarios, the variability in wind, solar heating, and ambient air temperature being much greater than that of the soil temperature. The difference between the calculated underground line temperatures of the two cases is approximately equal to the difference in the considered soil temperature, the temperature rise above ambient being approximately equal. It can also be noted that the underground line sections stay much warmer than the overhead lines in the cooler case, and much cooler than the overhead lines in the warmer case, again due to the relative stability of the soil temperature as compared to the weather conditions.

Considering that the benchmark power flow case considered a consistent temperature of $50°C$ for all line sections, the deviation from the baseline conductor temperature assumption is very great in some cases, particularly in the cooler case. All overhead line sections have temperatures far below the baseline assumption in the cooler case. In the warmer case, the overhead line sections have temperatures that are consistently higher than the baseline. In both cases, the conductor temperatures of the underground line sections are below the baseline assumption, except for the phase A conductor of branch 692-675 (last column of heatmap).

Table 6.9 gives the average absolute deviation in voltage magnitude of each phase and the maximum deviation for the cooler and warmer extreme cases as compared to the benchmark solution. The deviations are relatively small, with the maximum deviation in the cooler case approaching 0.01 pu. This close agreement is not due to the action of the voltage regulator, as the calculated tap settings are the same in both cases, and are the same as the tap settings of the benchmark. There is simply not much of a difference in the calculated voltage drops due to the differences in conductor temperature and corresponding conductor resistance and line current. From this result, the conclusion may be drawn that, for this particular feeder, the conductor temperature does not have a great impact on the calculated node voltage magnitudes. This result can be viewed graphically in Fig. 6.9.

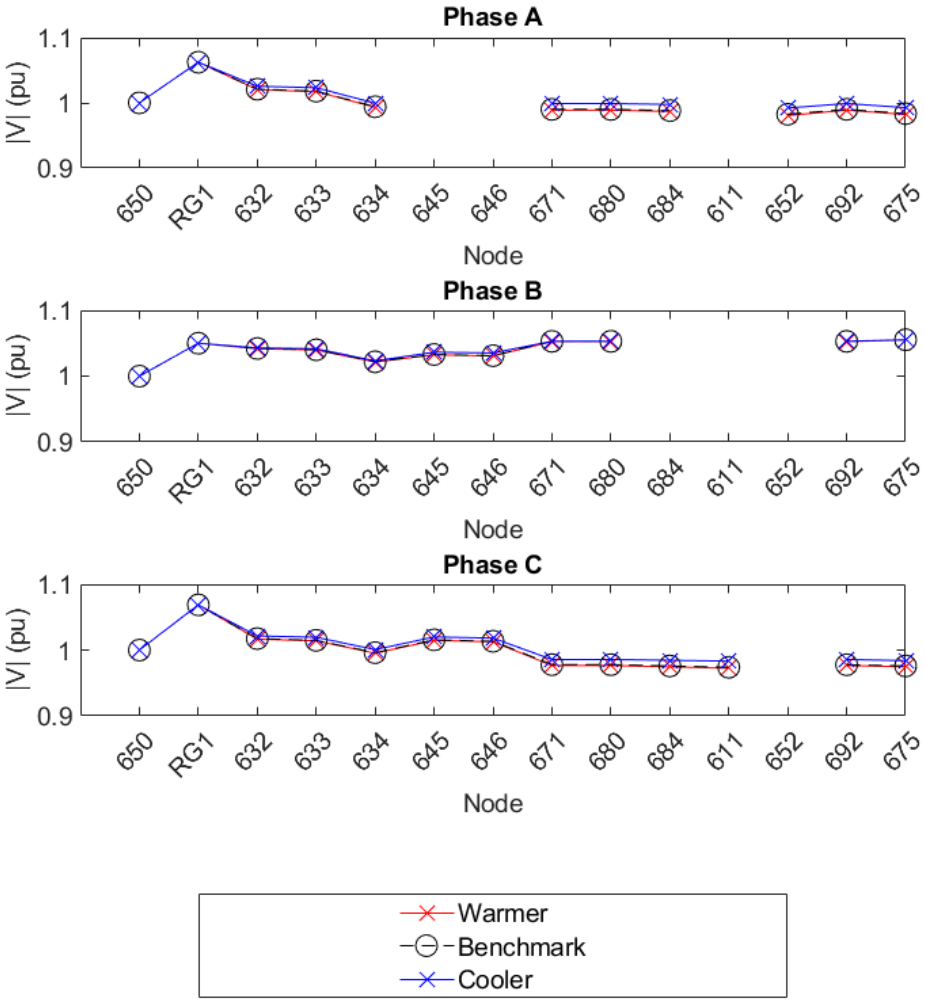

Figure 6.9: 13-node feeder: voltage profile, cooler and warmer extreme conditions

Table 6.9: Comparison to benchmark results: voltage deviation, cooler and warmer extreme conditions, 13-node feeder

	Average Absolute Deviation			
	Phase A (pu)	Phase B (pu)	Phase C (pu)	Maximum Deviation (pu)
Cooler	$6.4 \cdot 10^{-3}$	$1.1 \cdot 10^{-3}$	$5.6 \cdot 10^{-3}$	$9.6 \cdot 10^{-3}$
Warmer	$9.5 \cdot 10^{-4}$	$3.1 \cdot 10^{-4}$	$8.8 \cdot 10^{-4}$	$1.9 \cdot 10^{-3}$

In contrast to the calculated voltages, the calculated losses vary by a much greater percentage when comparing the two extreme cases. Table 6.10 gives the losses calculated, by phase and in total, for each extreme case and the benchmark solution. The negative loss on phase B is a result of the comparatively light loading on that phase and the effect of phase coupling on the line segment [27] and can also be seen in the original IEEE results.

Table 6.10: Extreme cases and benchmark results: real power loss, 13-node feeder

	Phase A (kW)	Phase B (kW)	Phase C (kW)	Total (kW)
Benchmark	39.11	-4.70	76.65	111.06
Warmer	40.95	-4.34	78.49	115.10
Cooler	28.91	-6.43	64.19	86.66

The total losses for the warmer case are 3.6% greater than the benchmark, and the losses calculated in the cooler case are 22% less than the benchmark. To understand this result we will look at only the phase A conductor of the branch leading from the regulator at the source node to its receiving node, branch RG1-632. This branch carries all source current to the rest of the feeder and the analysis of this phase conductor of this branch will be representative of the other phase branches of the feeder.

The calculated phase A current and conductor resistance for branch RG1-632 are

given in Table 6.11 for the benchmark, cooler, and warmer scenario cases. The calculation of losses is accomplished through the consideration of the power entering and leaving each branch (power in minus power out), but the line resistance and current can give an intuition as to the cause of the deviation in losses..

Table 6.11: Extreme cases comparison to benchmark results: branch RG1-632, phase A, 13-node feeder

	Line current (A)	Resistance (Ω/mile)
Benchmark	593.26	0.1859
Warmer	593.81	0.1930
Cooler	589.65	0.1456

It can be seen that in the cooler case, both the current and the line resistance decreased, and in the warmer case both increased, as compared to the benchmark solution. Most of the load on the feeder is constant power, and the current drawn by the constant power load will vary based on the node voltages, which vary based on conductor resistance, which vary based on line current, which in turn vary based on conductor temperature. As the resistance decreases with temperature, the voltage drop across the line decreases, causing downstream voltages to be incrementally higher than in the higher resistance case. This allows the line current to be less to meet the same constant power requirements of the load. This decreased line current then in turn pushes the conductor temperature even lower, which affects the voltage profile even further. This reciprocal relationship is the very reason we need a more complex analysis such as that described in this work in order to determine the effect that conductor temperature has on the power flow solution, including the calculation of branch losses.

The difference in losses for each branch in each extreme case, as compared to the benchmark solution, can be seen in Fig. 6.10. The losses shown are the sum of all

phase losses on a given branch, with the horizontal axis annotated as the branch receiving node. It can be noted that the largest variation in loss occurs on branches RG1-632 and 632-671, which correspond to the branches with the highest line current. Branch 671-692 is a normally-closed switch (lossless), and branch 633-634 is an inline transformer. The regulator on branch 650-RG1 is modeled as lossless (see section 3.6). It can be seen that, as indicated in Table 6.10, the benchmark solution and the warmer solution are relatively similar, with the warmer solution showing marginally higher calculated branch and total losses. The cooler case varies by a greater margin, especially for those highly loaded central branches.

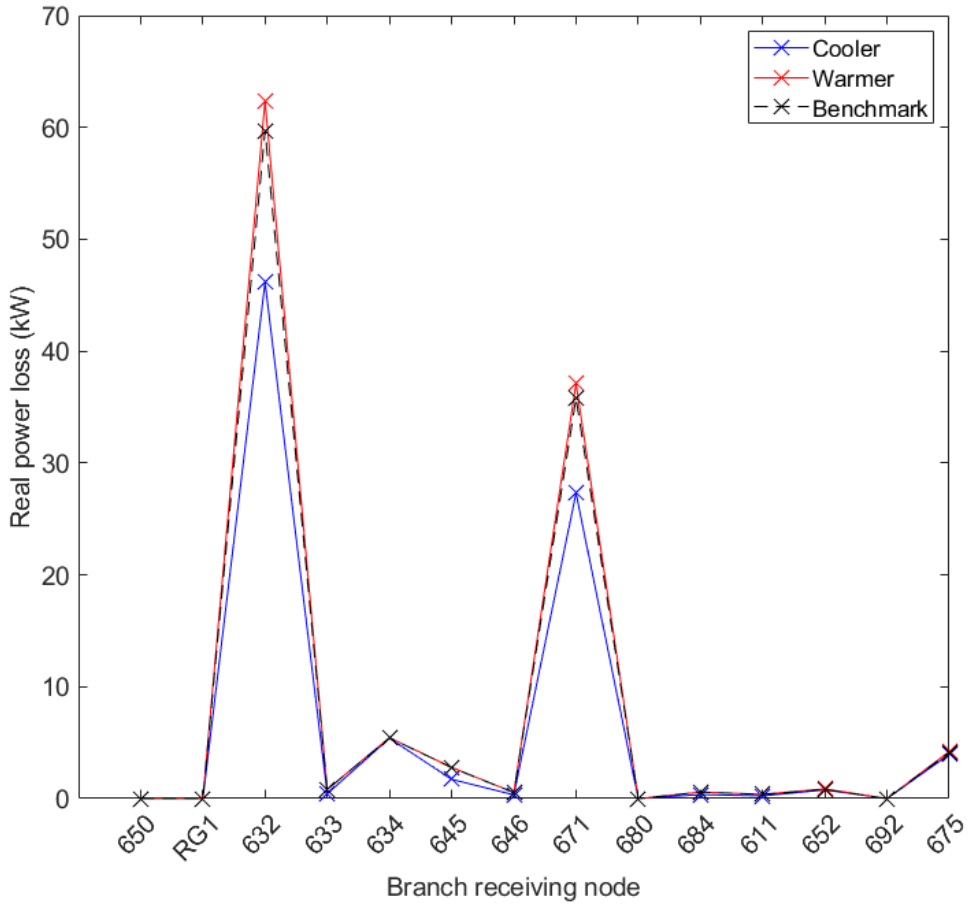

Figure 6.10: 13-node feeder: branch losses, cooler and warmer extreme conditions

The degree of voltage unbalance, as defined by Eq. 6.1, can also be compared

between the extreme cases and the benchmark. It can be noted from Fig. 6.11 that the voltage unbalance at each node increases in the warmer case and decreases in the cooler case, having a similar relationship as was demonstrated between real power loss and conductor temperature. The maximum unbalance for all cases occurs on the end node 675, and for the warmer, cooler, and benchmark scenarios is 5.09, 4.42, and 5.01% respectively. As the calculation of voltage unbalance is directly related to the maximum deviation of the node voltage magnitudes from the average node voltage, it is reasonable to state that as loss increases in the warmer case, the node voltages diverge more from the average, resulting in higher voltage unbalance at each node. The inverse is true of the cooler case.

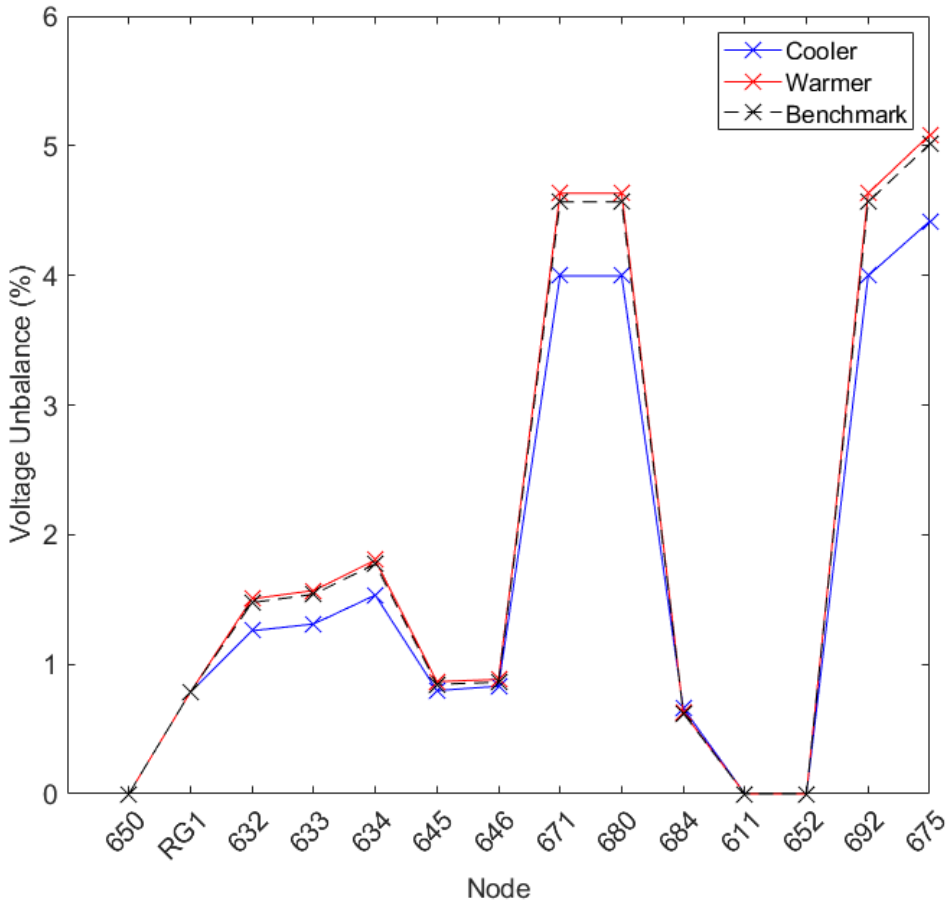

Figure 6.11: 13-node feeder: node voltage unbalance, cooler and warmer extreme conditions

The next section will use the complete data sets of section 6.3 in application of the temperature-dependent power flow to the 13-node test feeder in a steady-state time-series analysis.

6.4.2.2 Steady-State Time-Series: Year 2020

In this section the ambient air temperature, wind speed, and ambient soil temperature data of section 6.3, along with the solar heating implied by the corresponding time of day and day of the year, are used to perform a steady-state time-series power flow analysis of the 13-node test feeder. In this case study, the temperature dependent algorithm of section 5.3 is run at each of 8784 hourly time intervals of 2020 (2020 was a leap year) using the data corresponding to that time interval. Voltages, currents, conductor temperatures, losses, and voltage unbalance are all tracked over the course of the year to make an assessment of the impact of considering conductor temperature on the power flow solution, and the degree of variance that occurs over the course of a year considering historical weather and soil conditions. An important acknowledgement is that this type of steady-state time-series analysis has its limitations. While the electrical characteristics of the system (current, voltage) can change rapidly (approximated as a step change), the thermal characteristics of the system change more slowly, and cannot be as accurately represented without taking into account the gradual change that occurs between time steps (in both conductor temperature and weather conditions). However, it is the belief of the author that the following analysis provides interesting results, and can serve as a basis for incorporating transient thermal characteristics in the future.

Some insight in the results that follow in this section can be supported by looking at three representative branches of the 13-node test feeder: branches RG1-632 (overhead line, 556.5 kcmil ACSR phase conductor), 692-675 (underground line, 250 kcmil AA concentric neutral cable), and 684-652 (underground line, 1/0 AWG AA tape-shielded cable). The figures that follow will track the changes in conductor temperature,

conductor resistance, and line current for the phase A conductor of each branch.

Fig. 6.12 shows the calculated conductor temperature for the phase A conductor of each of the three branches over the course of the year in comparison to the constant conductor temperature of $50°C$ implicit in the benchmark power flow solution. The most obvious initial impression is that the conductor temperature of the overhead branch RG1-632 varies to a much greater degree than the underground branches. The exposure to more rapidly changing weather conditions, as compared to the comparatively stable soil temperature, causes the overhead line section to display much greater variability in conductor temperature.

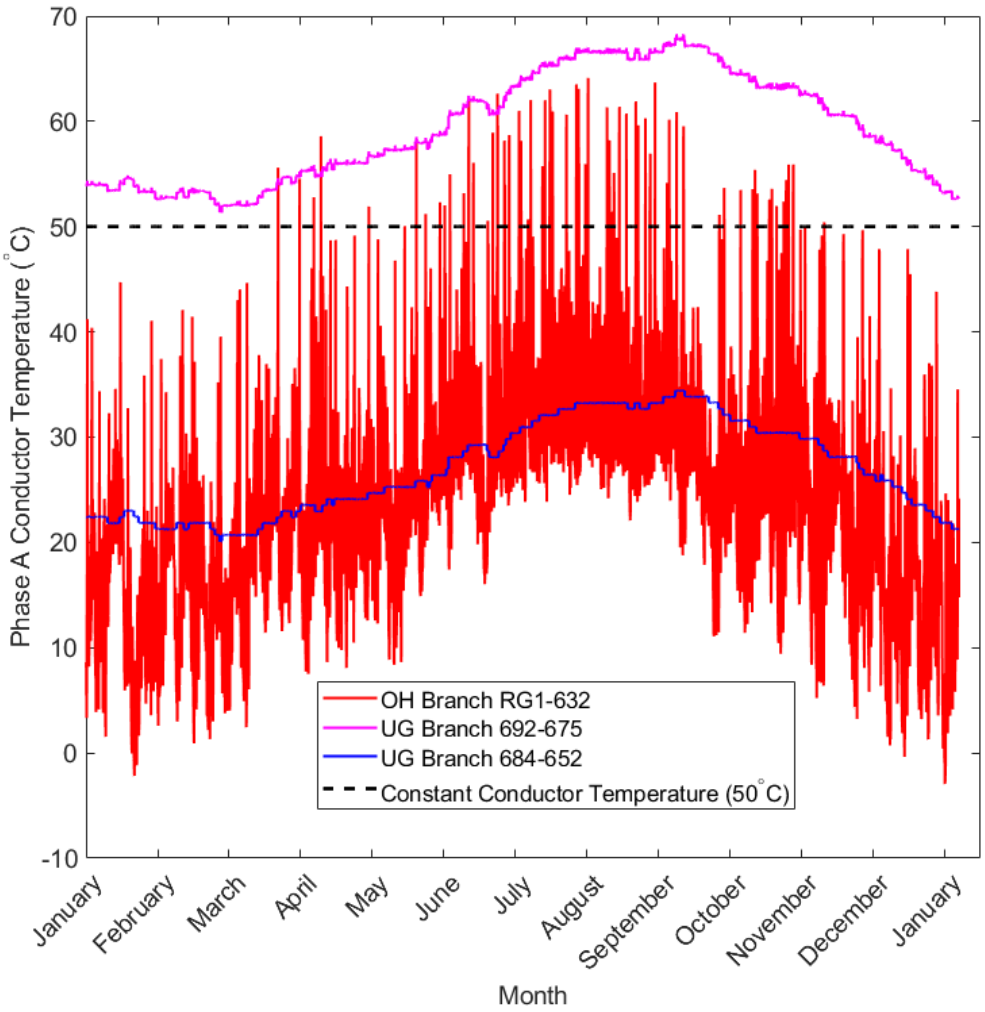

Figure 6.12: Representative branch conductor temperature variation, 2020

Secondly, it can be noted that for the entirety of the year, branch 692-675 has a consistently higher conductor temperature, and branch 684-652 a lower conductor temperature, than that assumed in the benchmark case. This is the result of having higher and lower branch current respectively than that which would result in the $50°C$ assumed in the benchmark case. The overhead branch RG1-632 is lower than $50°C \approx 99\%$ of the time, only infrequently reaching or exceeding this assumed value. Finally, the underground section temperatures are seen to peak around September, when the soil temperature peaks, and the overhead section peaks somewhat earlier during the hottest days of the year.

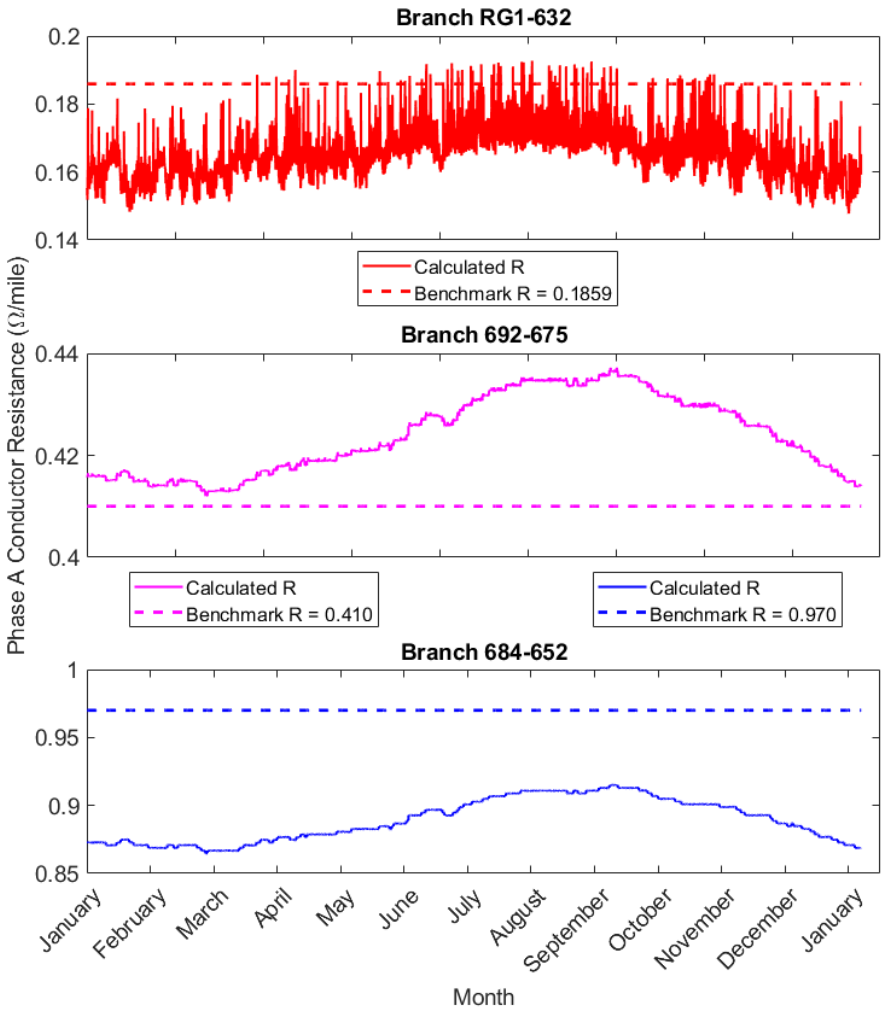

Figure 6.13: Representative branch conductor resistance variation, 2020

The relationship between conductor temperature and resistance was modeled in Chapter 4 as being piece-wise linear, with a breakpoint at $50°C$. Therefore, the branch resistances of the phase A conductors shown in Fig. 6.13 follow from the conductor temperature variation shown in Fig. 6.12. For each of the three branches, we can note that as with conductor temperature, the resistance of branch 692-675 is consistently higher than the assumed benchmark value, and branch 684-652 is consistently lower. Again, overhead branch RG1-632 has a lower-than-nominal resistance $\approx 99\%$ of the year. We can also note the more rapidly varying resistance in the overhead branch following from the more rapidly varying conductor temperature.

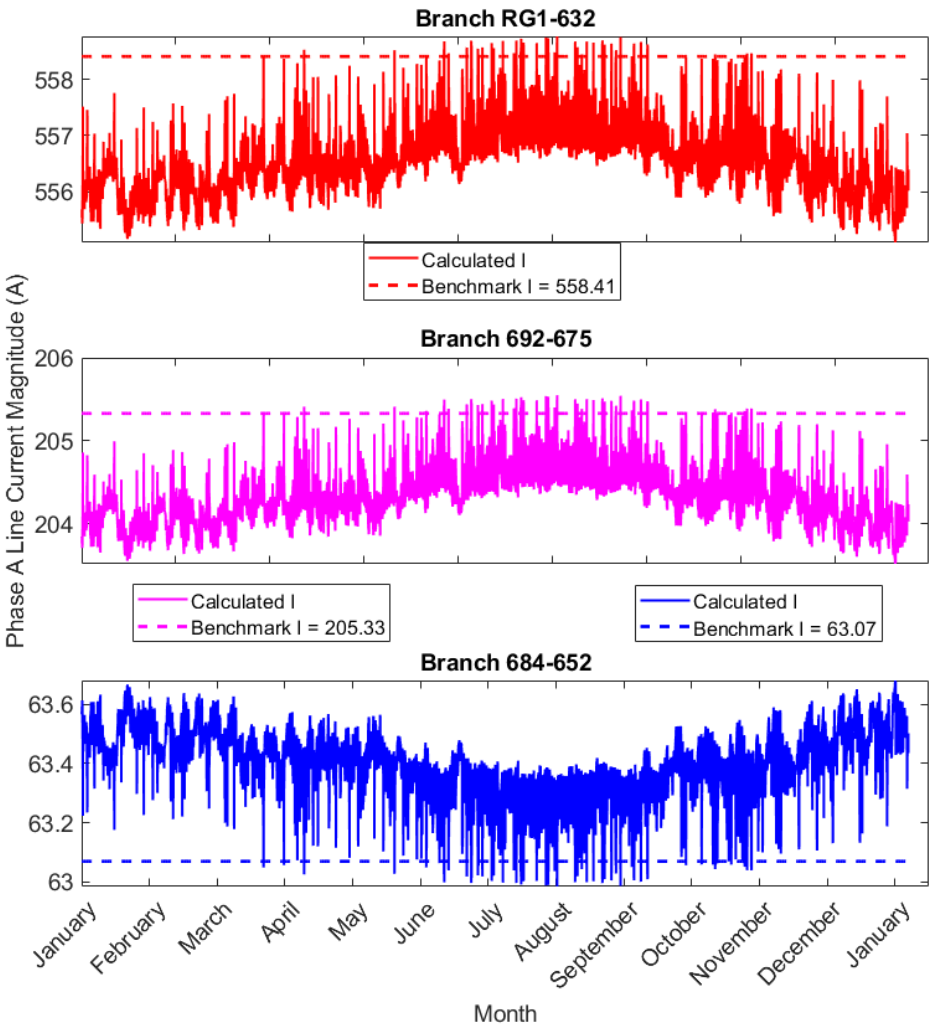

Figure 6.14: Representative branch line current variation, 2020

Most interestingly, Fig. 6.14 shows the variation in the line current in the phase A conductor for each branch over the course of the year. It was previously established that for a constant power load, as conductor temperature and thus resistance increase, node voltages decrease, and current must increase. This is precisely what is shown in Fig. 6.14 for branches RG1-632 and 692-675. However, the line current for branch 684-652 has an inverse relationship to the current on the other two branches. Branch 692-675 serves an end node with a constant power load, and branch RG1-632 is the main branch leading from the regulator at the source node that carries all current for the feeder, which is predominantly composed of constant power loads. Therefore, this logic holds true for these branch currents. In contrast, branch 684-652 serves an end node with a constant impedance load, so as the voltages decrease during the summer months (hotter lines, higher resistance, larger voltage drops, lower node voltages), the constant impedance load current for end node 652 decreases. Because the branch current on branch 684-652 is approximately equal to the end node load current (neglecting shunt impedance contributions), the decreased branch current during the summer months is observed for this branch.

It has been established that the relationship between line current and conductor temperature is nonlinear (Chapter 4), and that the relationship between conductor temperature and line resistance is modeled in this work as piece-wise linear (Eq. 4.9). For a single-phase line, the relationship between real power loss, resistance, and line current is also nonlinear, and becomes perhaps even more nonlinear when considering multi-phase line segments, where loss is calculated as the difference in powers at the sending and receiving ends of the line segment. It is interesting to consider then what occurs in a case such as branch 684-652 where current decreases as resistance increases. With reference to Figs. 6.12 and 6.13, it can be observed in Fig. 6.15 that the trend of losses is to increase and decrease with conductor temperature and line resistance throughout the year on all three branches, irrespective of the behavior of

the current magnitude.

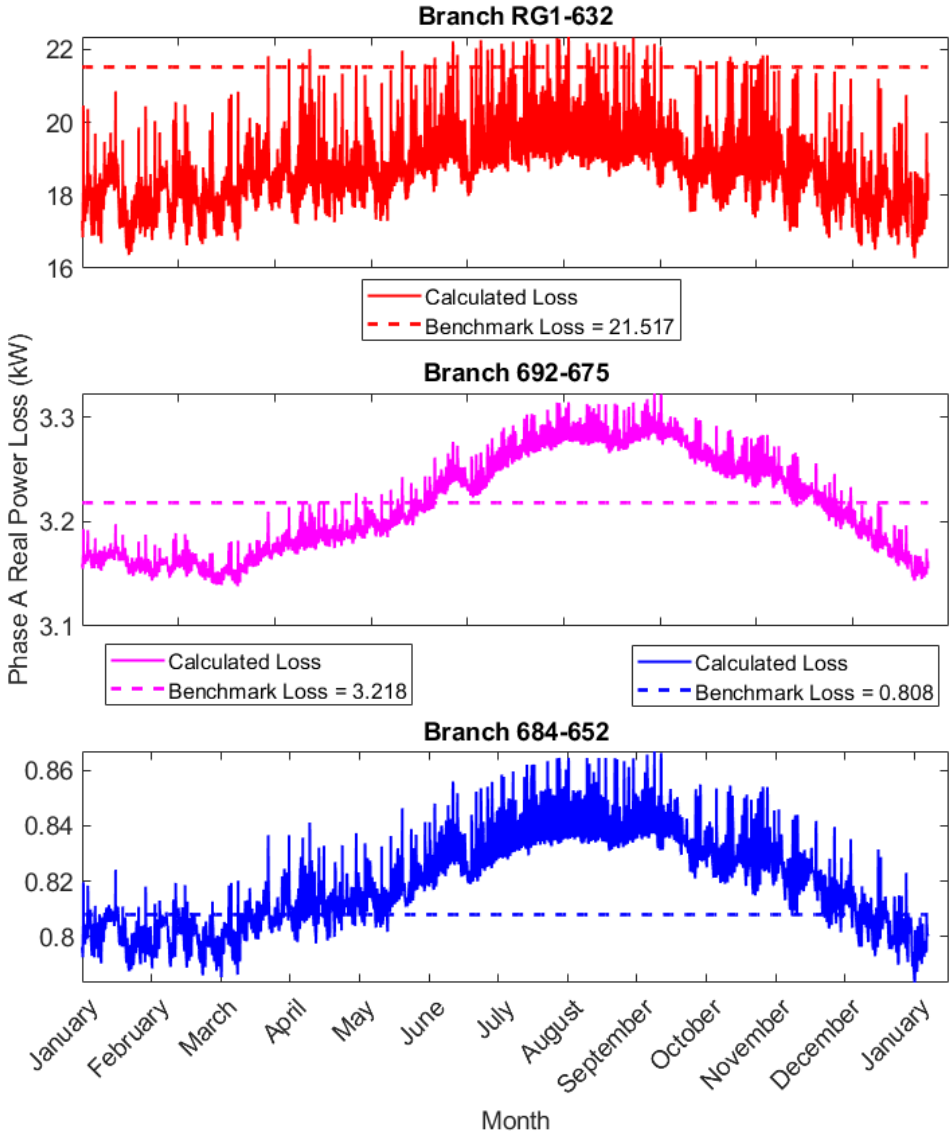

Figure 6.15: Representative branch line loss variation, 2020

Importantly, the steady-state time-series analysis shown in Figs. 6.12-6.15 can only be achieved using the proposed temperature-dependent power flow algorithm and *not* with a conventional power flow algorithm, which doesn't allow the explicit calculation of conductor temperature, and corresponding variation of resistance and current.

While the variation in node voltages is sufficient to play a role in marginally affect-

ing the line current, it was noted in the extreme test case of the last section that the consideration of conductor temperature in general made only a small impact on the calculation of node voltage magnitudes.

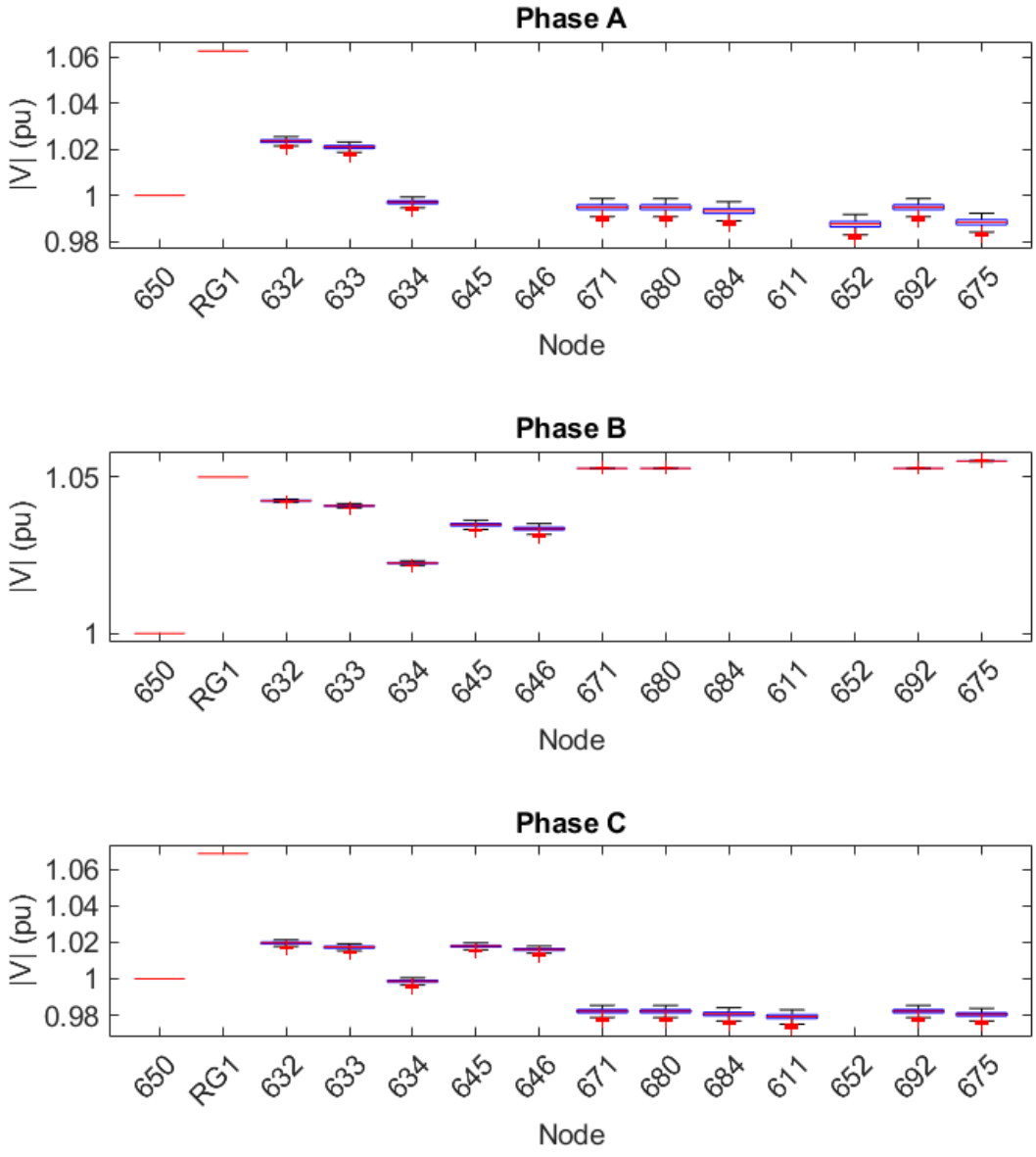

Figure 6.16: 13-node feeder: node voltage magnitude box and whiskers

This assessment is reinforced by the box-and-whiskers plot of Fig. 6.16 where the

summary statistics for each phase node over the course of the year can be viewed. Fig. 6.16 indicates that the voltage profile is very stable over the course of the year, with the maximum and minimum values varying by as little as approximately 0.01 pu towards the ends of the feeder, and being even more consistent closer to the source node. The source node is considered a fixed voltage source and does not change, and the regulator, while allowed to shift tap settings in the algorithm, has also remained fixed over the course of the year, indicating that the tap settings have not been required to change to regulate the voltage within the regulator set points. It can also be noted that although the variation in voltage is limited, it is more pronounced on phases A and C, where the feeder is most heavily loaded. This is reasonable as the voltage drop variation is exacerbated by the higher current present on these phases.

Fig. 6.17 shows the maximum node voltage magnitude deviation, calculated as the maximum value of the calculated solution minus the benchmark solution, over the course of the year. In the extreme scenario case, it was noted that warmer conditions, such as those found during peak summer months, brought the conductor temperature closer to and just beyond the assumed $50°C$ conductor temperature of the benchmark solution. It can be noted in Fig. 6.17 that the deviation approaches zero towards summer months, when the calculated conductor temperatures are closer to the $50°C$ that is assumed by the benchmark solution, and the deviation increases in general in the cooler months. During winter, spring, and fall, the deviation is most generally positive (higher voltage magnitudes than the benchmark), and in the summer there are some cases where the deviation is negative (lower voltage magnitudes than the benchmark). The extreme points that are much lower than surrounding time steps correspond to the incidence of still air (zero wind speed). Fig. 6.17 also indicates that approximately 99% of the time, the voltage magnitude at the node with the highest deviation from the benchmark is greater than that of the benchmark solution, albeit by a small margin.

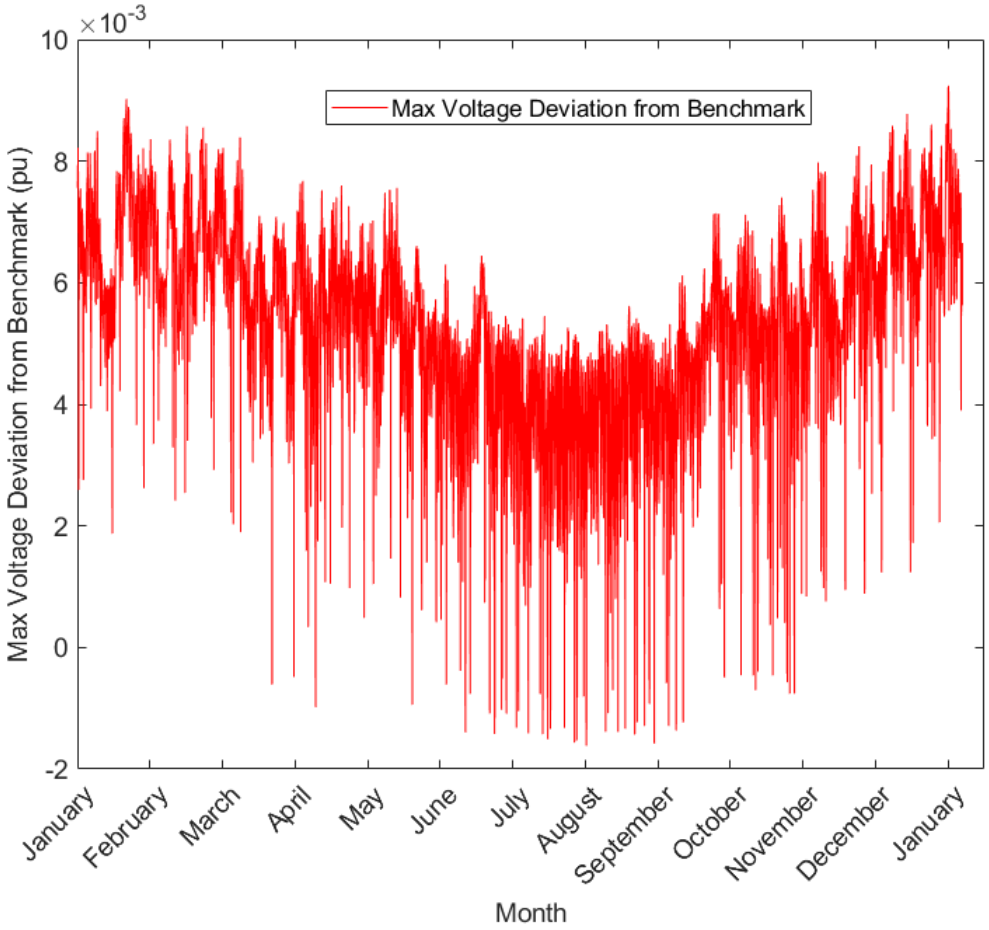

Figure 6.17: 13-node feeder: maximum voltage deviation from benchmark

Although the relationships between ambient conditions, voltage deviation from the benchmark, and real power loss are not linear in general, Fig. 6.18 attempts to fit any potential linearity which may exist between the weather parameters and the system variables. The figure shows the variable correlation, Pearson's correlation coefficient, and the parameter and variable histograms.

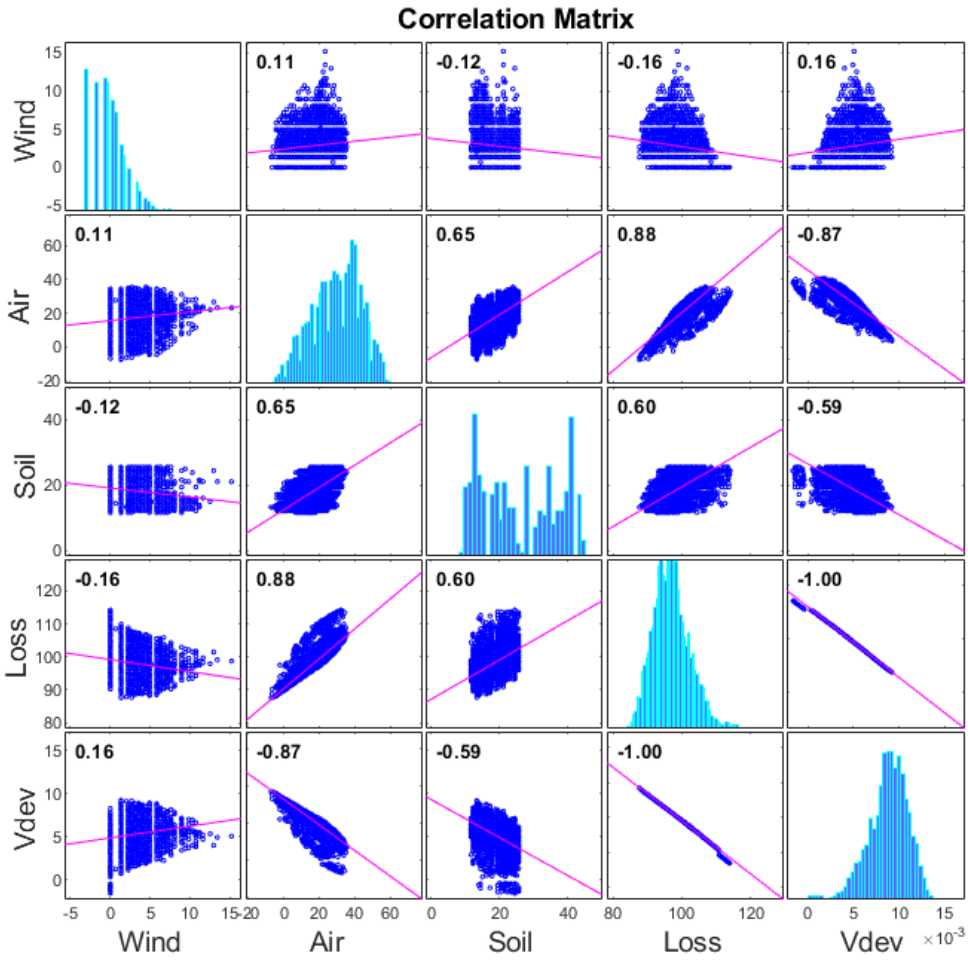

Figure 6.18: 13-node feeder: weather and soil data correlation to loss and voltage deviation

The ambient air and soil temperature are positively correlated with total loss and negatively correlated with voltage deviation. This seems reasonable as it is expected that voltage deviation from the benchmark decreases and losses increase as increasing ambient temperatures cause the conductor temperatures to approach the $50°C$ implicit in the benchmark solution. The relationship between air temperature and voltage deviation and total loss are particularly strong, perhaps because the 13-node test feeder is predominantly composed of overhead lines. The relationship between wind speed, total loss, and voltage deviation is a bit muddier, and it is suspected

that significant nonlinearity is obscuring the relationship that is expected, that is that increasing wind speed cools the lines, decreasing loss and increasing voltage deviation from the benchmark. It can also be noted the perfect negative linear correlation between maximum voltage deviation and loss. The voltage deviation becomes more positive (higher than the benchmark) as the voltage drops on the line segments decrease, which result in lower losses.

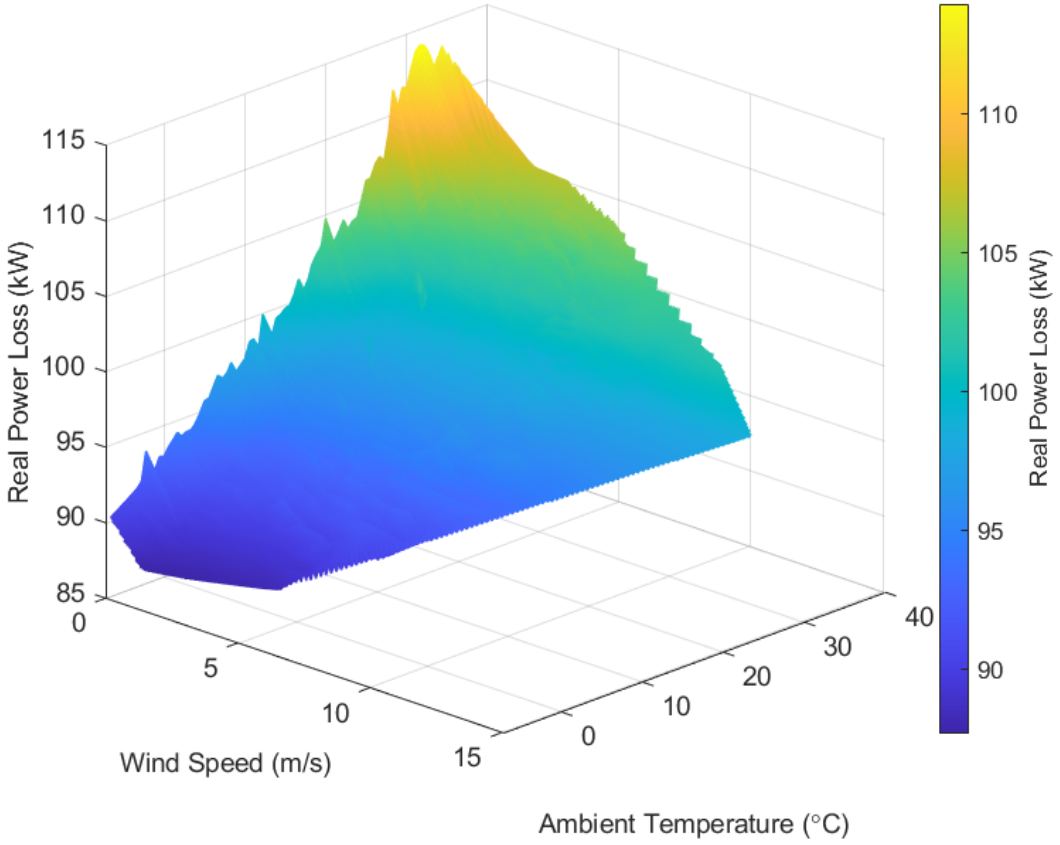

Figure 6.19: 13-node feeder: total loss, ambient air temperature and wind speed

The relationship between total losses, ambient air temperature, and wind speed can be further visualized in Fig. 6.19, developed from the results of the steady-state time-series analysis. The total loss is seen to increase towards higher ambient air temperature and lower wind speed, and decrease in the opposite direction. Since the test feeder is primarily composed of overhead lines, wind speed and ambient air

temperature play a greater role in the variation of losses than ambient soil temperature. However, as ambient soil temperature is positively correlated with ambient air temperature (Fig. 6.18), a similar relationship could be developed for the ambient soil temperature as well.

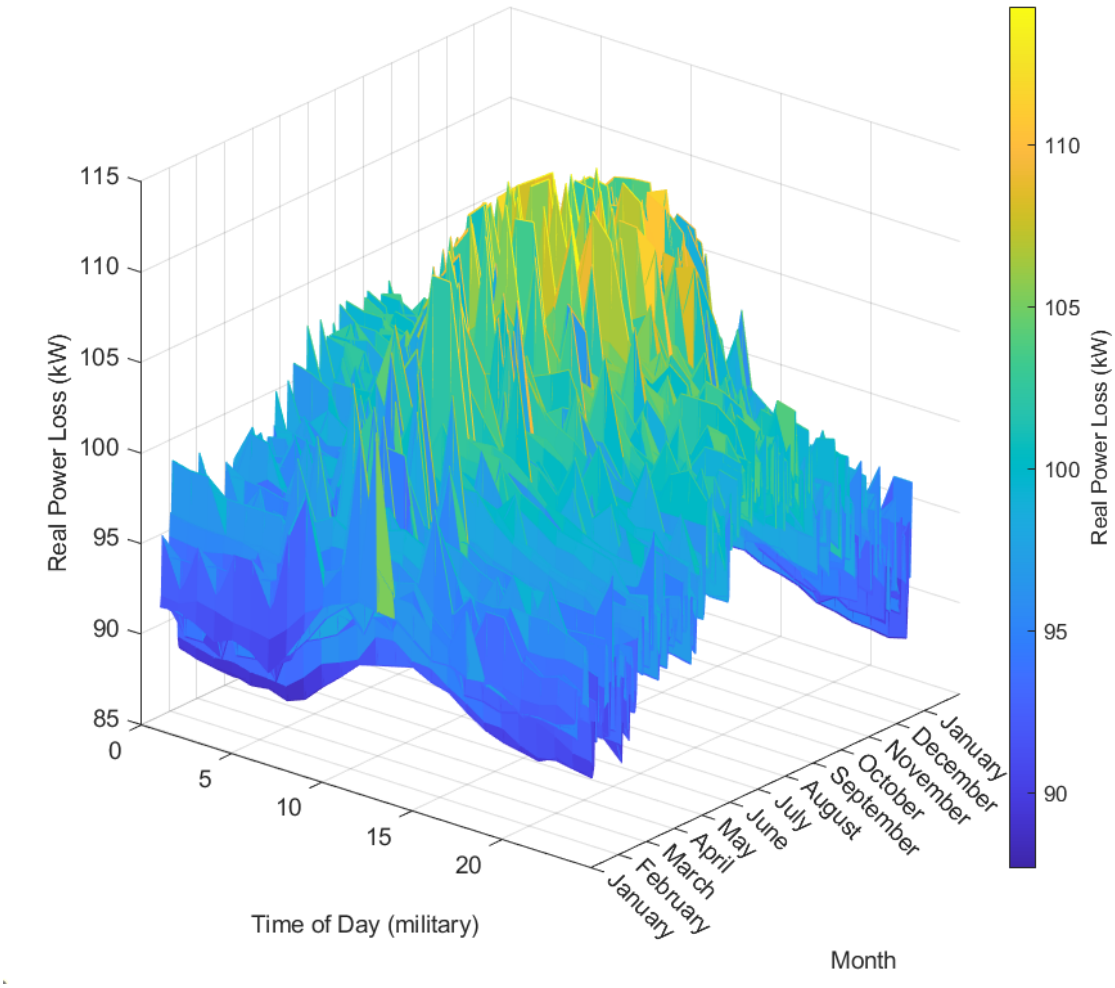

Figure 6.20: 13-node feeder: total loss, time of day and year

The time of day and year also play a crucial role in the calculation of the conductor temperature for overhead lines, as was discussed in section 4.2. The solar heating of the line increases in the warmer months of the year and during midday, contributing to higher overhead conductor temperature and corresponding losses. This relationship can be viewed in Fig. 6.20. The total losses can be seen to peak during the warmer

summer months, and during midday year round. The losses are shown to be reduced overnight, and the lack of solar heating during this time is one factor that causes this effect (along with lower nighttime air temperatures and reduced wind speed).

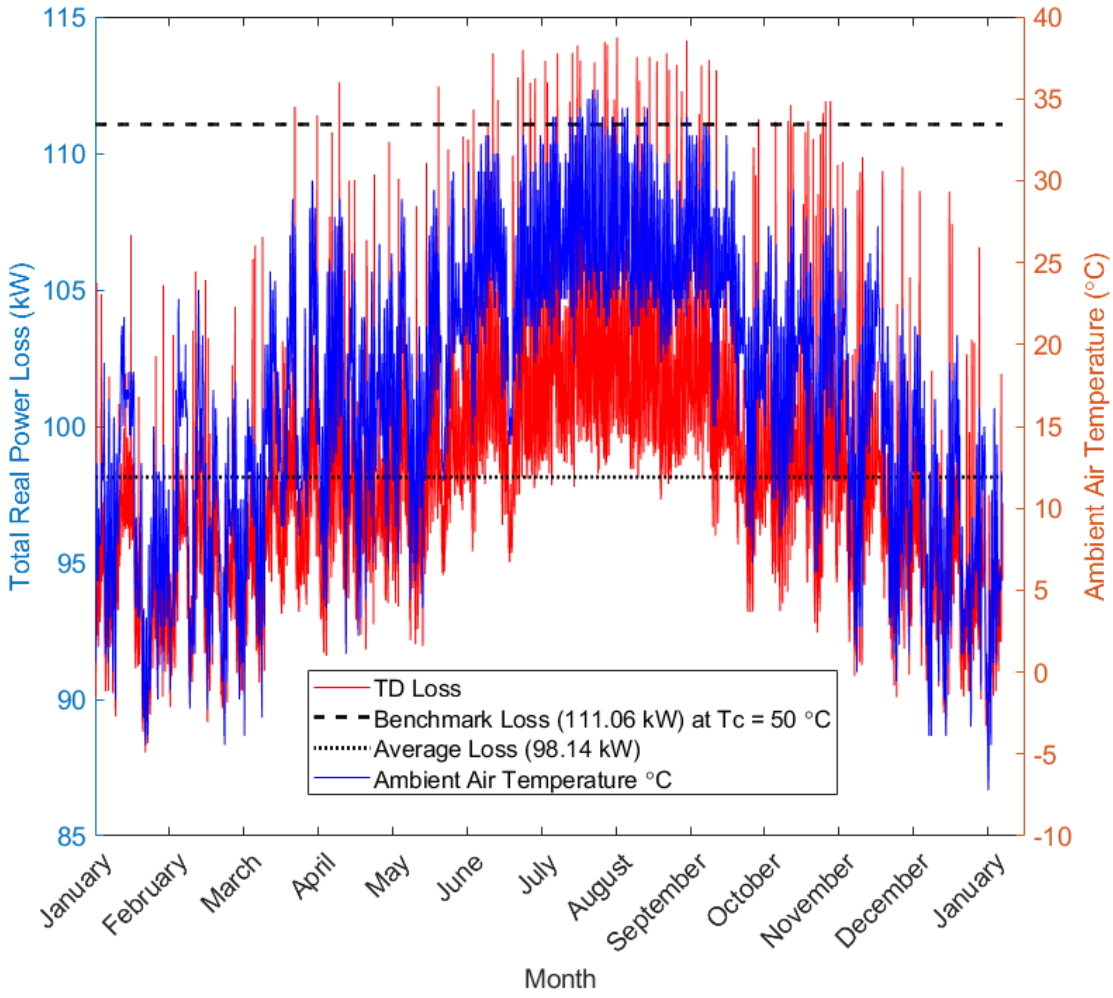

Figure 6.21: 13-node feeder: total loss and ambient temperature, 2020

The correlation between total losses and ambient air temperature can again be seen in Fig. 6.21. As indicated in the previous Figs. 6.18 and 6.19, the total losses increase and decrease with air temperature over the course of the year. The benchmark constant loss over the year, not considering the variability in conductor temperature, is shown as the black dashed line. It can be seen that only infrequently does the calculated total loss reach or exceed the benchmark loss ($\approx 1\%$ of the time). Much

more frequently, the calculated losses are less than the benchmark value ($\approx$ 99% of the time). The average loss, shown as the black dotted line, is 11.6% less than the benchmark value.

With reference to Fig. 6.21, Table 6.12 gives the incidence of highest and lowest loss over the course of the year along with the accompanying weather parameters and time of occurrence.

Table 6.12: 13-node feeder: highest and lowest loss occurrence, 2020

	Date	Total loss (kW)	Air temp ($°C$)	Soil temp ($°C$)	Wind speed (m/s)
Highest	7/29, 12pm	114.3	32.22	24.44	0
Lowest	12/26, 4am	87.7	-7.22	13.33	1.34

In comparing the maximum and minimum losses obtained, and the weather parameters associated with these losses, to the extreme condition test case in the previous section (reference Tables 6.8 and 6.10), it can be noted that the air and soil temperatures, losses, and dates are comparable to the highest and lowest loss occurrences shown in Table 6.12. The highest and lowest losses obtained in the extreme condition test case were marginally higher and lower than those shown in Table 6.12, and the air and soil temperatures marginally higher or lower respectively. It can also be noted that at such a low temperature as that seen in the lowest loss case of Table 6.12, only a marginal decrease in loss was seen by a substantial increase in wind speed, as was considered in the extreme low-loss test case. This characteristic was noted in Fig. 6.19, that the variation of wind speed has a greatly decreased effect at lower air temperatures in terms of impacting the loss.

The conductor temperature heatmaps for the highest and lowest loss cases of Table 6.12 can be seen in Fig. 6.22. Again, in comparing to the extreme test case heatmaps of Fig. 6.8, the conductor temperatures are comparable, with the extreme

test case conductor temperatures being moderately different in the range of 2 to 4°C, approximately the difference in the ambient air and soil temperatures considered.

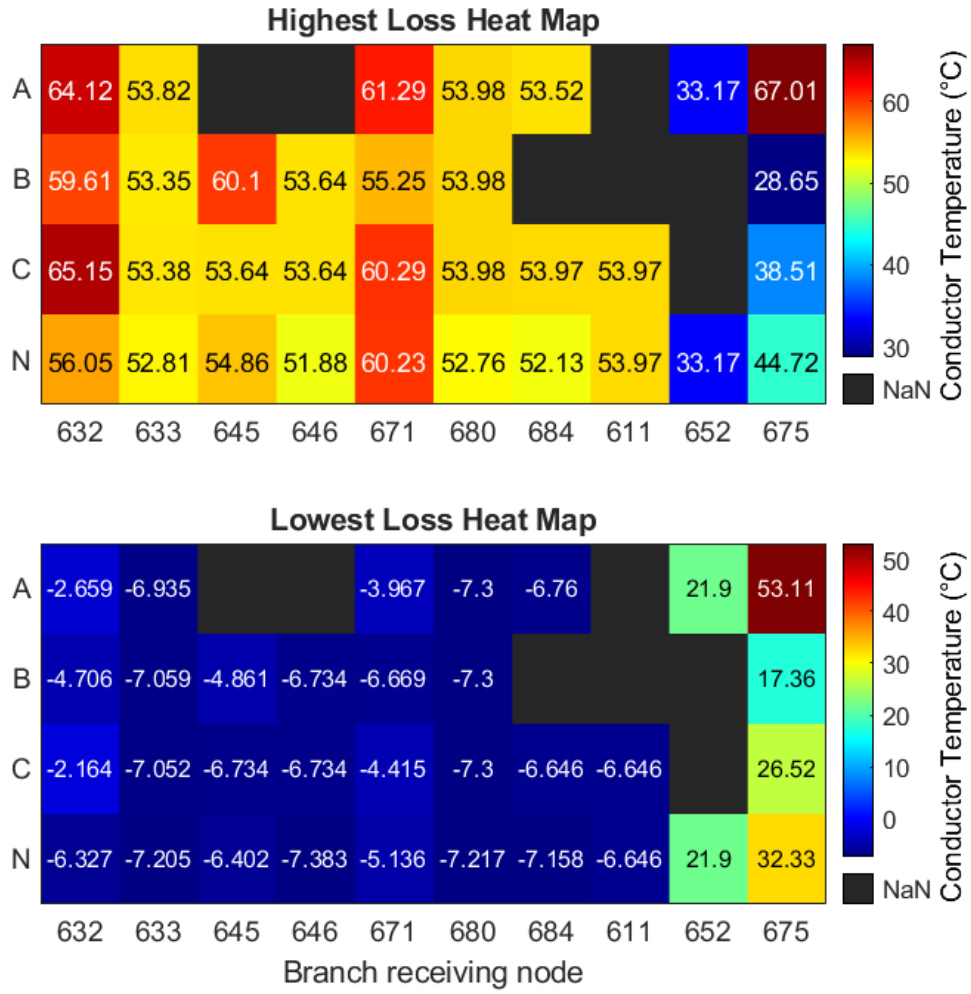

Figure 6.22: 13-node feeder: branch heatmap, highest/lowest loss cases, 2020

In the final examination of the variation of losses over the course of the year, Fig. 6.23 shows the variation in branch losses. As in Fig. 6.10, it can be noted that the largest losses occur on branches RG1-632 and 632-671, the longest and highest current branches of the feeder.

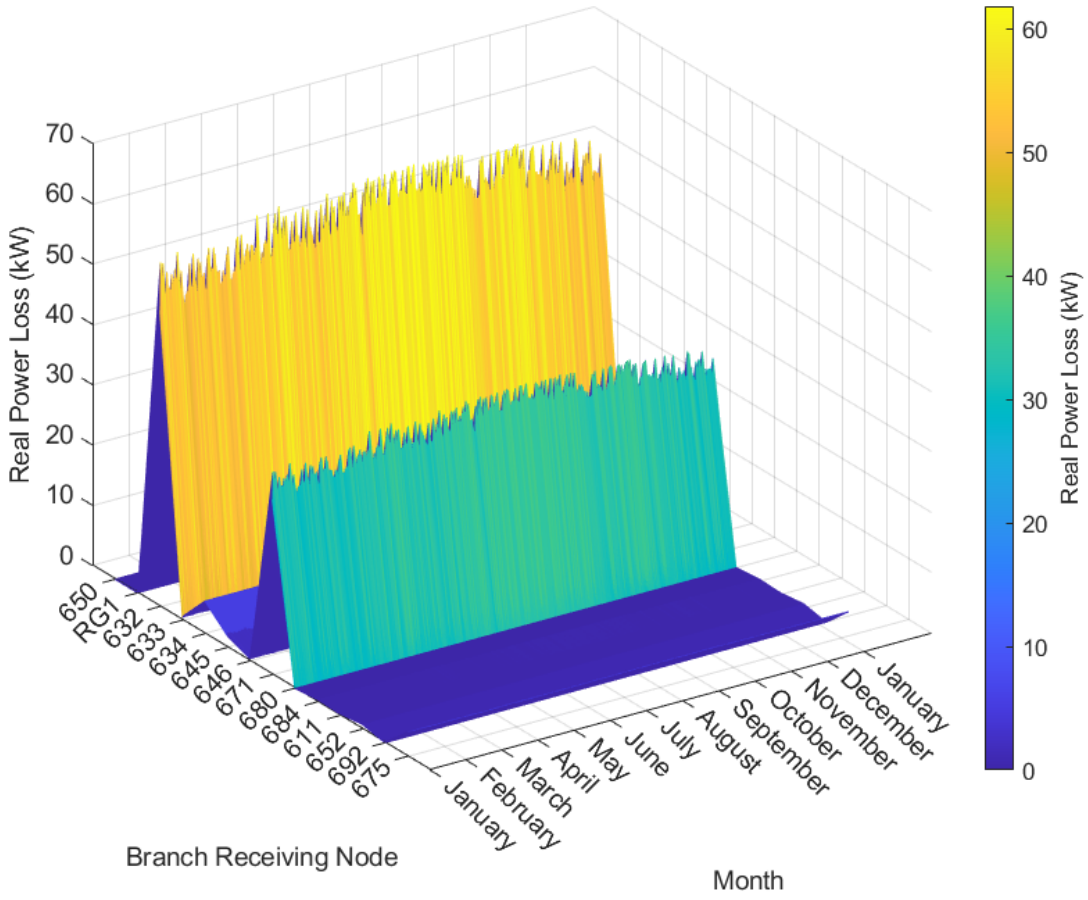

Figure 6.23: 13-node feeder: branch losses, 2020

Fig. 6.24 shows the voltage unbalance at each node as calculated by Eq. 6.1 over the course of the year. As in Fig. 6.11, the highest degree of unbalance occurs on the end node 675. The maximum and minimum voltage unbalance occurring at the most unbalanced node (node 675), and the time and date of occurrence, can be seen in Table 6.13. Referencing Table 6.12, it is no surprise that the incidence of highest and lowest total real power loss are coincident with the highest and lowest degree of voltage unbalance.

Table 6.13: 13-node feeder: highest and lowest voltage unbalance occurrence, 2020

	Date	Voltage unbalance (%)	Air temp ($°C$)	Soil temp ($°C$)	Wind speed (m/s)
Highest	7/29, 12pm	5.07	32.22	24.44	0
Lowest	12/26, 4am	4.44	-7.22	13.33	1.34

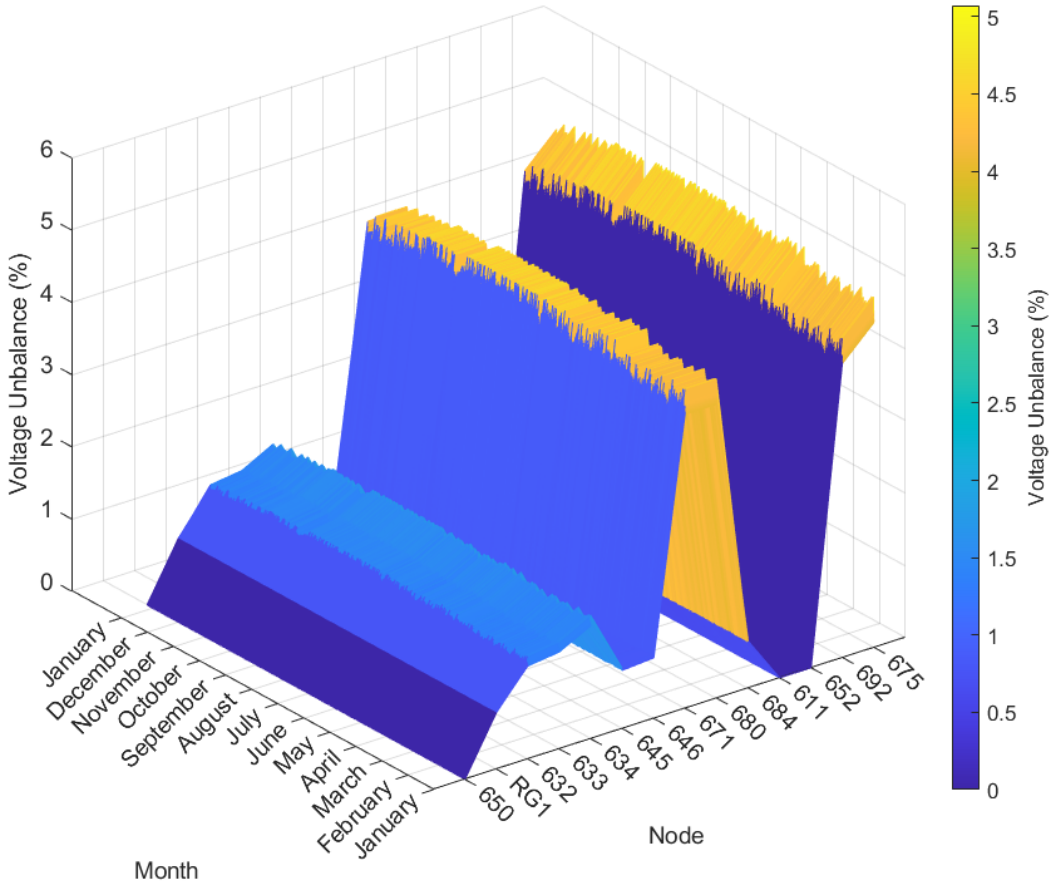

Figure 6.24: 13-node feeder: node voltage unbalance, 2020

The voltage unbalance varies over the year, perfectly correlated with total real power loss, as seen in Fig. 6.25. As real power loss has been shown to be correlated with conductor temperature, it is reasonable to assert that increased conductor temperatures, occurring generally during the warmer months of the year, exacerbate

voltage unbalance due to magnified differences in voltage drops across the phases of a line section.

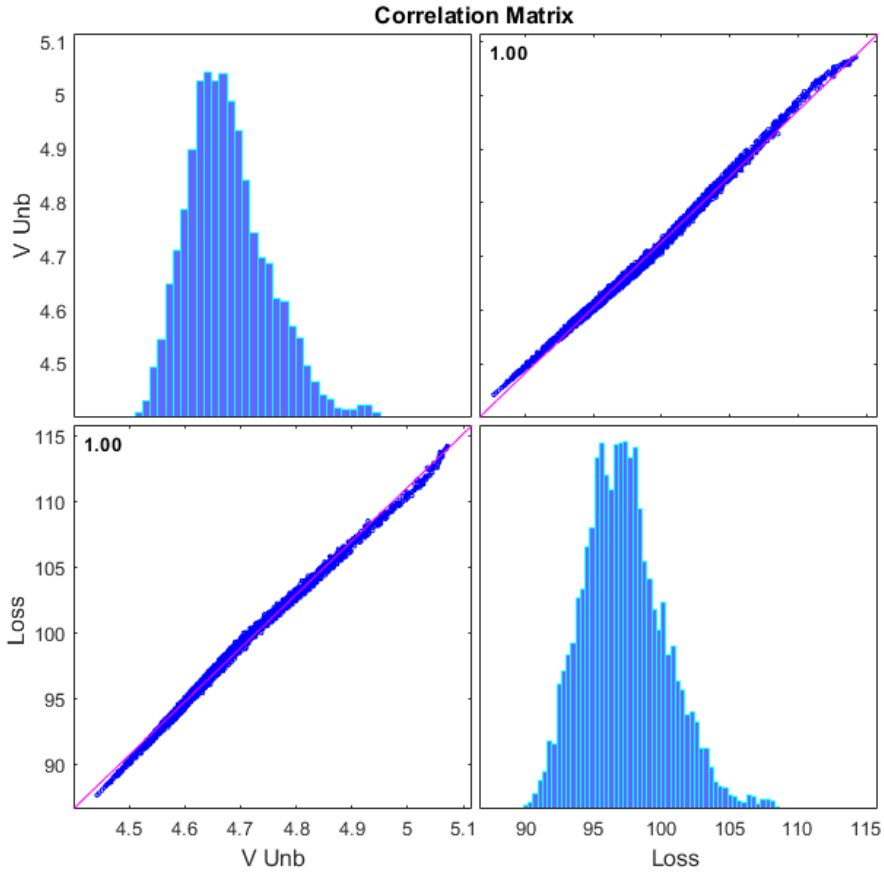

Figure 6.25: 13-node feeder: node voltage unbalance and total loss correlation

6.5 123-Node Test Feeder

The IEEE 123-node test feeder can be viewed in Fig. 6.26. As in the 13-node test feeder, the circuit contains a combination of one-, two-, and three-phase line sections and one-, two-, and three-phase constant current, impedance, and power loads configured in both delta and wye. Capacitors are located at four individual nodes, and there is one voltage regulator and one transformer located at the substation (source) node, three voltage regulators located at additional branches in the system, and a second transformer located between nodes 61 and 610. All lines are composed of

overhead ACSR conductors except for the five branches between nodes 60 and 66, which are underground concentric neutral cable. All data required for the conventional power flow analysis can be found at the IEEE PES AMPS DSAS Working Group website [62].

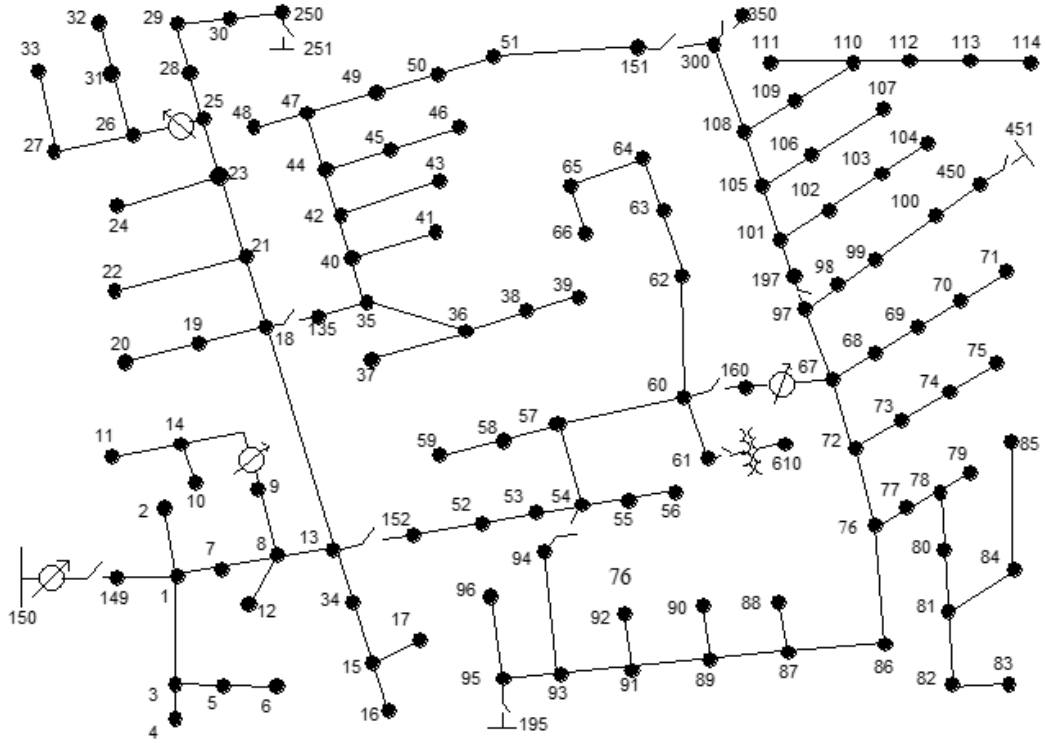

Figure 6.26: IEEE 123-node test feeder

The section that follows will compare the results of the algorithm presented in section 5.2 to the benchmark results as given in [62].

6.5.1 Conventional Algorithm Comparison to Benchmark

This section is formulated exactly as the 13-node test case benchmark comparison section 6.4.1 and will present the results of the application of the conventional (non-temperature-dependent) three-phase backward-forward sweep algorithm (section 5.2) to the IEEE PES 123-node test feeder [62]. These results assume, as in the original test feeder data, that all conductor resistances correspond to a uniform conductor temperature of $50°C$ across the entirety of the feeder. The results of the section 5.2

algorithm are compared to the benchmark solution as given by [62] to confirm the accuracy of the algorithm before modifications are made to introduce temperature-dependency, as discussed in section 5.3.

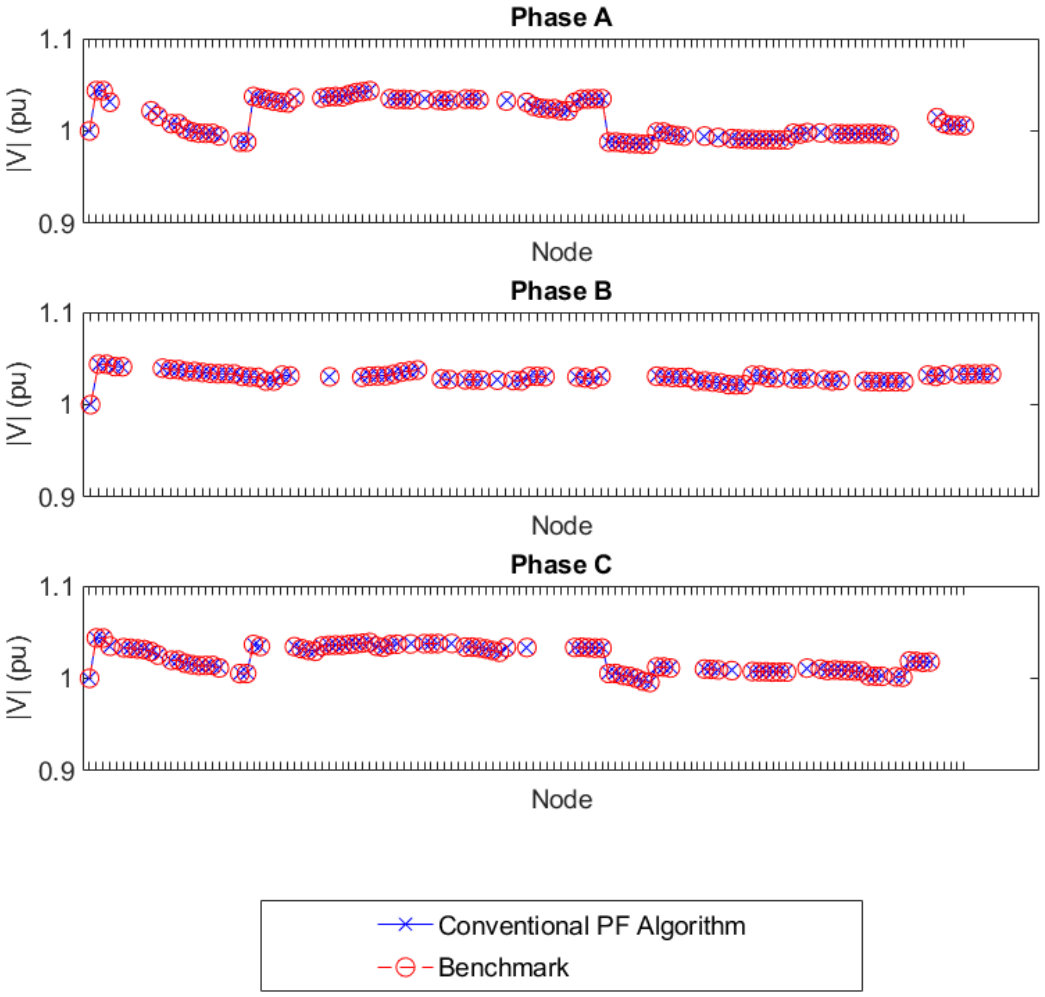

Figure 6.27: IEEE 123-node test feeder voltage profile

Fig. 6.27 shows the benchmark voltage profile as given in [62] in comparison to the results of the conventional power flow algorithm of section 5.2 (in this case, including node labels on the axis ticks was prohibitive), and Table 6.14 gives the

average absolute error for each phase in the calculation of the voltage as well as the maximum absolute voltage error with respect to the comparison between the benchmark results and the section 5.2 algorithm. As in the 13-node benchmark comparison, the voltages as calculated by the section 5.2 algorithm are noted to be in very close agreement to those of the benchmark.

Table 6.14: Comparison to benchmark results: voltage error, 123-node feeder

Average Absolute Error			
Phase A (pu)	Phase B (pu)	Phase C (pu)	Maximum Error (pu)
$2.44 \cdot 10^{-4}$	$1.09 \cdot 10^{-4}$	$1.32 \cdot 10^{-4}$	$6.13 \cdot 10^{-4}$

Table 6.15 gives the comparison of the real power loss calculated by the section 5.2 algorithm to the benchmark results. The error in calculated total real power loss between the section 5.2 algorithm and the benchmark is approximately 29 watts, or 0.03%.

Table 6.15: Comparison to benchmark results: real power loss, 123-node feeder

	Phase A (kW)	Phase B (kW)	Phase C (kW)	Total (kW)
Benchmark	50.540	10.134	34.937	95.611
Conventional PF	50.487	10.162	34.932	95.582
Error	0.053	-0.028	0.005	0.029

The degree of voltage unbalance at each node is calculated using the National Electrical Manufacturers Association (NEMA) definition (Eq. 6.1) as before, and the maximum voltage unbalance occurs at the end node 66, and is calculated for the section 5.2 algorithm and the benchmark as 2.06%.

6.5.2 Temperature-Dependent Algorithm Results

The following sections will demonstrate the application of the proposed temperature-dependent three-phase power flow algorithm presented in section 5.3 to the 123-node

test feeder. The first application in section 6.5.2.1 will assume two 'extreme' scenarios, a best- and worst-case for cooling of the lines. The second application in section 6.5.2.2 will use the complete data sets of section 6.3 in a steady-state time-series analysis.

6.5.2.1 Extreme Scenarios

This section will demonstrate the application of the temperature-dependent three-phase power flow algorithm to the 123-node test feeder in the same manner as in the extreme condition 13-node case study in section 6.4.2.1, and the extreme range of conditions, termed 'warmer' and 'cooler', can be viewed in Table 6.8. It was noted in the 13-node case study that the passive response of the feeder to increased conductor temperature, corresponding to the warmer set of conditions, was uniformly higher branch losses, lower voltage magnitudes, and greater degree of voltage unbalance as compared to the benchmark and the cooler condition case. It was also noted that the voltage regulator tap settings in the 13-node feeder case study, while allowed to change in the algorithm if system conditions required, remained the same for both cooler and warmer conditions. This is not the case for the 123-node feeder, and the examination of the variation in the tap settings is necessary to interpret the results.

The tap settings for the three-phase regulator at the source node (RG1), the single-phase regulator between nodes 9 and 14 (RG2), the two-phase regulator between nodes 25 and 26 (RG3), and the three-phase regulator between nodes 160 and 67 (RG4) can be viewed in Table 6.16 for both the warmer, cooler, and benchmark cases.

Table 6.16: Regulator tap settings, benchmark and cooler and warmer extreme conditions, 123-node feeder

Regulator	RG1			RG2	RG3		RG4		
Tap	A	B	C	A	A	C	A	B	C
Cooler	7	7	7	-2	0	-2	7	0	4
Warmer	7	7	7	-1	1	-1	8	1	5
Benchmark	7	7	7	-1	0	-1	8	1	5

The tap settings are a function of the regulator set points (bandwidth and voltage level), the voltage at the regulator in the unset position (in the power flow solution prior to setting the regulator taps, see algorithm in section 5.2), and the voltage simulated in the compensator circuit. The voltage simulated in the compensator circuit is dependent on the compensator settings, the current through the regulator, and the ratings of the current and potential transformers in the compensator circuit. This simulated voltage is designed to mimic the voltage at the load center that requires regulation downstream from the regulator. The regulator is capable of modifying the magnitude of the voltage on its secondary side by increments of 0.00625 pu, or 0.75 volts on a 120 volt base. As the voltage simulated in the compensator circuit, and presumably the voltage in the actual load center, decreases, the tap setting increases to support, or regulate, the load center voltage to remain within the regulator set points. Refer to section 3.6 and [27] for more details on the modeling of the regulators utilized in this study.

It can be noted that the primary regulator at the source node, RG1, has tap settings that do not change from the benchmark solution for either the warmer or cooler condition cases. It is important to note that this regulator has a "ganged" arrangement, where only phase A is monitored, and phase B and C taps are set to the phase A setting. The other regulators do change based on the conductor

temperature, however. The settings for RG2, RG3, and RG4 indicate that the cooler condition case requires less voltage support than the warmer and benchmark cases. The warmer case tap settings are the same as the benchmark case, except for phase A of RG3, indicating that the load center requires more voltage support on this phase during these conditions. The changing of the taps due to the change in conductor temperature adds an active element to the passive response of the system, and this behavior will be reflected in all the results that follow in this and the next section.

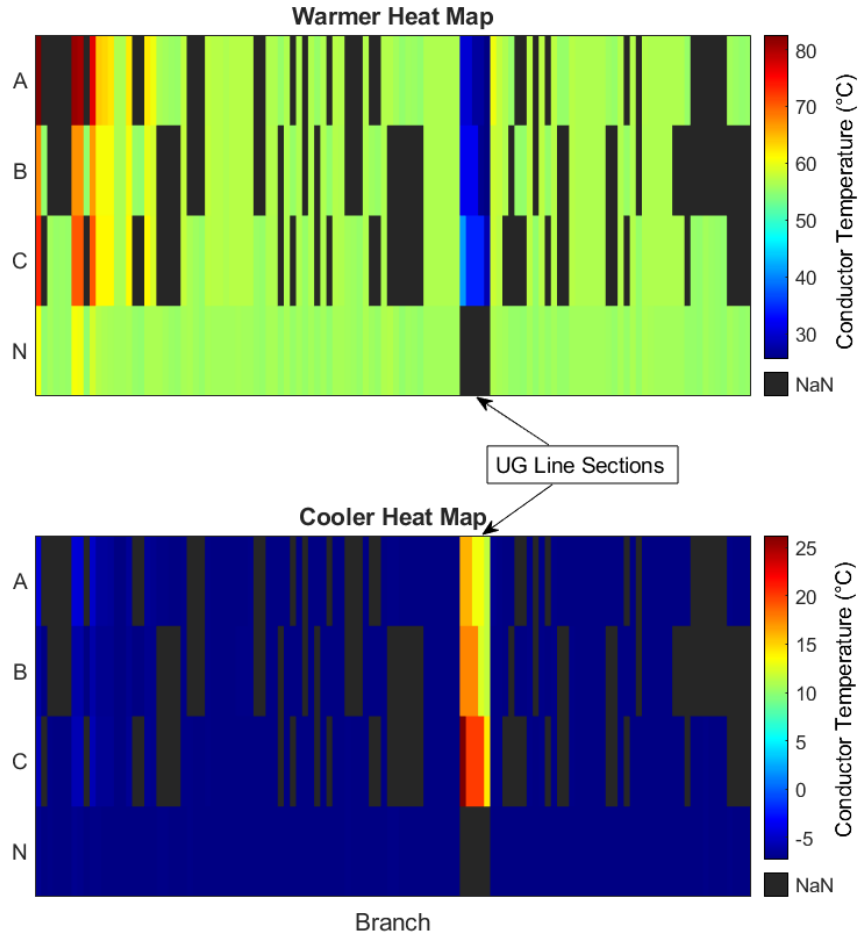

Figure 6.28: 123-node feeder: branch heatmap, cooler and warmer extreme conditions

The heatmap of Fig. 6.28 shows the calculated temperatures for all overhead and underground line sections in the 123-node test feeder for both the cooler and warmer

cases. As in the similar plot for the 13-node case, the vertical axes are annotated by phase, and the horizontal axes by the branch receiving node, however the branch annotation is not shown due to visibility constraints. Only branches corresponding to overhead and underground line sections are shown (transformer, switch, and regulator branches omitted). Additionally, the temperatures of phases not present for a given line section are shown as NaN (not a number). The top portion of Fig. 6.28 shows the heatmap corresponding to the warmer scenario, and the lower portion the cooler scenario. The annotated columns of the heatmaps slightly more than halfway down correspond to underground line sections, with all other columns representing overhead line sections.

Again, as in the 13-node case, it can be noted that the deviation in temperature for the overhead line sections is much greater than that for the underground sections when comparing the warmer and cooler scenarios, and that the underground line sections stay much warmer than the overhead lines in the cooler case, and much cooler than the overhead lines in the warmer case, again due to the relative stability of the soil temperature as compared to the weather conditions. The main feeders leaving the source node can clearly be seen in the first few columns of the warmer heatmap (neglecting the second through sixth columns, which are single-phase laterals close to the source node) as being much warmer than other branches, as they carry the current for large portions of the feeder. In the warmer case, all overhead conductor temperatures are above the $50°C$ implicit in the benchmark solution, and the underground conductor temperatures are well below. In the cooler case, all conductor temperatures are well below this implied temperature.

Table 6.17: Comparison to benchmark results: voltage deviation, cooler and warmer extreme conditions, 123-node feeder

	Average Absolute Deviation			
	Phase A (pu)	Phase B (pu)	Phase C (pu)	Maximum Deviation (pu)
Cooler	$4.6 \cdot 10^{-3}$	$2.4 \cdot 10^{-3}$	$2.2 \cdot 10^{-3}$	$8.2 \cdot 10^{-3}$
Warmer	$1.7 \cdot 10^{-3}$	$5.5 \cdot 10^{-4}$	$8.6 \cdot 10^{-4}$	$4.8 \cdot 10^{-3}$

Table 6.17 gives the average absolute deviation in voltage magnitude of each phase and the maximum deviation for the cooler and warmer extreme cases as compared to the benchmark solution. As in the 13-node feeder case, the deviations are relatively small, with the maximum deviation in the cooler case approaching 0.01 pu. This is comparable to the results of the much smaller 13-node case. However, in the case of the 123-node feeder, the voltage regulators have actively shifted taps between the warmer and cooler cases, mitigating the passive effect of the conductor temperatures to affect the node voltage magnitudes. It is reasonable to assert that without the active support of the voltage regulators to sense and respond to the passively changing voltages, the voltage deviations in this much larger case would have been noticeably higher than the 13-node feeder case.

The feeder voltage profile for warmer and cooler cases and the benchmark can be seen graphically in Fig. 6.29. It can be noted that, in general, the voltage magnitudes in the cooler case are higher, as anticipated based on the 13-node feeder results, with lower losses resulting from cooler conductor temperatures producing comparatively higher node voltage magnitudes. However, looking closely, there are several instances where the voltage magnitudes are lower in the cooler case versus the warmer case and the benchmark.

This can be seen much better by focusing on several portions of the profile, as seen in Fig. 6.30. We can note that these lower voltage magnitudes in the cooler conditions

case occur in the areas of the feeder downstream from the regulators RG2, RG3, and RG4 which are known to change tap settings between the warmer and cooler cases, an was noted in Table 6.16.

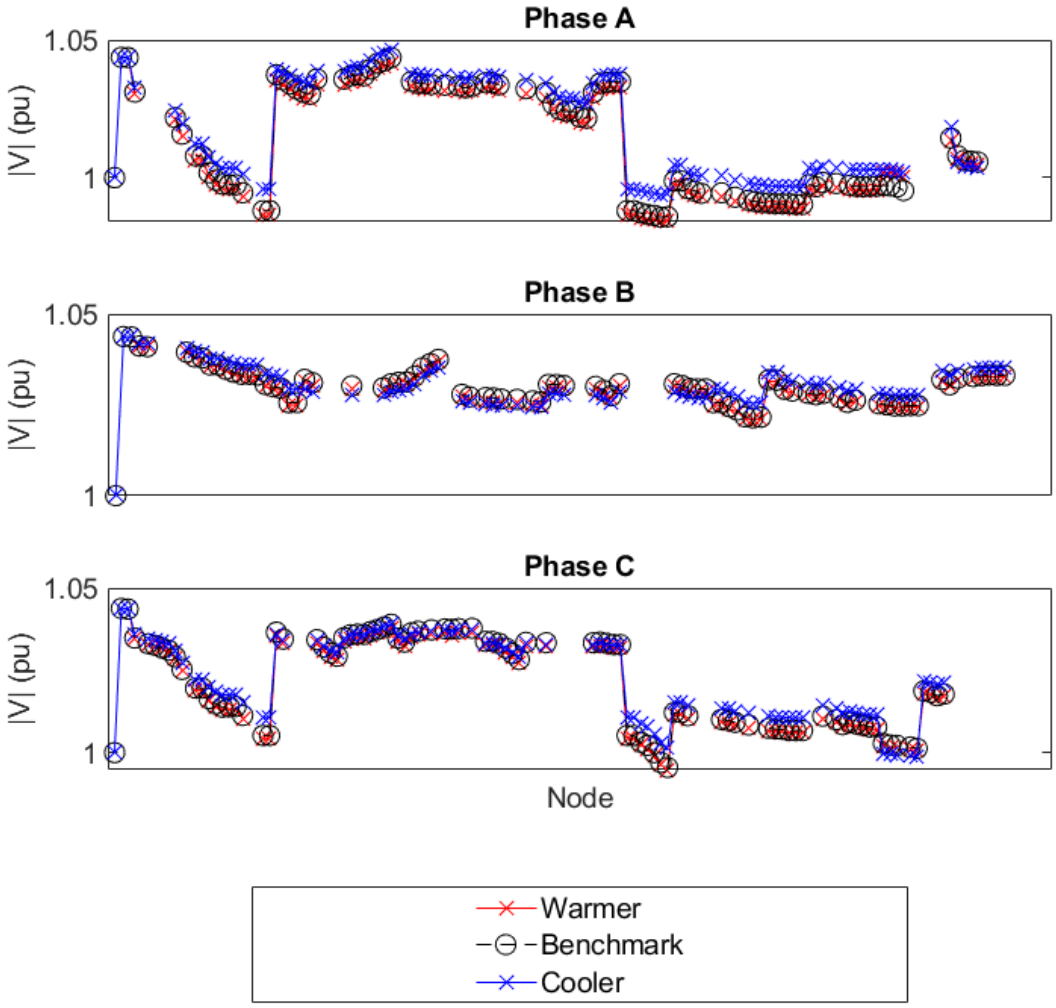

Figure 6.29: 123-node feeder: voltage profile, cooler and warmer extreme conditions

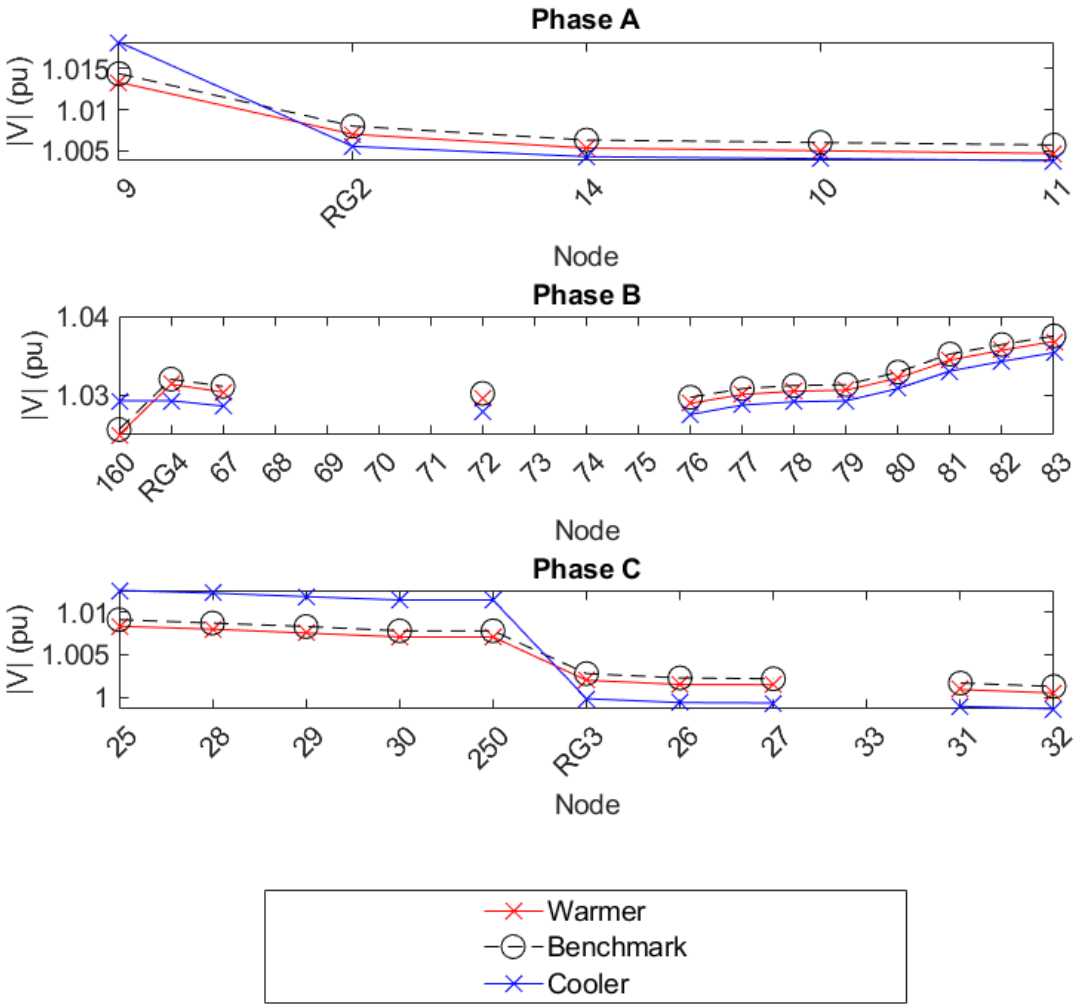

Figure 6.30: 123-node feeder: voltage profile, cooler and warmer extreme conditions, detail

It can then be concluded that the simulated voltages in the compensator circuits, representative of the voltage at the load centers, in the iteration of the power flow algorithm prior to the setting of the regulator taps (see section 5.2) are so high as to require less support, or further reduction, in the downstream voltage than that of the warmer case and the benchmark. As the regulator can only modify voltage

magnitudes in fixed increments, this pushes the voltages below that of the warmer case and the benchmark. For example, looking at the phase B portion of Fig. 6.30, where in the warmer case and the benchmark, the voltage was increased on phase B on the secondary side of RG4 (node RG4) by one increment, or 0.00625 pu, the tap setting was reduced to zero in the cooler case, and the phase B voltage on the secondary side is then equal to the voltage on the primary side (node 160). Similarly, in the phase A and phase C portions of Fig. 6.30, for RG2 and RG3 respectively, an additional decrement in voltage is required in the cooler case to satisfy the phase voltage set points at the simulated load centers due to the comparatively high voltage on the regulator primaries.

The calculated real power losses for the extreme cases and the benchmark can be seen in Table 6.18. As in the 13-node feeder test case, it can be noted that the warmer case shows the expected increased losses, and the cooler case shows a decrease in loss, as compared to the benchmark case.

Table 6.18: Extreme cases and benchmark results: real power loss, 123-node feeder

	Phase A (kW)	Phase B (kW)	Phase C (kW)	Total (kW)
Benchmark	50.54	10.13	34.94	95.61
Warmer	53.30	10.86	36.14	100.30
Cooler	39.31	6.41	28.28	74.00

With reference to the conductor heatmaps of Fig. 6.28, there are higher real power losses in the case of conductor temperatures largely exceeding the implicit $50°C$ of the benchmark case, and the opposite effect when the conductor temperatures are much lower. The warmer case total real power loss of 100.3 kW corresponds to an increase in losses of 4.9%, and the cooler case loss of 74 kW corresponds to a decrease of 22.6%, which is comparable to what was observed in the 13-node test case.

Fig. 6.31 shows the branch real power losses for the 123-node feeder as the summed

loss across all phases present for a given branch. Only the branches with the most significant loss have been annotated. These branches correspond to the branches that serve as primary feeders to all or large portions of the feeder, and/or are longer than comparably loaded branches in their vicinity.

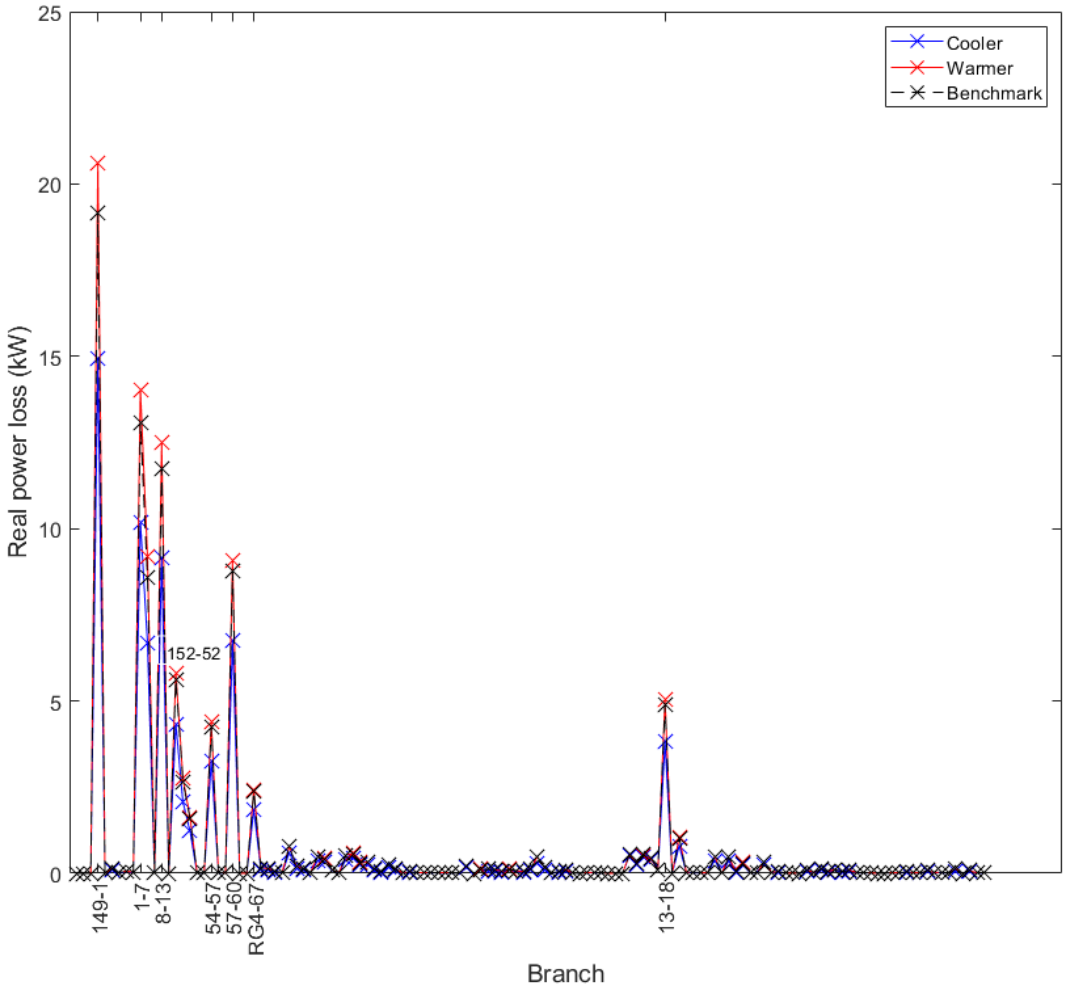

Figure 6.31: 123-node feeder: branch losses, cooler and warmer extreme conditions, detail

The branch losses increase uniformly in the warmer case, and decrease in the cooler case. This is irrespective of the effect on the voltage characteristics noted due to the tap changing of the voltage regulators.

However, the action of the voltage regulators does have an effect on the character-

istics of the node voltage unbalance. It was observed in the 13-node test case that the passive effect of increased conductor temperature was to magnify the degree of voltage unbalance at all nodes, however marginally. In Fig. 6.32 it can be noted that this is not necessarily true for the 123-node feeder.

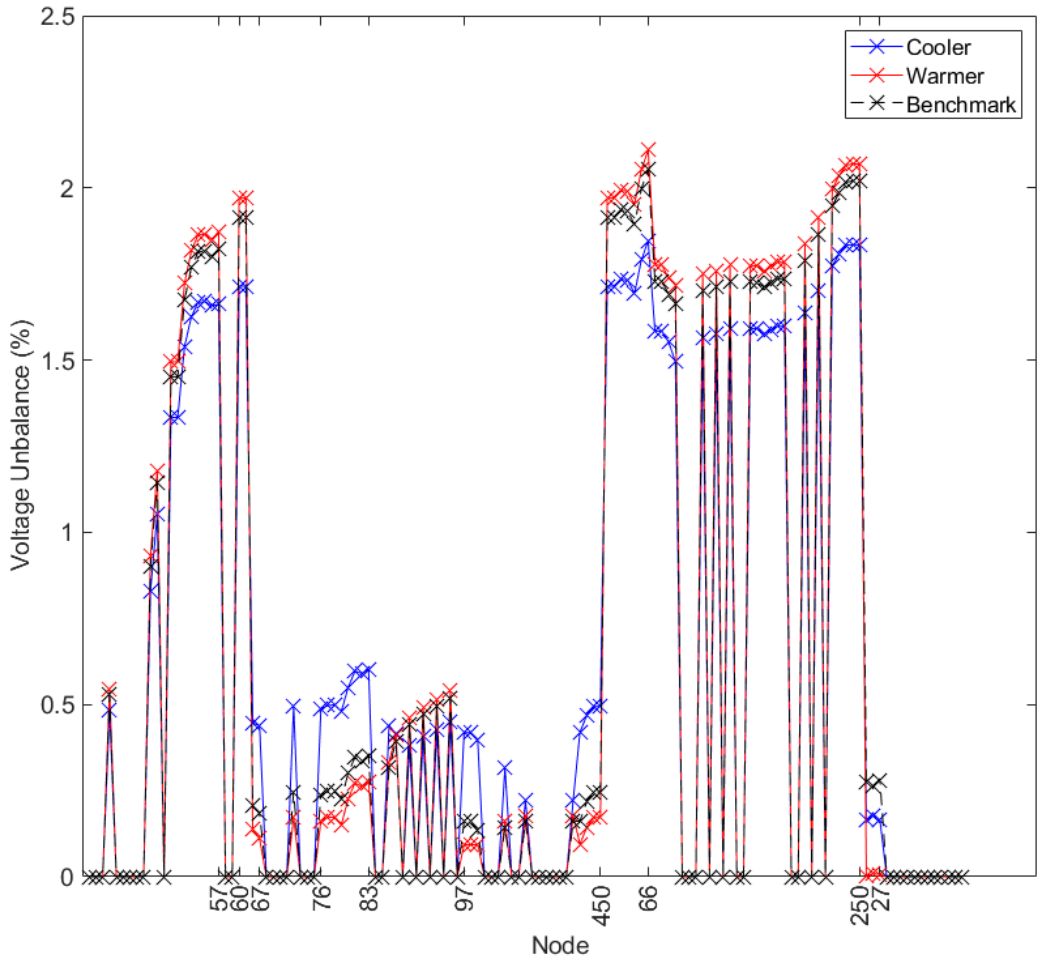

Figure 6.32: 123-node feeder: voltage unbalance, cooler and warmer extreme conditions

At nodes 67, 76, 83, 97, and 450, among others, the voltage unbalance at the node in the cooler case has increased as much as 0.25% above the benchmark, while the warmer case voltage unbalance has decreased by $\approx$ 0.1%. These nodes are all downstream from RG4, and the presumption must be that this difference in behavior

is caused by the difference in tap settings of this voltage regulator and the subsequent effect on the voltage profile, as noted in Fig. 6.30 and discussed above. RG2 and RG3 also change tap settings between the warmer and cooler cases, but RG2 is a single-phase regulator serving a single-phase lateral, where the voltage unbalance is zero or undefined. The portion of the feeder downstream from two-phase regulator RG3 can be seen in the area around the node 27 annotation, where the voltage unbalance is higher in the benchmark case than either the warmer or the cooler case. Therefore, the assertion must be that in the presence of active voltage regulation in response to changes in conductor temperature, no single assumption can be made about the effect on voltage unbalance. It depends entirely on the system-level behavior of the feeder, which is governed by passive and active elements (e.g., line sections and voltage regulators) whose response is difficult to predict without these types of iterative analyses.

6.5.2.2 Steady-State Time-Series: Year 2020

In this section the data sets of section 6.3 were used in the temperature-dependent power flow algorithm of section 5.3 and applied to the 123-node feeder in the same manner as for the 13-node feeder in section 6.4.2.2. As in section 6.4.2.2, the steady-state time-series analysis provides a sense of the state of the feeder at each hourly increment of time over the course of year 2020 with load held constant, subject to variations in ambient conditions.

The analysis of the steady-state time-series results must begin by looking at the changing tap settings of the voltage regulators present on the feeder, as was discussed in the previous extreme condition section. In the previous section, some regulator tap settings were observed to change by one increment between the warmest and coolest extreme conditions. Fig. 6.33 shows the change in the tap settings of all regulators over the course of the year.

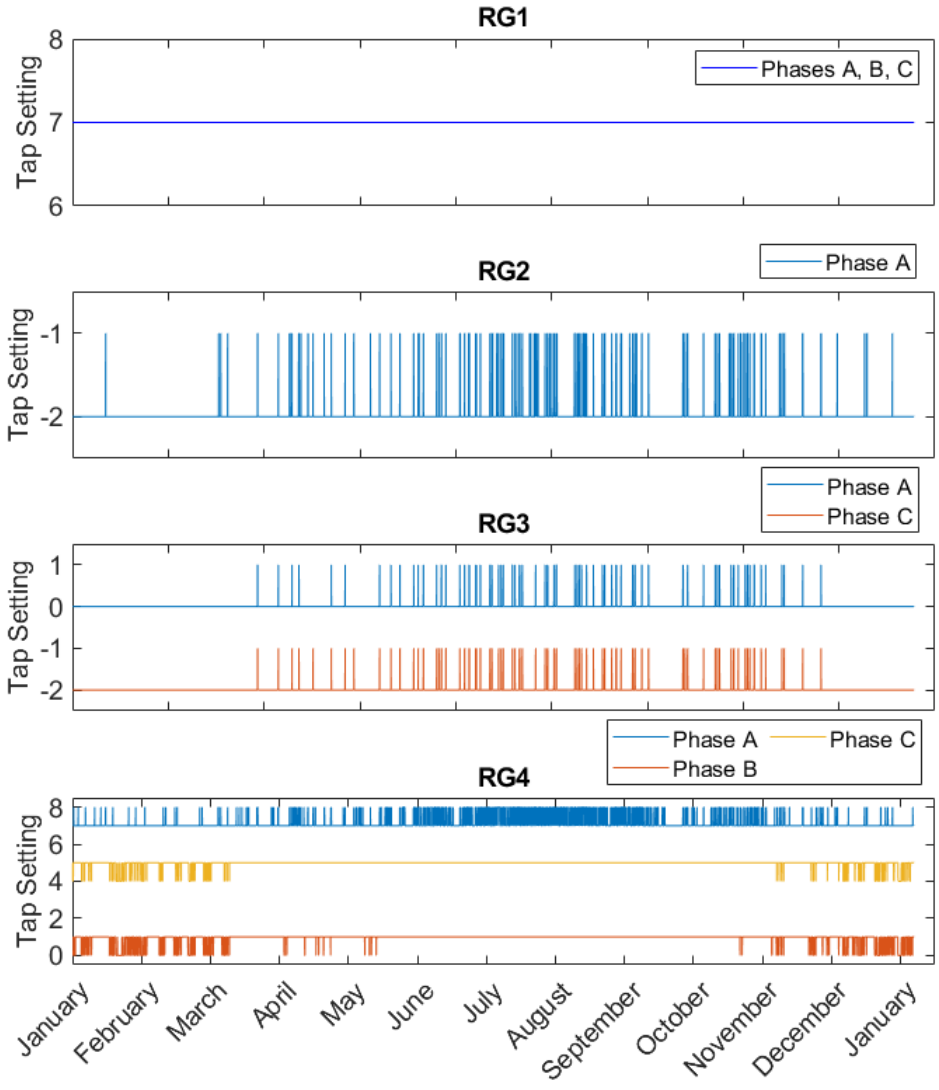

Figure 6.33: 123-node feeder: variable regulator tap settings, 2020

It can be observed that the tap settings of RG1 at the source node remain constant, while the tap settings of the other regulators oscillate in response to changing system conditions brought on by the consideration of the conductor temperature. Interestingly, the tap settings of RG2, RG3, and phase A of RG4 tend to oscillate more during the warmer times of the year, while phases B and C of RG4 oscillate more during the cooler times of the year. Due to the nature of the regulator modeling and tap setting calculation, which involves a rounding operation (see section 3.6), it can be deduced

that system conditions in the warmer months (higher losses, resistance, and voltage drops) cause the simulated voltage at the load centers for RG2, RG3, and phase A of RG4 to straddle two intervals that dictate the tap setting. The inverse is true for phase B and phase C of RG4, where during the warmer months, the simulated load center voltages are firmly within the observed tap setting interval, and they straddle two intervals in the cooler months.

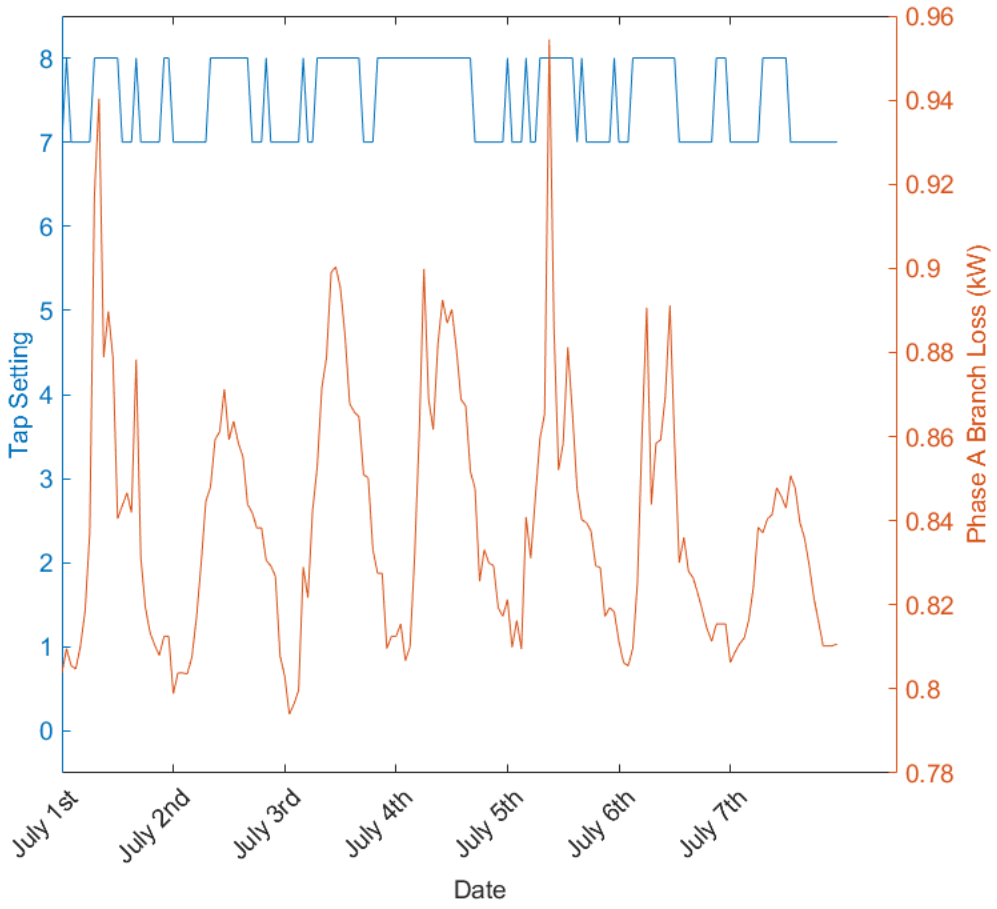

Figure 6.34: 123-node feeder: RG4 phase A tap setting and branch RG4-67 phase A loss, 2020

Taking a closer look at the phase A tap setting of RG4 and the phase A real power losses of downstream branch RG4-67, Fig. 6.34 shows the steady-state time-series results for the first week of July, during the period of high tap setting oscillation. As expected, the changing of regulator tap to a higher setting largely corresponds to

time intervals of peaking loss, which occurs around midday, when the lower voltage magnitudes corresponding to higher loss require more support.

In looking at the variation in voltage profile over the year, then, it is expected to not only observe the passive response of the voltage magnitudes to changing conductor temperature, but also the embedded active control of the voltage regulators.

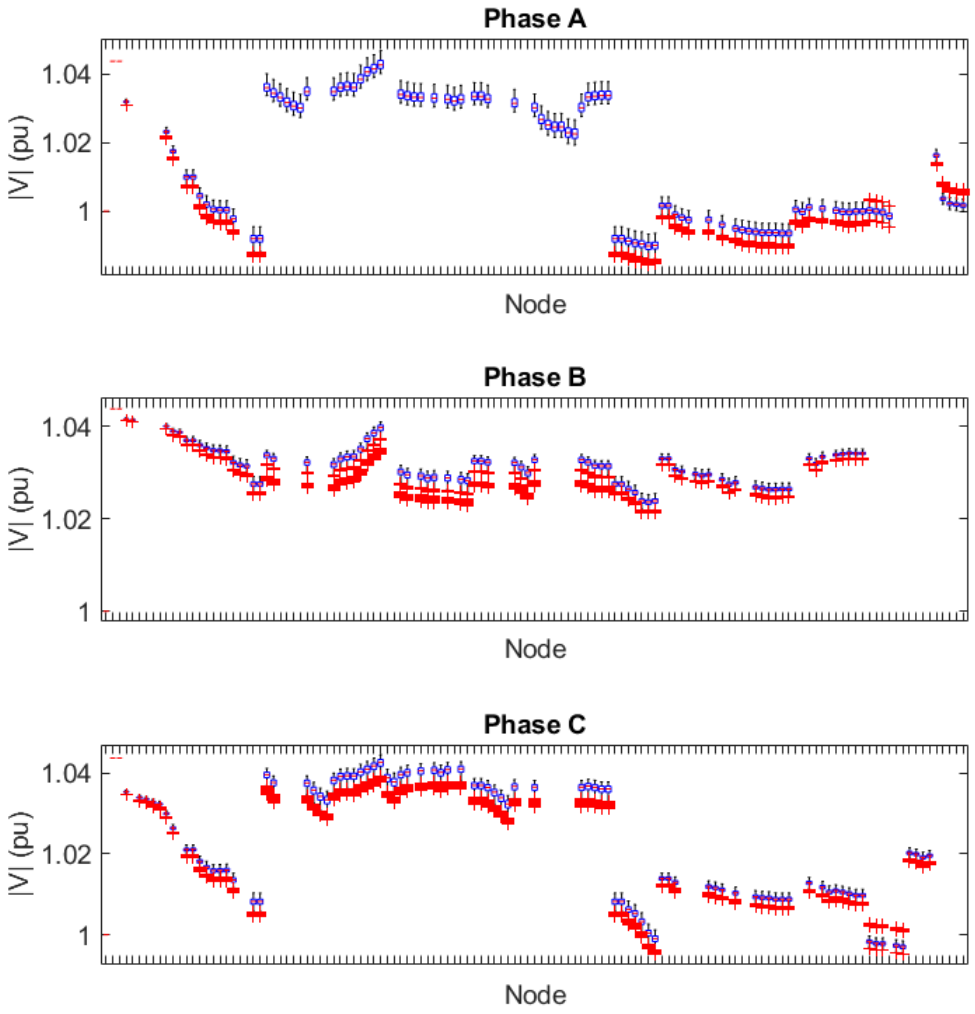

Figure 6.35: 123-node feeder: node voltage magnitude box and whiskers

Fig. 6.35 shows the variation in the voltage profile in the form of a box-and-whiskers plot. The variation in maximum and minimum voltage magnitudes for a given node

is comparable to that seen in the 13-node test case, with a maximum difference of about 0.01 pu. So again, even considering the actions of the voltage regulators in this case, it can be concluded that the effect of the consideration of conductor temperature on voltage magnitude is minimal. One thing of note in Fig. 6.35 is that there are significantly more outliers in general than in the 13-node test case. This is presumably due to the action of the voltage regulators, as the number of outliers (shown in red), tends to increase downstream from the regulators in the nodes more distant from the source node, which is at the extreme left-hand side of the figure.

The maximum voltage magnitude deviation from the benchmark solution for the 13-node case, as was shown in Fig. 6.17, tended to trend towards zero as the lines became warmer during the warmer portion of the year, and become more positive (higher voltages than the benchmark) during the cooler months. Fig. 6.17 also showed that the voltage at the node with the highest deviation was greater than that of the benchmark solution 99% of the time. In contrast, Fig. 6.36 shows no apparent trend related to the passive change of the line conductor temperature, but instead shows oscillation between positive and negative maximum deviation. This maximum node voltage magnitude deviation occurs at the secondary node of RG2 or RG3 51.7% of the time, and at end nodes 33 (downstream from RG3), 66, and 85 (downstream from RG4) otherwise. The oscillations of the tap settings of RG2, RG3, and RG4 can be seen in the oscillations of Fig. 6.36 between positive and negative values, as the voltage magnitudes vary from greater than to less than the benchmark. The maximum deviation is greater than the benchmark $\approx$ 48.6% of the time, much less consistently than in the 13-node case.

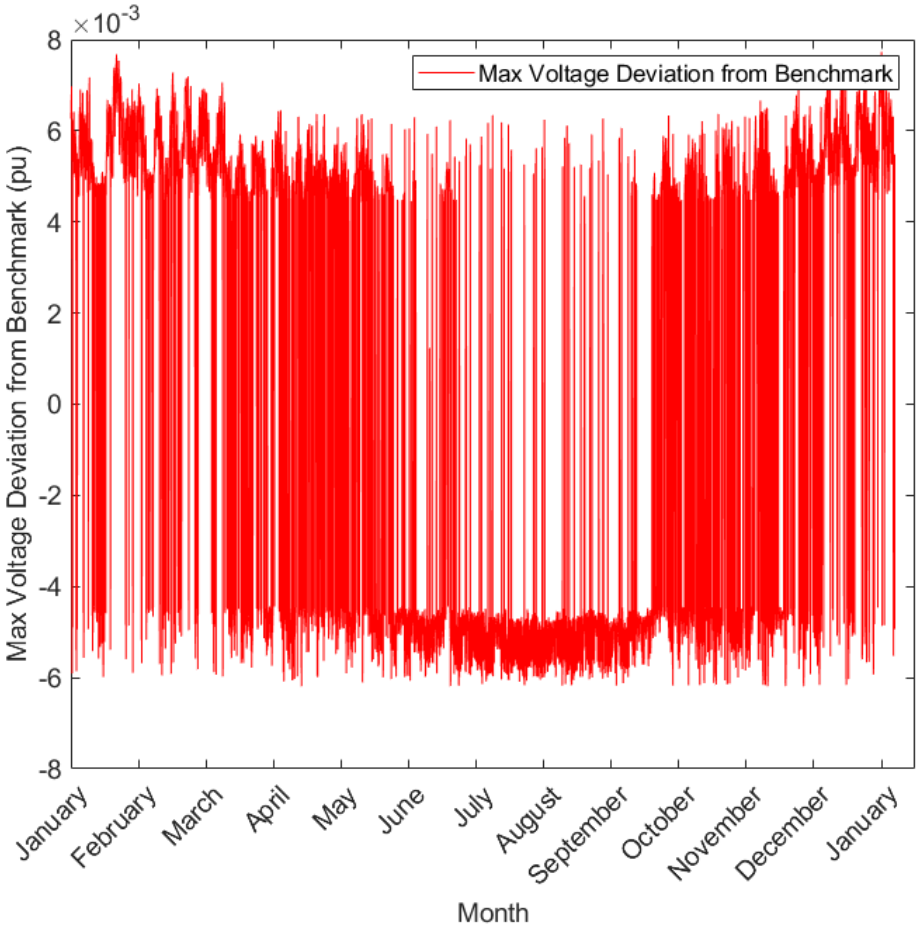

Figure 6.36: 123-node feeder: maximum voltage deviation from benchmark

The correlation between total losses and ambient air temperature is again emphasized in Fig. 6.37 for the 123-node feeder which, as the 13-node feeder, is primarily composed of overhead lines. The benchmark constant loss over the year, not considering the variability in conductor temperature, is shown as the black dashed line. As in the 13-node feeder case, it can be seen that only infrequently does the calculated total loss reach or exceed the benchmark loss ($\approx 1\%$ of the time). Much more frequently, the calculated losses are less than the benchmark value ($\approx 99\%$ of the time). The average loss, shown as the black dotted line, is 11.4% less than the benchmark value. These characteristics are almost identically comparable to the analysis of total losses for the 13-node feeder.

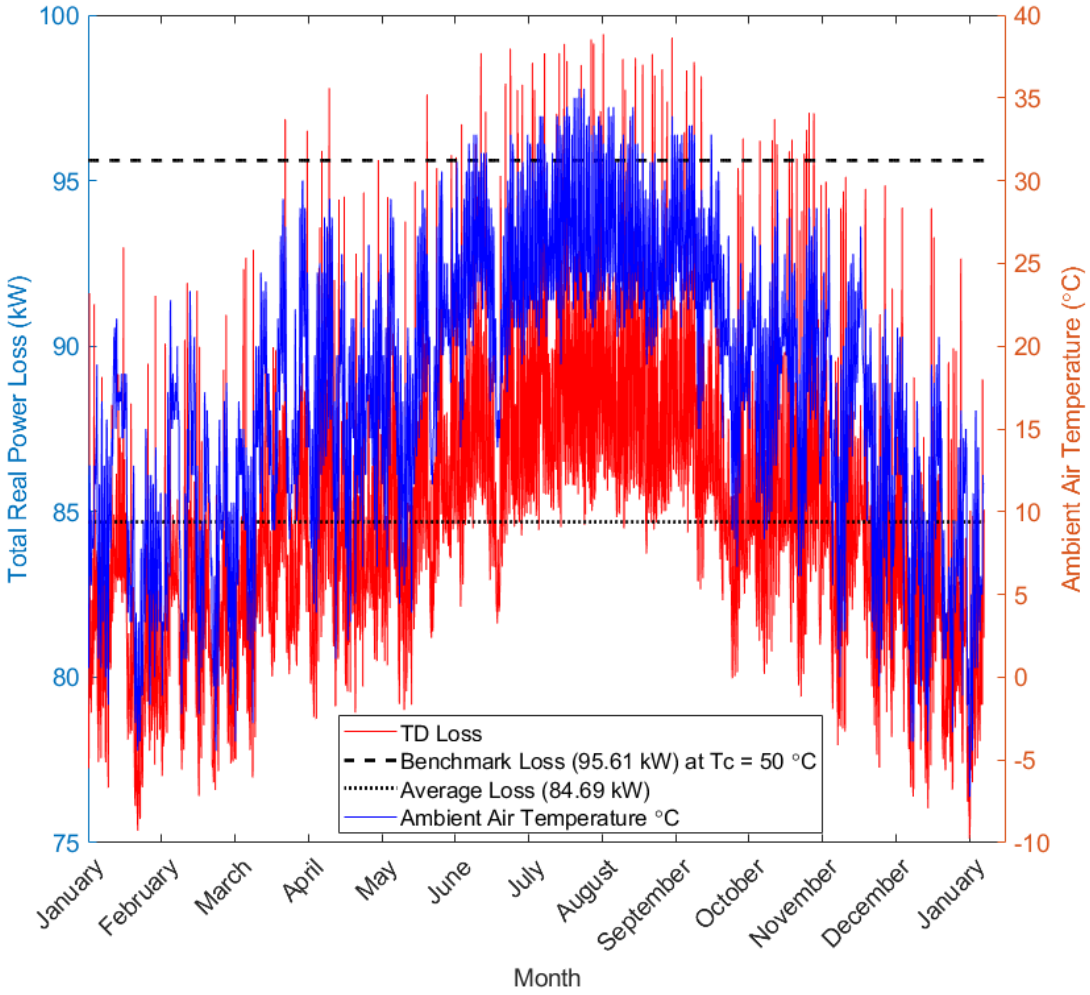

Figure 6.37: 123-node feeder: total loss and ambient air temperature, 2020

With reference to Fig. 6.37, Table 6.19 gives the incidence of highest and lowest loss over the course of the year along with the accompanying weather parameters and time of occurrence.

Table 6.19: 123-node feeder: highest and lowest loss occurrence, 2020

	Date	Total loss (kW)	Air temp ($°C$)	Soil temp ($°C$)	Wind speed (m/s)
Highest	7/29, 12pm	99.4	32.22	24.44	0
Lowest	12/26, 4am	75.1	-7.22	13.33	1.34

These maximum and minimum losses occur at the same times, and therefore under the same ambient conditions, as those noted in the 13-node case. Coupled with the discussion on Fig. 6.37 above, it seems compelling that the variation in loss is strongly governed by ambient conditions versus being system dependent, i.e. the ambient conditions uniformly affect systems in very similar ways with respect to real power loss, regardless of system size or topology. This assertion is expected to hold for distribution systems with similar proportions of underground to overhead lines as the 13- and 123-node test cases. A system composed of a high proportion of underground lines would be expected to show less variation in loss due to less variable conductor temperatures, as was noted in Figs. 6.12 and 6.15.

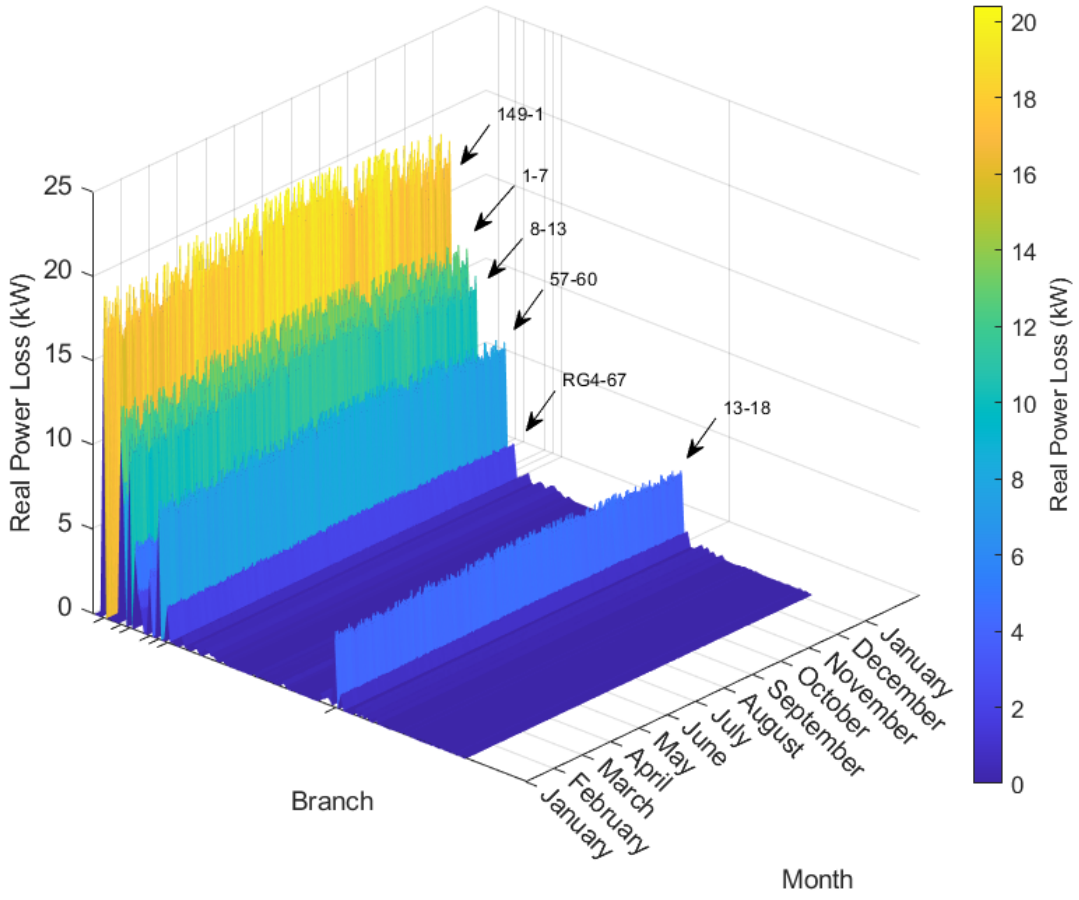

Figure 6.38: 123-node feeder: branch losses, 2020

Fig. 6.38 shows the variation in branch losses throughout the year. The variation in branch loss for the underground lines is in the 5% range, while for the overhead lines varies approximately 22-37%. The percent variation in the loss tends to be towards the low end of that range for the more highly loaded, high loss lines, and towards the higher end of the range for the lightly loaded, lower loss lines.

Fig. 6.39 shows the voltage unbalance at each node as calculated by Eq. 6.1 over the course of the year. As in Fig. 6.32, the highest degree of unbalance occurs on the end node 66, which varies just slightly throughout the year. The maximum and minimum voltage unbalance occurring at node 66 and the time and date of occurrence can be seen in Table 6.20.

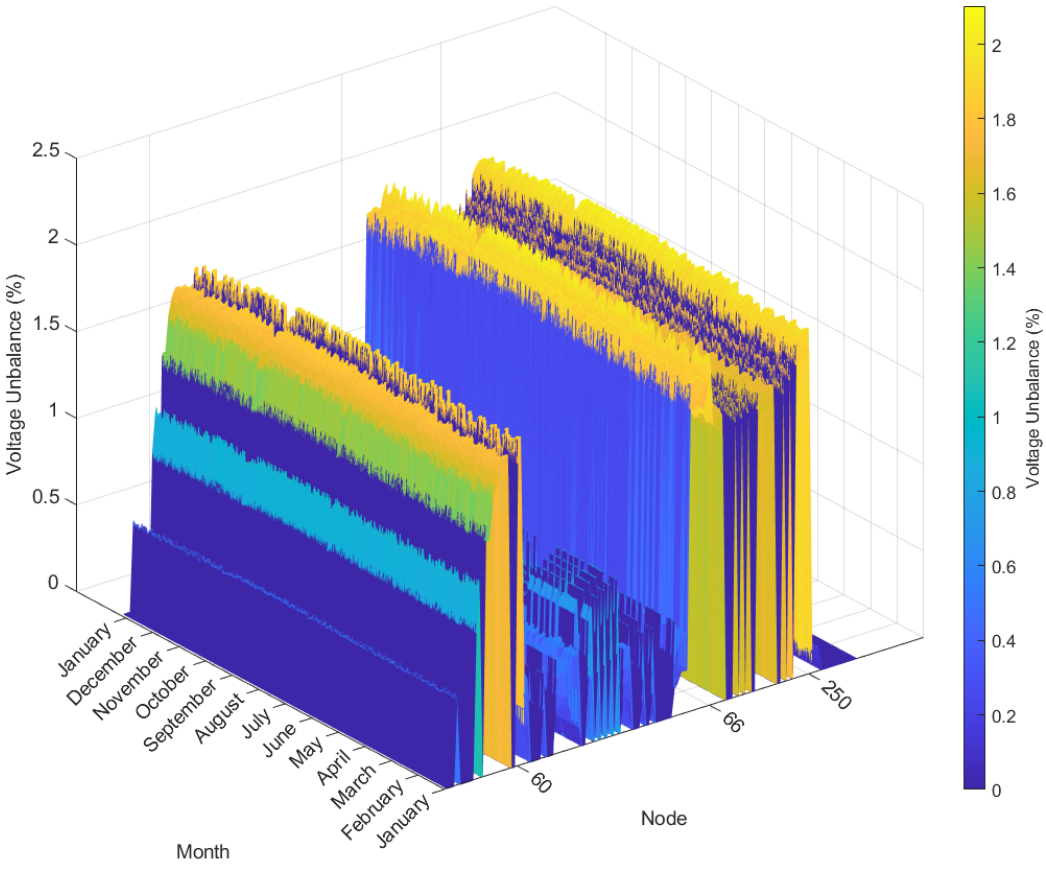

Figure 6.39: 123-node feeder: node voltage unbalance, 2020

Referencing Table 6.19, it is no surprise that the incidence of highest and lowest total real power loss are coincident with the highest and lowest degree of voltage unbalance, which also coincide with the maximum and minimum loss and voltage unbalance results for the 13-node feeder.

Table 6.20: 123-node feeder: highest and lowest voltage unbalance occurrence, 2020

	Date	Voltage unbalance (%)	Air temp ($°C$)	Soil temp ($°C$)	Wind speed (m/s)
Highest	7/29, 12pm	2.10	32.22	24.44	0
Lowest	12/26, 4am	1.86	-7.22	13.33	1.34

This chapter presented results for the application of the proposed temperature-dependent three-phase power flow for unbalanced radial systems. A discussion and overview of these results will be given in the next and final chapter, which also includes a summary of research contributions and a discussion of possible future work.

CHAPTER 7: CONCLUSION AND FUTURE WORK

7.1 Overview

This work presented a temperature-dependent, three-phase power flow algorithm for radial distribution systems that is capable of accommodating system unbalance, ZIP loads, and both overhead and underground line sections. This chapter concludes the work with three sections. The first section is a discussion and summary of the results of the case studies in Chapter 6. The second section will summarize the research contributions, and the final section discusses avenues of future work related to the topic covered herein.

7.2 Discussion of Case Study Results

Power flow is an essential, foundational aspect of the operation and planning of electric power systems. The information gained from modeling existing real-life systems in power flow software serves as the basis for processes such as state estimation, optimal power flow, fault analysis, transient stability studies, and the development of control strategies, as well as being of vital importance in the design of planned expansion. For this reason, the accuracy of the power flow solution is of paramount importance.

In engineering there is the acknowledged concept of a trade-off between modeling and computational complexity and accuracy. As a system model becomes more involved in the interest of accuracy, the computational burden increases, sometimes in cases where the simpler model would have been "good enough" for some purposes. Whether or not a certain purpose requires the additional layer of complexity is a matter of discussion and is dependent on the application. The intent of this work was

not necessarily to define the grounds for the application of a temperature-dependent power flow model for distribution systems, but to show the nature of the changes caused by the consideration of conductor temperature in the power flow modeling of the case studies considered in Chapter 6.

In terms of computational time or "speed" of the proposed temperature-dependent versus the conventional power flow algorithm, the introduction of temperature dependency did not add significant additional computational time. With the algorithms coded in MATLAB R2020a and executed on a machine with Intel core i7, 3.4GHz processor with 18GB ram, an average convergence of the temperature-dependent algorithm for the 13- and 123-node test cases was 0.019 and 0.285 seconds respectively, as opposed to 0.017 and 0.256 seconds respectively for the conventional algorithm. This suggest much of the computational overhead is in the backward-forward sweep process itself, rather than the temperature calculations.

The results of the case studies, all conducted with constant base load, showed that the conductor temperature of overhead lines can vary widely when subjected to weather extremes, from just above the ambient air temperature in the cooler extreme, to over twice the air temperature in the warmer extreme, and often very different from the $50°C$ assumed in the benchmark case solutions. Overhead lines tend to have a more highly variable conductor temperature over the course of the year than underground cables, as overhead lines are exposed to the air temperature, which is more highly variable than soil temperature. The overhead lines are also greatly impacted by the changes in wind speed and solar heating.

In contrast, the temperature of underground cables was found to be more stable and perhaps predictable due to the dependence on the comparatively stable temperature of the surrounding soil medium. Further, it was observed that for the test systems studied, the underground lines stayed cooler in the warmer months, and warmer in the cooler months, than the overhead lines. Conductor temperature for overhead

lines tends to follow the annual trend of air temperature, with variable wind speed causing deviations to this trend, while underground cable temperatures trend with soil temperature, which consequently trends with air temperature subject to a thermal lag. The conductor resistance, modeled as a piece-wise linear function of conductor temperature, trends with conductor temperature and could vary by more than 20%.

These trends in conductor temperature and resistance were reflected in the observed trends in node voltage magnitude, power loss, and voltage unbalance, when the tap settings of voltage regulators present on the feeder were not affected, as in the 13-node case study. The observed trends due to this passive action of the conductor temperature were that higher conductor temperature led to higher losses, lower voltage magnitudes, and higher degree of voltage unbalance. The line current was found to, of course, vary with the varying conductor resistances and node voltages, but whether it increased or decreased with conductor temperature was dependent on the way the load was modeled. Currents serving a majority constant power load increased with conductor temperature, while currents serving a constant impedance load will decrease with increased conductor temperature. The magnitude of current serving a constant current load is, of course, constant. Voltage and current magnitudes were seen to vary over the course of the year by as much as $\approx 1\%$ and the percent voltage unbalance by as much as 0.6%.

In the 123-node case study, the effect of conductor temperature on the node voltages was observed to cause some voltage regulators to change tap settings, and this active control on the system obscured the previously noted passive effect of conductor temperature on the voltage profile and the voltage unbalance, leading to some node voltages being higher and some node unbalance being lower with high conductor temperatures. Thus, while in the 13-node case a trend in conductor temperature was seen to imply certain trends in node voltage magnitude and unbalance, in cases where the changing system conditions also affect the voltage regulators, the effect on specific

node voltages can be difficult to predict without power flow analysis.

Even in the case of changes in the regulator tap settings, however, branch and total losses were found to uniformly trend with conductor temperature; in both case studies, higher conductor temperature was found to indicate higher losses. The power losses showed much greater variability than voltage magnitude and unbalance, being 23-24% different between the highest and lowest loss cases of the year. The highest and lowest calculated loss in the 13- and 123-node case was 3-4% greater and 21% lower, respectively, than that of the benchmark solutions.

Often, test cases can be intended to reflect conservative assumptions about component modeling and parameters, and based on the results of this work, the 13- and 123-node test cases tend to do that concerning real power loss. The total loss is found to be less than that of the benchmark solution 99% of the time, and it could be said the resistances and implied conductor temperature of the benchmark represent a "worst case" scenario. More often, outside of the "worst case", voltage magnitudes are higher, and voltage unbalance and loss are lower, than that calculated under the $50°C$ conductor temperature assumption.

7.3 Summary of Contributions

The research contributions of this work can be summarized as follows:

- Synthesis of three-phase component modeling from first principles for power flow studies;
  - Transformers of various primary and secondary connections
  - Voltage regulator
  - Capacitor banks (delta and wye connected, single- and three-phase)
  - ZIP loads (delta and wye connected, single-, two-, and three-phase)
  - Overhead and underground lines

- Development and implementation of three-phase BFS-based power flow algorithm for radial systems capable of accommodating unbalanced loading and incorporating component models listed above;
- Synthesis of electrothermal modeling indicated by IEEE Std. 738 for bare overhead conductors;
  - Development and implementation of bisection algorithm to enable fast computation of IEEE Std. 738 equations governing non-linear relationship between conductor temperature and current
- Synthesis of electrothermal modeling indicated by IEC 60287 for underground cables;
  - Development and implementation of subroutine to calculate cable conductor temperature utilizing the relationships presented in IEC 60287
- Incorporation of electrothermal modeling into derivation of phase impedance matrices for power flow algorithm;
  - Matrices developed from first principles at each iteration to account for variation in conductor temperature and corresponding resistance;
- Development and implementation of power flow algorithm mentioned above with incorporation of electrothermal modeling of overhead lines and underground cables.

7.4 Future Work

Interesting avenues of future work include the following:

- Greater generalization/refinement of the temperature calculation of underground cable to include more types of cable construction.

- Automate the pre-processing steps to develop the branch and node data matrices that serve as input to the algorithm. This data is often in Excel, OpenDSS, or another data format. This will allow efficient simulation of larger systems.

- Expand to co-simulation with temperature-dependent power flow for transmission systems. This will require a three-phase temperature-dependent power flow model for transmission systems, likely Newton-Raphson based.

- The above expansion to co-simulation could enable an exciting temperature-dependent optimal power flow with more accurate consideration of losses at both transmission and distribution system levels.

- Investigate the effect of conductor temperature on distribution system capacity for power transfer considering line thermal and voltage stability limits. This could also be expanded to co-simulation with transmission systems.

REFERENCES

[1] S. Lumbreras and A. Ramos, "The new challenges to transmission expansion planning. survey of recent practice and literature review," *Electric Power Systems Research*, vol. 134, no. 1, pp. 19–29, 2016-05.

[2] P. Song, Z. Xiu, H. Ding, H. Cai, and Z. Xie, "Security-constrained line loss minimization in distribution systems with high penetration of renewable energy using upfc," *Journal of Modern Power Systems and Clean Energy*, vol. 5, no. ue 6, pp. 876–886,, 2017-11.

[3] B. Xu, A. Ulbig, and G. Andersson, "Impacts of dynamic line rating on power dispatch performance and grid integration of renewable energy sources," *IEEE PES ISGT Europe*, pp. 1–5, 2013.

[4] R. Adapa and D. Douglass, "Dynamic thermal ratings: monitors and calculation methods," in *2005 IEEE Power Engineering Society Inaugural Conference and Exposition in Africa*, (Durban), pp. 163–167, 2005.

[5] A. Michiorri, P. Taylor, S. Jupe, and C. Berry, "Investigation into the influence of environmental conditions on power system ratings," *Proceedings of the Institution of Mechanical Engineers*, vol. 223, 2009.

[6] X. Dong, "Calculation of power transfer limit considering electro-thermal coupling of overhead transmission line," *IEEE Transactions on Power Systems*, vol. 29, no. 4, pp. 1503–1511,, 2014-07.

[7] "IEEE standard for calculating the current-temperature relationship of bare overhead conductors," *IEEE Std 738-2012 (Revision of IEEE Std 738-2006 - Incorporates IEEE Std 738-2012 Cor 1-2013*, vol. l, pp. 1–72, 2013-12-23.

[8] "CIGRE guide for thermal rating calculations of overhead lines, technical brochure 601, study committee b2," *WG*, vol. B2, no. 42, pp. 1–95, 2014.

[9] V. Cecchi, M. Knudson, and K. Miu, "System impacts of temperature-dependent transmission line models," *IEEE Transactions on Power Delivery*, vol. 28, no. 4, pp. 2300–2308, 2013-10.

[10] S. Jagarlapudi and V. Cecchi, "Investigating wind speed-dependent models for electric power transmission lines," in *2016 IEEE International Symposium on Circuits and Systems (ISCAS)*, (Montreal, QC), pp. 626–629, 2016.

[11] W. Tinney and C. Hart, "Power flow solution by newton's method," *IEEE Transactions on Power Apparatus and Systems*, vol. 86, no. 11, pp. 1449–1460, 1967-11.

[12] B. Stott and O. Alsac, "Fast decoupled load flow," *IEEE Transactions on Power Apparatus and Systems*, vol. 93, no. 3, pp. 859–869, 1974-05.

[13] A. Sasson, C. Trevino, and F. Aboytes, "Improved newton's load flow through a minimization technique," *IEEE Transactions on Power Apparatus and Systems*, vol. 90, no. 5, pp. 1974–1981, 1971-09.

[14] S. Frank, J. Sexauer, and S. Mohagheghi, "Temperature-dependent power flow," *IEEE Transaction on Power Systems*, vol. 28, (4, pp. 4007–4018, 2013.

[15] J. Santos, A. Exposito, and F. Sanchez, "Assessment of conductor thermal models for grid studies," *IET Generation, Transmission Distribution*, vol. 1, no. 1, pp. 155–161, 2007.

[16] M. Rahman, V. Cecchi, and K. Miu, "Power handling capabilities of transmission systems using a temperature-dependent power flow," *Electric Power Systems Research*, vol. 169, pp. 241–249, 2019-04.

[17] A. Ahmed, F. McFadden, and R. Rayudu, "Weather-dependent power flow algorithm for accurate power system analysis under variable weather conditions," *IEEE Transactions on Power Systems*, vol. 34, no. 4, pp. 2719–2729, 2019-07.

[18] M. AlHajri and M. El-Hawary, "Exploiting the radial distribution structure in developing a fast and flexible radial power flow for unbalanced three-phase networks," *IEEE Transactions on Power Delivery*, vol. 25, no. 1, pp. 378–389, 2010.

[19] Z. Wang, F. Chen, and J. Li, "Implementing transformer nodal admittance matrices into backward/forward sweep-based power flow analysis for unbalanced radial distribution systems," *IEEE Transactions on Power Systems*, vol. 19, no. 4, pp. 1831–1836, 2004.

[20] D. Rajicic, R. Ackovski, and R. Taleski, "Voltage correction power flow," *IEEE Transactions on Power Delivery*, vol. 9, no. 2, pp. 1056–1062, 1994.

[21] G. Chang, S. Chu, and H. Wang, "An improved backward/forward sweep load flow algorithm for radial distribution systems," *IEEE Transactions on Power Systems*, vol. 22, pp. 882–884, 2002.

[22] U. Eminoglu and M. H. Hocaoglu, "Distribution systems forward/backward sweep-based power flow algorithms: A review and comparison study," *Electric Power Components and Systems*, vol. 37, no. 1, pp. 91–110, 2008.

[23] D. Shirmohammadi, H. W. Hong, A. Semlyen, and G. X. Luo, "A compensation-based power flow method for weakly meshed distribution and transmission networks," *IEEE transactions on power systems*, vol. 3, no. 2, pp. 753–762, 1988.

[24] W. Kersting and D. Mendive, "An application of ladder network theory to the solution of three phase radial load-flow problems," in *IEEE PAS Winter Meeting*, (New York, NY), 1976.

[25] G. Cespedes, "New method for the analysis of distribution networks," *IEEE Transactions on Power Delivery*, vol. 5, no. 1, pp. 391–396, 1990.

[26] M. Haque, "Load flow solution of distribution systems with voltage dependent load models," *Electric Power Systems Research*, vol. 36, no. 3, pp. 151–156, 1996.

[27] W. H. Kersting, *Distribution System Modeling and Analysis*. Boca Raton, FL: CRC Press, and imprint of Taylor and Francis, 2nd edition. ed., 2006.

[28] A. Picanco and A. Z. de Souza, "Temperature-dependent radial power flow with distributed generation," in *2019 IEEE Milan PowerTech*, (Milan, Italy), 2019.

[29] K. P. Schneider, B. A. Mather, B. C. Pal, C.-W. Ten, G. J. Shirek, H. Zhu, J. C. Fuller, J. L. R. Pereira, L. F. Ochoa, L. R. de Araujo, R. C. Dugan, S. Matthias, S. Paudyal, T. E. McDermott, and W. Kersting, "Analytic considerations and design basis for the ieee distribution test feeders," *IEEE transactions on power systems*, vol. 33, no. 3, pp. 3181–3188, 2018.

[30] "IEC 60287. electric cables - calculation of the current rating," 1994.

[31] The Aluminum Association, *Aluminum Electrical Conductor Handbook*. Washington, DC: Aluminum Association Publication, 2nd ed., 1982.

[32] M. Rahman, F. Atchison, and V. Cecchi, "Temperature-dependent system level analysis of electric power transmission systems: A review," *Electric Power Systems Research*, vol. 193, pp. 107033–, 2020.

[33] J. Engelhardt and S. Basu, "Design, installation, and field experience with an overhead transmission dynamic line rating system," in *Proceedings of 1996 Transmission and Distribution Conference and Exposition*, (Los Angeles, CA, USA), pp. 366–370, 1996.

[34] B. Howington and G. Ramon, "Dynamic thermal line rating summary and status of the state-of-the-art technology," *IEEE Transactions on Power Delivery*, vol. 2, no. 3, pp. 851–858, 1987-07.

[35] H. Wan, J. McCalley, and V. Vittal, "Increasing thermal rating by risk analysis," *IEEE Transactions on Power Systems*, vol. 14, no. 3, pp. 815–828, 1999-08.

[36] C. Black and W. Chisholm, "Key considerations for the selection of dynamic thermal line rating systems," *IEEE Transactions on Power Delivery*, vol. 30, no. 5, pp. 2154–2162, 2015-10.

[37] J. Hall, A. Deb, and J. Savoullis, "Wind tunnel studies of transmission line conductor temperatures," *IEEE Transactions on Power Delivery*, vol. 3, no. 2, pp. 801–812, 1988-04.

[38] F. McElvain and S. Mulnix, "Statistically determined static thermal ratings of overhead high voltage transmission lines in the rocky mountain region," *IEEE Transactions on Power Systems*, vol. 15, no. 2, pp. 899–902, 2000-05.

[39] S. Rowland and F. Easthope, "Electrical ageing and testing of dielectric self-supporting cables for overhead power lines," 1993-09.

[40] M. Bhuiyan, P. Musilek, J. Heckenbergerova, and D. Koval, "Evaluating thermal aging characteristics of electric power transmission lines," *CCECE*, pp. 1–4, 2010.

[41] H. Brown, G. Carter, H. Happ, and C. Person, "Power flow solution by impedance matrix iterative method," *IEEE Transactions on Power Apparatus and Systems*, vol. 82, no. 65, pp. 1–10, 1963-04.

[42] C. Cheng and D. Shirmohammadi, "A three-phase power flow method for real-time distribution system analysis," *IEEE Transactions on Power Systems*, vol. 10, no. 2, pp. 671–679, 1995-05.

[43] R. Broadwater, A. Chandrasekaran, C. Huddleston, and A. Khan, "Power flow analysis of unbalanced multiphase radial distribution systems," *Electric Power Systems Research*, vol. 14, no. ue. 1, February, pp. 23–33.

[44] *Aluminum Electrical Conductor Handbook*. The Aluminum Association, 3rd ed., 1989.

[45] P. Zarco and A. Exposito, "Power system parameter estimation: a survey," *IEEE Transactions on Power Systems*, vol. 15, no. 1, pp. 216–222,, 2000-02.

[46] L. Staszewski and W. Rebizant, "Temperature dependent dynamic loadability control for transmission lines," in *2011 International Conference on Advanced Power System Automation and Protection*, (Beijing), pp. 1981–1985, 2011.

[47] V. Knyazkin, C. Canizares, and L. Soder, "On the parameter estimation and modeling of aggregate power system loads," *IEEE Transactions on Power Systems*, vol. 19, no. 2, pp. 1023–1031, 2004-05.

[48] J. Black, J. Colandairaj, S. Connor, and B. O'Sullivan, "Equipment and methodology for the planning and implementation of dynamic line ratings on overhead transmission circuits," *Wroclaw*, pp. 1–6, 2010.

[49] S. Talpur, C. Wallnerstrom, P. Hilber, and S. Saqib, "Implementation of dynamic line rating technique in a 130 kv regional network," in *17th IEEE International Multi Topic Conference 2014*, (Karachi), pp. 477–482, 2014.

[50] P. Kacejko, M. Wydra, W. Nowak, W. Szpyra, and R. Tarko, "Advantages, benefits, and effectiveness resulting from the application of the dynamic management of transmission line capacities," in *2018 15th International Conference on the European Energy Market (EEM*, (Lodz), pp. 1–5, 2018.

[51] A. Ghosh and V. Mukherjee, "Temperature dependent optimal power flow," in *2017 International Conference on Technological Advancements in Power and Energy (TAP Energy*, (Kollam), pp. 1–6, 2017.

[52] Q. Gao, Z. Wei, G. Sun, Y. Sun, and H. Zang, "Temperature-dependent optimal power flow based on simplified interior point method," in *2015 5th International Conference on Electric Utility Deregulation and Restructuring and Power Technologies (DRPT*, (Changsha), pp. 765–769, 2015.

[53] P. Bamane, A. Kshirsagar, S. Raj, and H. Jadhav, "Temperature dependent optimal power flow using gbest-guided artificial bee colony algorithm," in *2014 International Conference on Computation of Power, Energy, Information and Communication (ICCPEIC*, (Chennai), pp. 321–327, 2014.

[54] A. Picanco and A. Oliveira, "Reactive optimal power flow in the temperature-dependent power flow using interior point method with artificial neural network," in *IET Conference Proceedings*, pp. 66–, 2018.

[55] U. Nowak and L. Weimann, "A family of newton codes for systems of highly nonlinear equations," *Konrad-Zuse-Zentrum fur Informationstechnik Berlin*, 1991.

[56] U. Ghatak and V. Mukherjee, "A fast and efficient load flow technique for unbalanced distribution system," *International Journal of Electrical Power and Energy Systems*, vol. 84, no. 1, pp. 99–110, 2017.

[57] J. R. Carson, "Wave propagation in overhead wires with ground return," *Bell System Technical Journal*, vol. 5, 1926.

[58] W. H. Press, S. A. Teukolsky, W. T. Vetterling, and B. P. Flannery, *Numerical Recipes: The Art of Scientific Computing*. New York, NY: Cambridge University Press, 3rd edition. ed., 2007.

[59] TEXCAN, "Unarmoured medium voltage concentric neutral aluminum conductor." `https://ecat.eleknet.com/PIM_Docs/Docs/STEP_ASSETS_PDF/211326702.pdf`, 2022.

[60] National Cable Specialists, "Medium voltage power cables." `https://nationalcablespecialists.ca/wp-content/uploads/CN_cables.pdf`, 2021.

[61] Prysmian, "5-35kv 1/c epr mv-105 easy glider (tape shield)." `https://prioritywire.com/specs/Single%20Conductor%2015KV,%20Shielded,%20MV-105.pdf`, 2021.

[62] IEEE PES AMPS DSAS Test Feeder Working Group, "IEEE PES test feeder." `https://cmte.ieee.org/pes-testfeeders/`, 2022.

[63] NOAA National Centers for Environmental Health, "Charlotte douglas international airport weather data." `https://www.ncdc.noaa.gov/cdo-web/`, 2020.

[64] USDA Natural Resources Conservation Service National Weather and Climate Center, "Scan station tidewater 1, washington county, nc." `https://www.nrcs.usda.gov/wps/portal/wcc/home/snowClimateMonitoring/soilClimateConditions/`, 2020.

[65] Mecklenburg County Soil and Water Conservation, "Mecklenburg soil survey." https://www.mecknc.gov/LUESA/WaterandLandResources/Conservation/Pages/Soil%20Survey.aspx, 1975.

[66] O. Gouda and A. El Dein, "Improving underground power distribution capacity using artificial backfill materials," *IET Generation, Transmission Distribution*, vol. 9, pp. 1–8, 07 2015.

[67] United States Department of Commerce, National Bureau of Standards, "Copper wire tables, handbook 100." https://nvlpubs.nist.gov/nistpubs/Legacy/hb/nbshandbook100.pdf, 1966.